PLASMON ASSISTED FLUORESCENCE EMISSION:

FAR-FIELD OBSERVABLES AND THEIR FLUCTUATIONS

Cover: photograph of a glass marble, plated with 17 karat gold leaf, in a water / milk mixture. The light traces, mimicking random trajectories of fluorescent molecules, were painted with a red LED during the 15 seconds of exposure.

Ph.D. thesis, Universiteit van Amsterdam, July 2015
Plasmon assisted fluorescence emission:
far-field observables and their fluctuations
Lutz Armin Langguth

ISBN 978-90-77209-92-9

A digital version of this thesis can be downloaded from
http://www.amolf.nl.

PLASMON ASSISTED FLUORESCENCE EMISSION:

FAR-FIELD OBSERVABLES AND THEIR FLUCTUATIONS

ACADEMISCH PROEFSCHRIFT

ter verkrijging van de graad van doctor
aan de Universiteit van Amsterdam
op gezag van de Rector Magnificus
Prof. Dr. D. C. van den Boom
ten overstaan van een door het College voor Promoties ingestelde commissie,
in het openbaar te verdedigen in de Agnietenkapel
op vrijdag 3 juli 2015, te 12:00 uur

door

Lutz Armin Langguth

geboren te Karlsruhe, Duitsland

Promotor:	Prof. Dr. A. F. Koenderink	Universiteit van Amsterdam
Overige leden:	Prof. Dr. M. Lippitz	Universität Bayreuth
	Prof. Dr. P. C. M. Planken	Universiteit van Amsterdam
	Prof. Dr. H. B. van Linden van den Heuvell	Universiteit van Amsterdam
	Dr. P. Zijlstra	Technische Universiteit Eindhoven
	Dr. K. Dohnalová	Universiteit van Amsterdam
Faculteit:	Faculteit der Natuurwetenschappen, Wiskunde en Informatica	

The work described in this thesis is part of the research program of the "Stichting voor Fundamenteel Onderzoek der Materie" (FOM) which is financially supported by the "Nederlandse organisatie voor Wetenschappelijk Onderzoek" (NWO). It is also funded by NanoNextNL, a nanotechnology program funded by the dutch ministry of economic affairs, and the European Research Council (ERC).

This work was carried out at the
Center for Nanophotonics,
FOM Institute for Atomic and Molecular Physics AMOLF,
Science Park 104, 1098 XG Amsterdam, The Netherlands
where a limited number of copies of this dissertation is available.

Contents

1

Introduction

This thesis revolves around light, and in particular the control of light at the nanometer scale. *Nanophotonics* is the science of both understanding and manipulating the creation of light, its propagation, and the information it can carry. This first chapter gives a brief historical outline and introduction to the four main ingredients which define the content of this thesis: Electromagnetic waves, nano-optics, fluorescence and intensity correlations. In this work we investigate potential improvements of fluorescence applications by plasmonic antennas.

1.1 Electromagnetic waves

In 1864 James Clerk Maxwell proposed a set of equations [1], now known as Maxwell's equations, to unify a set of laws that famous scientists had empirically established for the behavior of charges, currents, and electromagnetic fields. These laws are Gauss's law, which describes the electrostatic field for a given charge distribution, the Biot-Savart's law - modelling the magnetic field due to electric current, Faraday's law of electromagnetic induction and Ampères circuit law.

Within the limits of classical physics, Maxwell equations describe all electromagnetic phenomena, ranging from electrostatics and magnetostatics, radio wave technology, to optics, and X-ray diffraction. Maxwell equations themselves directly show that accelerating charges are responsible for generating time-varying fields, meaning that AC currents are sources of electromagnetic waves. While it is evident that all matter is composed of atoms, that contain a positively charged nucleus and a negatively charged electron cloud, it would be highly impractical if electrodynamics would require microscopic accounting of all charges. Instead, one of the most powerful approximation in Maxwell's equation is that matter can be accounted for by two material properties: the response of the medium to an external electric field (permittivity) and a magnetic field (permeability). These can be ascribed to a net polarization of the medium due to the displacement of the electron cloud

relative to the nuclei. These two material properties determine the reflection, absorption and penetration of an external field into this material.

Maxwell equations predict propagating waves, propagating at the speed of light. The first experimental confirmation that moving charges create propagating waves was obtained by Heinrich Hertz in 1886. He used electrical discharges between two metal wires to create propagating waves which he could detect by observing a spark in the small gap of a receiver antenna, caused by a local electric field enhancement high enough to ionize air.

The concept of oscillatory currents in wires generating propagating fields is the basis of radio-frequency communication. Radio frequency technology revolves around the engineering of current carrying objects with meter-sized length scales, operating at MHz to GHz frequencies, fundamental for transmitting and receiving information as in radio communication and the basis of all presentday wireless communication technology. In 1909 Guglielmo Marconi and Karl Ferndinand Braun were awarded the Nobel prize in physics 'in recognition of their contributions to the development of wireless telegraphy'.

The radio waves of Marconi and Braun were of very low frequency, and hence through the speed of light by necessity also at very long, kilometer-scale wavelengths. Since Maxwell equations are essentially scale invariant, the concepts of radio frequency can in theory be scaled to the much higher frequencies of optics, simply by scaling down the linear dimensions of antenna designs. Scaling up the frequency to the optical domain (500 THz), or equivalently scaling down the wavelength from meter-sized to $400-700$ nm, implies that antennas to control light should be therefore nanoscale. The two limitations to this argument are that on the one hand material properties, i.e., permeability and permittivity, change significantly with frequency. On the other hand, the notion of a classical current at THz frequencies does not exist. Currents at 500 THz can not be generated in circuit boards, and do not propagate on copper wires. Sources for this frequency range are electronic transitions in atoms and molecules.

The fact that in optics, sources of light are not classical currents, but rather quantum mechanical transitions in single atoms and molecules, immediately leads to the notion that optics is related to quantum mechanics. In fact, the question of how light is created on a microscopic level was the cradle of quantum physics. An important step to developing quantum physics is the derivation of the broad emission spectrum of thermally excited materials, i.e., the black-body spectrum derived by Planck. Max Planck was awarded the Nobel prize in 1918 for postulating that the black body spectrum is generated by quantized oscillators.

Einsteins analysis of the photoelectric effect proved that it is the light itself that is quantized as 'photons', for which he obtained the Nobel prize in 1921. Niels Bohr then explained the discrete light emission spectrum of atoms based on the notion of quantized orbitals around the nucleus and he was awarded the Nobel prize in 1922.

1.2 Nano-optics and plasmon antennas

This thesis is positioned in the field of nano-optics. Nano-optics is the science of controlling the generation, propagation, and detection of light on length scales on the order of 1 nanometer (10^{-9} meter). Controlling light on the nanoscale is a very different

challenge from the traditional field of optics in which one steers light by lenses, mirrors and prisms. The reason is the wave nature of propagating electromagnetic fields, with a wavelength between $400-700$ nm for light in the visible spectrum. The wave nature results in limitations on the field distributions which can be obtained. Superimposing harmonic waves of a wavelength λ results in intensity distributions where two maxima are separated at least by $\Delta x \approx \lambda/2$. This fact is called the diffraction limit, and was formulated by Ernst Abbe [2] and Lord Rayleigh [3]. The diffraction limit was thought to be a fundamental limit to how small electromagnetic fields can be localized, and is the fundamental limit for the resolution of far-field optical microscopy.

The limit of Abbe not only applies to microscopy. It also applies to the control of light. As an example, consider the transport of light as a guided wave. In a standard glass optical telecom fiber, the mode has a micron-sized transverse cross section [4]. In the best chip-scale technology based on transparent materials, confinement is limited to $\lambda/2$ [5]. Only in the past decade, it has been realized that Abbe's limit of diffraction for field confinement can be broken by using nanoscale antennas made from metal. In retrospect this should not come as a surprise, since at radio frequencies it is common to work with subwavelength devices. For instance, Marconi used kilometer waves, but antennas tens of meters and larger, up to $\lambda/4$ in size.

Shrinking antennas to the nanoscale changes the physics significantly, because the response of metals at optical frequencies is different from that of a near perfect conductor. Optical frequencies approach the intrinsic response frequency of the free electron plasma in common metals. This can be used to advantage, as it enables one to excite "plasmons", i.e., intrinsic resonances of the free electron plasma. The field of plasmonics employs metal nano-structures in which currents are excited resonantly. Therefore they offer strong near-field enhancements [6, 7].

Plasmonics is pursued for a very wide range of applications that range all the way from optical information processing, improvement of solar cells and LEDs, to improving microscopy and spectroscopy of single molecules [8, 9]. In this thesis we focus entirely on the application of nano-antennas to microscopy and spectroscopy. The essential idea is that by tightly focusing the field to the nanoscale, thus greatly enhancing the optical field strength, it becomes possible to interrogate and control even single molecules to an unprecedented degree. Historically, plasmonics was first pursued for spectroscopy in the framework of Raman scattering. Raman scattering is an inelastic scattering effect in which light interacts with molecular vibrations [10]. Thus, it is commonly used to identify molecules by their typical vibrational frequency spectrum. Since the effect is very weak, it is very challenging to measure Raman spectra of single molecules. Due to the $|E|^4$ scaling of the Raman scattering signal with electric field strength, using plasmon-enhancement is particularly attractive. In fact, Surface Enhanced Raman Scattering (SERS) has been pursued since the early 1970s, typically using rough metal films [11]. The current state of the art in plasmon-enhanced Raman scattering is scanning probe microscopy. Recent reports highlight that Tip Enhanced Raman Scattering [12] can even reach sub-molecular resolution. Plasmonics has also been applied to other types of vibrational spectroscopy, such as in infrared-absorption spectroscopy [13].

The bigger goal of controlling fluorescence by plasmonics aims at improving the brightness and directivity of single molecules, which by themselves tend to be dim and

omnidirectional emitters. Turning these into bright and directional emitters of single photons is relevant for information processing, quantum optics and microscopy. Nano-antennas have shown up to a 1000-fold brightness enhancement of single molecule fluorescence [14–17]. Further, nano-antennas can make far-field emission of a single molecule highly directional [18–21].

1.3 Fluorescence

The term *Fluorescence* was coined by Sir George Gabriel Stokes for an observation he conducted in the mineral Fluorite. He observed that ultra violet light was transformed into visible light [22]. Many materials show fluorescence, from tissue in some animals or plants, minerals, to synthetic organic dye molecules [10] and quantum dots [23], which are designed for their fluorescent properties. The physical process can only be explained by quantum mechanics. As in an atom, in a fluorescent molecule there are discrete electronic states an electron can occupy. Figure 1.1 shows a simplified level scheme of a fluorescent molecule. The electronic states (black lines) are split into several levels of vibrational and rotational states (gray lines). When a photon is absorbed the electron undergoes a transition into an excited state. The system quickly relaxes into its rotational and vibrational ground-state (within picoseconds), but stays electronically excited. Then, within nanoseconds, it relaxes to the electronic ground state under the emission of a photon. This photon is red-shifted compared to the excitation photon. The energy difference between the excitation and emission photon is called Stokes shift, and corresponds to energy which is lost as heat.

The huge benefits of fluorescence for biological imaging became quickly evident when autofluorescence of biological samples was first observed, and later by the possibility to stain bio-molecules selectively with fluorescent labels. In 1962, Shimonura isolated the green fluorescent protein from jellyfish, which allowed to make living cells produce the fluorescent labels themselves. In current-day biological research, analysis of biological processes is unthinkable without fluorescent labels, which selectively bind to, or are even generated within a cell linked to specific proteins. The latest achievement in fluorescence microscopy is the development of super resolution methods, which allow to localize fluorescent labels with an accuracy more than an order of magnitude better than allowed

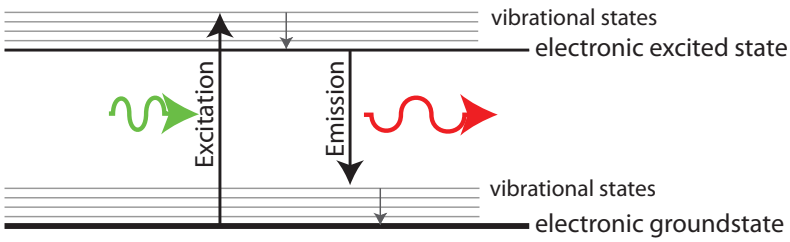

Figure 1.1: Simplified Jablonski diagram of a fluorescent molecule. A photon is absorbed and excites the molecule into the electronic excited state, and additionally excites vibrations. The vibrational excitations decay within picoseconds. Within nanoseconds the system relaxes into the electronic ground state under the emission of a fluorescence photon, which has less energy than the excitation.

by the diffraction limit [24]. Moerner, Betzig and Hell were awarded the Nobel prize in chemistry in 2014 for their work on super resolution microscopy.

Not only in research labs has fluorescence become an indispensable tool, also our private lives are brightened by fluorescence. Nowadays almost all modern indoor lighting is provided by compact fluorescent lamps or light emitting diodes (LED). The light source in compact fluorescent lamps is mercury vapor, which has its most dominant emission lines in the blue, violet and UV. The surface of the tube is coated with fluorescent particles which convert these parts of the spectrum into longer wavelengths to provide a white spectrum. Choosing and mixing different fluorescent substances allows to adjust the spectrum and give the light source the desired color temperature. Similarly, in solid state lighting with LEDs, a semiconductor with a bandgap of $3-4$ eV efficiently creates blue photons, a part of which is then converted by a fluorescent layer into yellow light to result in light which is perceived as white. The invention of the blue LED has been awarded the Nobel prize in physics in 2014 to Akasaki, Amano and Nakamura. For a historical overview we refer the reader to ref. [25].

1.4 Intensity correlations

This thesis deals with a particular property of fluorescent light, namely the information that can be gathered by analyzing the temporal fluctuations of fluorescence intensity. If a classical oscillating current at some constant frequency is inserted into Maxwell's equations, one finds a steady-state solution in which the fields vary at the driving frequency, but in which there is no difference in energy density or intensity, from one optical cycle to the next [26]. In optics, however, temporal fluctuations in intensities are relevant from two perspectives. On the one hand, the discrete nature of photons means that quantum mechanics fundamentally imposes fluctuations on any source [27]. On the other hand, even if quantum mechanics can be disregarded, observed optical properties can fluctuate due to fluctuations in the environment. Studying these optical fluctuations can thus be a tool to obtain information about the fluctuations of the environment [10].

In this thesis we compute temporal correlation functions of fluctuating light intensities. The correlation of two intensity signals is defined as $\langle I_1(t), I_2(t+\tau)\rangle / [\langle I_1(t)\rangle \langle I_2(t)\rangle]$ where $\langle I(t)\rangle$ denotes the time average of I. The correlation function quantifies the probability that at time $t+\tau$ the measured intensity is similar to its value at time t. In quantum optics, intensity-correlations are used to categorize light sources into three different types, based on their photon statistics [27]: First, photons emitted by a single molecule or other single-photon source can only emit one photon at a time. Thus, the temporal photon statistics shows an anti-bunching at $\tau = 0$. In contrast, photons emitted from a thermal source tend to arrive at the same time, they travel "bunched". Finally, a coherent source, such as a laser, shows uncorrelated photon arrival times and the normalized auto-correlation is 1, independent of τ. The first experimental realization of an intensity correlation in the visible spectrum was performed by Hanbury-Brown and Twiss in 1956 [28]. They exploited the bunching at $\tau = 0$ of a thermal emitter, the star Sirius, and measured the coincidence counts at $\tau = 0$ between two detectors mounted on two telescopes pointing at the star. Increasing the distance between the detectors, showed the disappearance of coincidence counts at

a distance given by the spatial coherence length, which allowed them to calculate the size of Sirius. Nowadays, the term "Hanbury-Brown Twiss measurement" usually refers to a measurement in which a photon stream is sent to two single-photon counters via a beamsplitter. This is a standard tool in laboratories to assess whether a source antibunches, bunches, or is coherent [29].

Intensity correlations are a robust tool to find and quantify characteristic timescale of a fluctuating observable. When passing a beam of light through a system with fluctuating optical properties, these temporal changes are relayed to an intensity change. Performing an auto-correlation of this intensity trace yields the characteristic timescales of the fluctuations of the optical properties. Applying this method to the fluctuations of transmission or reflection through a liquid, in which scattering particles are diffusing, is called dynamic light scattering (DLS). DLS works for particles with scattering cross-sections which are sufficiently high to give a measurable intensity change in transmission or reflection, and as such, it is not suitable for single molecules. We refer to [30] for a comprehensive review on scattering based fluctuation techniques such as DLS. When the specimen of interest is fluorescently labeled, one can analyze its diffusive motion by analyzing the temporal fluctuations in fluorescence, instead of scattering, using the same correlation techniques. This technique is called "Fluorescence Correlation Spectroscopy" and was first developed by Magde, Elson and Webb [31] in 1972. Nowadays, it is commonly used to study the diffusive behavior of single molecules in biophysical systems. We refer to Chapter 2 for a review of the basics of FCS. Metallic nano-structures have been recently used to improve the performance of FCS [32, 33].

1.5 Motivation and overview of this thesis

In this thesis we investigate how to employ metal nano-structures to control fluorescence emission for different applications. Our main approach is based on plasmon-antenna enhanced fluorescence correlation spectroscopy. The basic idea is that when a fluorophore diffuses very close to a plasmon antenna, its fluorescence signature may be strongly increased in terms of brightness, polarization, and fluorescence lifetime. Since the typical distances at which these modifications occur are about $\lambda/10$, position fluctuations of fluorophores translate into large and fast fluctuations in various optical signatures. This thesis is divided into three parts.

The first part addresses the theory of Fluorescence Correlation Spectroscopy (FCS). Since FCS uses an optical system to measure intensity fluctuations that derive from temporal fluctuations it is evident that the theory hinges on the understanding how microscope properties and diffusion physics come together. The microscope part is lumped into a so-called "molecular detection function", that sets the spatial selectivity of the excitation and detection optics to a small volume. Chapter 2 introduces the molecular detection function and the correlation function. We illustrate the molecular detection function by exact calculations of antenna-enhanced FCS at a Mie sphere. In Chapter 3 a general model is developed which allows the efficient calculation of FCS measurements in the presence of arbitrarily complex molecular detection functions. The model is applied to a simple system of a diffraction limited focus with a superimposed hot-spot,

which elucidates the requirements and limitations for a plasmon-enhanced fluorescence correlation experiment. We show how the fluorescence background originating from the diffraction limited focus adversely affects the high correlation contrast provided by the hot-spot.

The second part of the thesis, highlights the potential of nano-optics in combination with single molecule fluorescence by the exploitation of other degrees of freedom of the fluorescence emission, like polarization, fluorescence lifetime or radiation pattern. Chapter 4 describes a new method to localize single molecules close to a nano-antenna based on different far-field observables. The proposed method uses simultaneous measurements of different far-field observables, which allow to reconstruct the coordinates with an accuracy of a few nanometers relative to the nano-antenna. Furthermore, it allows localization rates in the kHz regime. Chapter 5 shows how diffusing emitters introduce fluctuations in non-intensity observables. We show how lifetime fluctuations can alleviate the problems of background signals which we have encountered in Chapter 3. Further, Chapter 5 shows that lifetime and polarization fluctuations can be used to measure the near-field volume of plasmonic antennas. As the calibration of a plasmon-enhanced FCS experiment is intrinsically challenging, Chapter 6 presents a plasmonic design of a dual focus FCS experiment which allows the measurement of a diffusion coefficient without additional calibration.

Part three discusses two experiments that both address the question of how to shape the fluorescence emission of an incoherent ensemble. Chapter 7 presents an improvement to the nano-aperture design for FCS measurements that was reported in [32, 33]. In nano-aperture enhanced FCS experiments one uses a small aperture in a metal film. Typically, a large fraction of the fluorescence photons is lost because the emitter does not radiate in the collection optics, but rather into surface plasmons, i.e., surface waves bound to the metal film. We show how the surface plasmons can be recuperated to contribute to the photon signal by small periodic arrays of nano-apertures can couple surface plasmon polaritons out into highly directional free space radiation right into collection optics. Chapter 8 combines the concept of metasurfaces with an ensemble of incoherent sources in a waveguide. We show how the design of a periodic meta surface allows to control the scattering amplitude of the reciprocal lattice, and how it translates into directional emission into the far-field.

Part I

Fluorescence correlation spectroscopy

2

Introduction to fluorescence correlation spectroscopy

2.1 Fluorescence correlation spectroscopy and the molecular detection function

2.1.1 Fluorescence correlation spectroscopy

Fluorescence correlation spectroscopy (FCS) [31] is widely used to locally investigate the diffusion coefficient of single molecules in a solution. A wealth of literature is available on its benefits for different applications typically found in biophysics [34, 35]. FCS exploits random fluorescence intensity fluctuations that occur as individual molecules diffuse in and out of focus in a confocal measurement configuration, as illustrated in figure 2.1. These random fluctuations are correlated on a time scale given by the diffusion constant and the focus size. By its very nature, diffusion measurements via FCS require the number of detected molecules (fluorophores in the diffraction limited focus) to fluctuate significantly due to brownian motion, which limits the maximal concentration at which FCS measurements can be performed. With a standard diffraction limited excitation volume this translates to about one per λ^3 or 1 nM ($1 \cdot 10^{-9}$ mol/l).

In a typical Fluorescence Correlation Spectroscopy measurement, a collimated laser is focused by a microscope objective in a solution of fluorophores which undergo brownian motion. The fluorescence signal is picked up through the same objective, passes a spectral filter to block the scattered laser light and the fluorescence is then detected on a sensitive detector and stored as a function of time $F(t)$. Temporal fluctuations in the fluorescence intensity originate from single molecules randomly entering and leaving the focus. The stochastic trajectories are reflected in temporal correlations in the fluorescence signal, which are quantified by the auto-correlation of the fluorescence intensity.

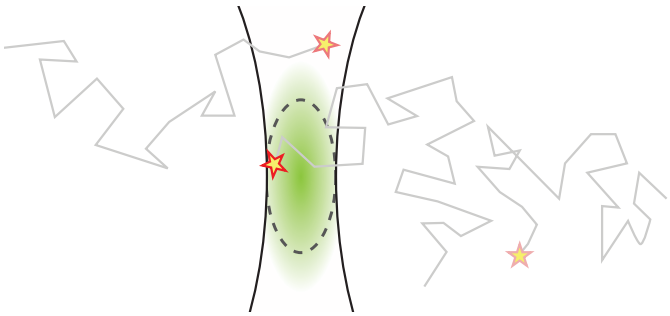

Figure 2.1: Illustration of an excitation beam focused in a liquid. The volume is filled with fluorophores which undergo brownian motion, when their trajectories cross the focus high fluorescence intensity is detected.

2.1.2 Definition of the molecular detection function and the correlation function

Given that we defined the auto-correlation of the detected fluorescence intensity time trace as observable, the question is, what determines the instantaneous fluorescence intensity? It must depend on two factors: on the one hand, the instantaneous spatial concentration of the fluorophores $C(\mathbf{r}, t)$ in the focus, and on the other, the properties of the microscope optics, i.e. the optical excitation and detection efficiency*. In FCS literature it is conventional to lump both the excitation and collection properties of the microscope into a quantity called the molecular detection function (MDF). The $MDF(\mathbf{r})$ represents the probability density function for detecting a set number B of photons per unit time, given that a molecule is at location $\mathbf{r}$. With this definition, the fluorescence intensity reads [10]

$$F(t) = B \iiint \mathrm{MDF}(\mathbf{r})\, C(\mathbf{r}, t) \mathrm{d}^3\mathbf{r}\,. \tag{2.1}$$

Performing a normalized auto-correlation

$$G(\tau) = \frac{\int F(t)\, F(t+\tau)\, dt}{\left[\int F(t) dt\right]^2}$$

of the fluorescence intensity $F(t)$ yields

$$G(\tau) = \frac{B^2 \iiint \mathrm{MDF}(\mathbf{r}) \iiint \mathrm{MDF}(\mathbf{r}') \left\langle \delta C(\mathbf{r}, 0)\, \delta C(\mathbf{r}', \tau) \right\rangle \mathrm{d}^3\mathbf{r}' \mathrm{d}^3\mathbf{r}}{\left[B \langle C \rangle \iiint \mathrm{MDF}(\mathbf{r}) \mathrm{d}^3\mathbf{r}\right]^2} + 1 \tag{2.2}$$

where $\left\langle \delta C(\mathbf{r}, 0)\, \delta C(\mathbf{r}', \tau) \right\rangle$ is the probability to find a fluorophore at time $t+\tau$ at position $\mathbf{r}'$, when it was located at $\mathbf{r}$ at time t. Commonly one assumes free diffusion, that is, diffusion in a 3D solvent without geometrical constraints, sources, sinks or boundaries. In the case of free translational diffusion, the term $\left\langle \delta C(\mathbf{r}, 0)\, \delta C(\mathbf{r}', \tau) \right\rangle$ is given by the solution of the diffusion equation $\left\langle \delta C(\mathbf{r}, 0)\, \delta C(\mathbf{r}', \tau) \right\rangle = \langle C \rangle \left(4\pi D\tau\right)^{-\frac{3}{2}} \exp\left[-\left(\mathbf{r}-\mathbf{r}'\right)^2 / \left(4\, D\, \tau\right)\right]$ where D is the diffusion coefficient and $\langle C \rangle$ the average concentration of the fluorophores. Thus, the

*The vector nature of the electric field and the transition dipole moment of the molecule are neglected here.

auto correlation can be read as first taking the convolution of the MDF with the time-dependent diffusion kernel, and subsequently taking the overlap integral of this blurred MDF, with the MDF itself. FCS has also been applied to the case of two dimensional diffusion in a plane, i.e. in biological membranes. In this case the diffusion kernel is also Gaussian.

2.1.3 Gaussian FCS theory

In mathematical terms, the molecular detection function (MDF) is the probability density function which quantifies the likelihood to detect a fluorophore at position $\mathbf{r}$. The spatially dependent part of the MDF can be factorized in three functions:

$$MDF(\mathbf{r}) = EEF(\mathbf{r}) \cdot \eta(\mathbf{r}) \cdot CEF(\mathbf{r}) \ .$$

The product of all factors independent from position yields the prefactor B. This prefactor includes no spatial dependence, but instead accounts for all types of absolute set-up efficiencies, such as the excitation pump power, the absorption cross section of the molecule, the overall transmission coefficient of the optics towards the objective, and detector quantum efficiency. Since in the final measurement, the factor B drops out, it is typically left out of FCS considerations. Returning to the factorization of the MDF we discuss the three factors. First, the excitation efficiency function (EEF) is given by the intensity distribution of the pump field. Second, the quantum efficiency $\eta(\mathbf{r})$ is given by the probability of the fluorophore to emit a photon when it is excited [36, 37]. Third, the collection efficiency function (CEF) quantifies the chance that an emitted photon is captured by the collection optics and detected. For FCS measurements in a bulk solution with a tightly focused excitation spot, the MDF is often approximated as a 3D gaussian Γ, determined by its strength S, center position $\mathbf{R}$ and width in each dimension σ

$$\Gamma(\mathbf{r}, S, \mathbf{R}, \sigma) = \left(\frac{2}{\pi}\right)^{\frac{3}{2}} \frac{S}{\sigma_1 \sigma_2 \sigma_3} \exp\left[-2 \sum_{k=1,2,3} \left(\frac{r_k - R_k}{\sigma_k}\right)^2\right].$$

We derive the correlation function for molecular detection functions of gaussian shape with free 3D diffusion. The solution of the diffusion equation is then given by $\left\langle \delta C(\mathbf{r}, 0)\, \delta C(\mathbf{r}', \tau) \right\rangle = \Gamma(\mathbf{r}, \langle C \rangle, \mathbf{0}, 4D\tau)$. Substituting this expression into $G(\tau)$ yields

$$G(\tau) = \frac{\iiint \mathrm{MDF}(\mathbf{r}) \left\{ \iiint \mathrm{MDF}(\mathbf{r}') \, (4\pi D\tau)^{-\frac{3}{2}} \exp\left[-\left(\mathbf{r} - \mathbf{r}'\right)^2 / (4D\tau)\right] \mathrm{d}^3\mathbf{r}' \right\} \mathrm{d}^3\mathbf{r}}{\langle C \rangle \left[\iiint \mathrm{MDF}(\mathbf{r}) \mathrm{d}^3\mathbf{r} \right]^2} + 1. \quad (2.3)$$

The expression in curly brackets can be intuitively seen as the MDF blurred by the diffusion process with a Gaussian of width $4D\tau$. The volume integrated product of the blurred MDF with the original one quantifies the time evolution of the probability to detect a particle at a time $t + \tau$, after it has been already detected at time t. We now can solve eq. (2.3) analytically:

$$G'(\tau) = \left[\langle C \rangle \prod_{k=1,2,3} \sqrt{\pi} \sqrt{4D\tau + \sigma_k^2} \right]^{-1} \quad (2.4)$$

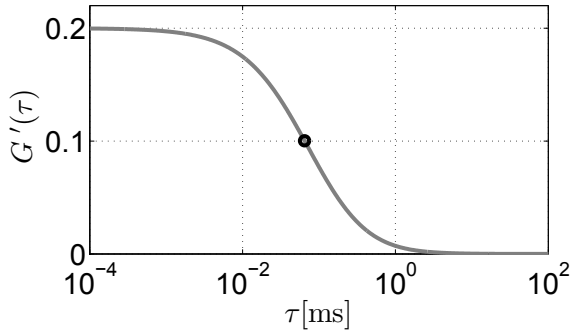

Figure 2.2: A typical correlation function for a ø10 nm sphere diffusing in water (viscosity $\eta_{H_2O} = 8.9 \cdot 10^{-4}$ Pa s). The MDF is of gaussian shape with a width of 300 nm in x and y and 600 nm in z direction. The correlation contrast is 0.2, thus on average $< N >= 5$ emitters are in the detection volume. The roll off time is 0.94 ms (black circle). The diffusion coefficient is calculated by the Einstein-Stokes model [38].

where $G'(\tau) = G(\tau) - 1$ was introduced for the sake of brevity. On the example the correlation function calculated for fluorescent beads diffusing in water (Figure 2.2), we discuss the key features of FCS correlation curves [34]. At very short times, the auto-correlation shows a significant excess correlation ($G'(\tau) > 0$). The auto-correlation is comparatively constant until it rolls off monotonically at a characteristic time of ≈ 0.1 ms for the chosen example. At large times the excess auto-correlation rolls-off to $G'(\tau) = 0$, or equivalently, the auto-correlation rolls off to 1. The correlation contrast at zero time is given by $G'(0) = \left[\langle C \rangle \, \pi^{3/2} \, \sigma_1 \, \sigma_2 \, \sigma_3\right]^{-1}$. Here we can identify an effective detection volume $V^* = \pi^{\frac{3}{2}} \, \sigma_1 \, \sigma_2 \, \sigma_3$. Given this definition, the contrast at zero time is simply the inverse of the mean number of emitters in the detection volume. For the example chosen in figure 2.2, the excess correlation is 0.2, meaning 5 molecules in the effective detection volume.

The roll-off time τ^*, which we define as $G'(\tau^*) = \frac{1}{2} G'(0)$, corresponds to the average residence time of the fluorophore in the detection volume. If the size of the detection volume is known, τ^* allows to retrieve the diffusion coefficient.

In FCS literature, one often finds a further simplification that is considered appropriate for fitting experimental data [10, 34]. This simplification consists of the assumption that the focus has cylindrical symmetry around the optical axis, so that one can take $\sigma_1 = \sigma_2 = \sigma$. The larger extension of the focus along the optical axis is typically captured by a parameter s, setting $\sigma_3 = s\sigma$. Commonly the resulting analytical expression for the correlation function is fitted to measured data, taking as three independent fit parameters the correlation contrast, the parameter $\sigma / \sqrt{4D}$ that sets the timescale, and the asymmetry parameter for the focus, s. These parameters can subsequently be interpreted in terms of $\langle C \rangle$ and D provided one has further knowledge of the focus size σ and shape s. The asymmetry parameter s can be viewed as a consistency check for the fit, as it should be of order 2 for a high NA focus.

Another useful fact is that, independent of the detailed shape of the MDF or the dynamics of the fluorophore, the total correlation contrast at $\tau = 0$ is always given by

$$G'(0) = \frac{1}{\langle C \rangle} \frac{\iiint \mathrm{MDF}(\mathbf{r})^2 d\mathbf{r}}{\left(\iiint \mathrm{MDF}(\mathbf{r}) d\mathbf{r}\right)^2} \, .$$

which is the inverse of the average number of molecules $\langle N \rangle$ in the effective detection volume V^*. This yields a generalized effective detection volume

$$V^* = \frac{\left(\iiint \mathrm{MDF}(\mathbf{r})\, d\mathbf{r}\right)^2}{\iiint \mathrm{MDF}(\mathbf{r})^2\, d\mathbf{r}} \,.$$

2.2 Literature review

Standard FCS implementations employ a single diffraction limited detection volume to deduce the mobility of particles due to the mean diffusion time through the known focus volume. Accurate knowledge of the focus size and shape is required to correctly retrieve the kinetic properties of the specimen of interest. In literature there are two approaches for this calibration. One sidesteps the issue by using a solution with fluorophores of known concentration and kinetic properties. One can then directly relate a measured ratio in correlation contrast to a ratio in concentrations, and similarly one can then deduce a ratio of diffusion constants from the ratio in roll off times. However, this approach really avoids, rather than tackles, the question of how to accurately interpret FCS data, since ultimately using a reference sample only shifts - but does not remove - the calibration burden. Hence several authors have embarked on actually measuring focus shapes and including deviations from the Gaussian shape approximation in FCS theories. In addition, others have explored schemes that deliberately go beyond single Gaussian focus FCS in attempts to extend the application domain of FCS. In this section we briefly review the literature treating on the one hand corrections to standard Gaussian FCS theory (section 2.2.1), and on the other hand extensions to FCS (2.2.2).

2.2.1 Corrections to standard FCS theory

The assumption of a 3D gaussian MDF is not always justified. We therefore review literature employing non-gaussian MDFs in the presence of free diffusion. In the original FCS experiment in 1972, Magde, Elson and Webb [31] assumed a cylindrical volume of infinite length along the optical axis and with a gaussian cross-section given by the intensity distribution of the laser focus, and derived analytic expressions for this MDF [31]. In fact, even if one can assume a Gaussian transverse profile of the focus, the established theory of paraxial Gaussian beams [39] states that the energy density in the third dimension (along the optical axis) is neither cylindrical nor Gaussian. Instead it has a Lorentzian shape. Analytical expression for this case can also be found, even though they are mathematically more complex [40]. While paraxial Gaussian beam optics might have been appropriate to describe the experiment [31] of Magde, Elson and Webb who used a focus as large as 5.5 μm micron across (NA $\approx$ 0.04), it certainly does not apply to focusing by a high NA objective. Hence, Enderlein [41] has calculated FCS traces taking into account the full focal shape of a high NA focus, which typically includes sidelobes, and is not cylindrically symmetric due to polarization effects. Furthermore, microscopy inevitably has to contend with aberrations, such as spherical abberations due to coverslips, or astigmatism that can occur due to misalignment. These have been treated in [41]. In actual laboratory practice, these aberration effects in Gaussian fits to FCS data are often seen as unphysical values

of the asymmetry parameter s. Finally, for sufficiently high excitation power, one may encounter saturation, which effectively reduces the molecular detection function in regions of high pump intensity. This has been dealt with by Gregor et al. in [42].

In the past decade, many experiments have also been performed to reduce the detection volume below the diffraction limit [43], e.g. by employing an evanescent wave at a glass water environment in a total internal reflection microscope [44], or by 4Pi- microscopy employing coherent illumination with high numerical aperture from two sides [45, 46].

2.2.2 Conceptual extensions to FCS

2.2.2.1 Dual Focus FCS

In dual focus FCS (2fFCS), the intensity fluctuations originating from two spatially separated volumes are measured and then cross-correlated. 2fFCS has proven to be a robust method to measure absolute diffusion coefficients, due to the fact that the distance between the two detection volumes can be precisely known in an experiment, even if the exact shape of the foci is prone to aberration and thus not exactly known [47, 48]. The known distance between the MDFs provides an intrinsic reference which allows the measurement of the absolute diffusion coefficient without a reference measurement. The normalized cross-correlation function for a dual focus FCS experiment with two displaced molecular detection function MDF_1 and MDF_2 is given by

$$G_{CC}(\tau) = \frac{\iiint MDF_1(\mathbf{r}) \iiint MDF_2(\mathbf{r}') \cdot \langle \delta C(\mathbf{r},0)\, \delta C(\mathbf{r}',\tau) \rangle \, d\mathbf{r}' d\mathbf{r}}{\langle C \rangle^2 \iiint MDF_1(\mathbf{r}) d\mathbf{r} \cdot \iiint MDF_2(\mathbf{r}) d\mathbf{r}} \, .$$

Assuming a gaussian shape $MDF_i(\mathbf{r}) = \Gamma(\mathbf{r}, S_i, \mathbf{R_i}, \sigma_\mathbf{i})$, with $i = 1,2$ for the first and second MDF, and free diffusion in 3D gives the cross-correlation function

$$G_{CC}(\tau) = \frac{1}{\langle C \rangle} \prod_{k=1,2,3} \left(\frac{\sqrt{2}}{\sqrt{\pi}\sqrt{\left(\sigma_{1,k}\right)^2 + \left(\sigma^D_{2,k}(\tau)\right)^2}} \exp\left[\frac{-2\left(\mathrm{R_{1,k}} - \mathrm{R_{2,k}}\right)^2}{\left(\sigma_{1,\mathrm{k}}\right)^2 + \left(\sigma^{\mathrm{D}}_{2,\mathrm{k}}(\tau)\right)^2} \right] \right). \qquad (2.5)$$

A cross-correlation function calculated with eq. (2.5) is shown in fig. 2.3. The typical feature of dual focus FCS is that the cross-correlation does not roll-off monotonically, as the auto-correlation does, but instead can show a maximum at a characteristic time τ_{peak}. This timescale can be identified as the time required to diffuse from one detection volume to the other. Thereby, the spatial separation between the focus sets a calibration for the timescale in the measurement. As an example, we derive the characteristic properties of the cross-correlation function for two spherical gaussians $\Gamma_1(\mathbf{r}, S_1, [0,0,0], \sigma)$ and $\Gamma_2(\mathbf{r}, S_2, [0,0,R_0], \sigma)$ of widths σ with a center-to-center displacement of R_0. The peak time is then given by

$$\tau_{peak} = \frac{1}{12} \frac{2R_0^2 - 3\sigma^2}{D} \, , \qquad (2.6)$$

and the peak height equals $G_{CC}(\tau_{peak}) = \langle C \rangle^{-1} \left(\frac{3}{2\pi \mathrm{e}}\right)^{\frac{3}{2}} |R|^{-3}$, independent of the width σ of the gaussians. At $\tau = 0$ the cross-correlation is given by $G_{CC}(0) = \exp\left(-R^2/\sigma^2\right)\left(\sqrt{\pi}\sigma\right)^{-3}$

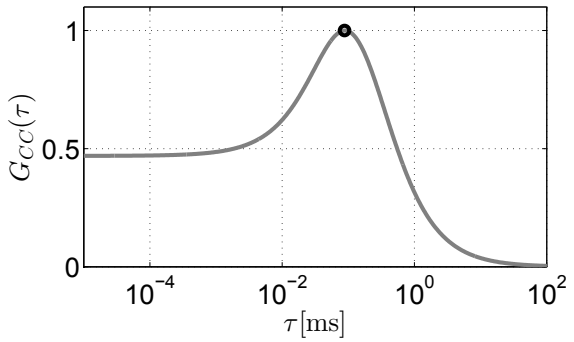

Figure 2.3: Calculated cross correlation function for emitters performing free diffusion ($D = 1 \cdot 10^{-9}\,\mathrm{cm}^2/\mathrm{s}$) in a liquid with two displaced spherical gaussian MDFs (width: 300 nm, center-to-center distance: 500 nm). The value of the cross correlation function at the τ_{peak} is indicated by the black circle.

and is given by the overlap integral of the two Gaussians, normalized by $S_1 S_2$. If $G_{CC}(\tau_{peak}) < G_{CC}(0)$, then no peak is visible, and the cross-correlation function shows a roll-off similar to the auto-correlation function.

2.2.2.2 Species discrimination FCS

Another type of extension of the FCS concept provides discrimination of different species diffusing in the same solution. If the solution under investigation is not homogeneous and contains species of different diffusion characteristics, a measured correlation curve shows a superposition of the single-species correlation functions. The number of species in the solution can be obtained by fitting a superposition of a set number of correlation curves. This method is prone to errors, and requires a minimal difference in the diffusion time of the different species [49]. A solution to this is the use of dual-color FCS [50]. If two different species can be labeled with different fluorescent markers, the fluorescence can be spectrally separated to different detectors. Typically a dual-color FCS experiment employs two lasers with wavelengths matching the absorption spectra of the two fluorescent labels. In the detection channel, a dichroic mirror separates the emission spectra of both fluorophores before two detectors. This allows to obtain simultaneously the correlation function of each species. The cross correlation between the two detectors shows if the species are bound together. Due to the broad emission spectrum of organic fluorescent labels, the number of possible detection channels in multi-color FCS is limited.

To allow the separation of different species within the same spectral region, changes in the fluorescence lifetime can be used. In Fluorescence Lifetime Correlation Spectroscopy [51, 52] one uses a pulsed excitation source and acquires a time-resolved histogram of the fluorescent emission. The histogram then allows to retrieve the contribution of the different species in the focus. Furthermore, this technique has been used to separate the diffusion of fluorophores close to an interface from the fluorescence in the bulk. Contribution to the fluorescence signal originating from labeled lipids could be disentangled into signal from a lipid bilayers at the interface and from the bulk liquid, as the interface was coated with a fluorescence quencher to introduce a difference in fluorescence lifetime [53].

2.2.3 Nanostructure enhanced FCS

All the previously mentioned systems use conventional objectives to create the detection volume. Since the correlation contrast scales inversely with the mean number of emitters in the detection volume, this sets a limit to the maximum concentration at which a correlation curve can be measured. Taking the diffraction limit as the smallest attainable volume, one finds that FCS requires concentrations, at most, in the nanomolar range. As plasmonics allows to confine electromagnetic fields in volumes much smaller than the diffraction limit, the suitability of metal nano-structures for FCS has been tested by many groups [54]. Since Levene et al. used a nanometric aperture in an aluminum film [32] to measure kinetic processes, with high correlation contrast at micro molar concentrations, nano-apertures are now extensively studied. Rigneault et al. characterized the influence of the aperture diameter in the reduction of the detection volume of aluminum nano-apertures [55]. Wenger et. al. investigated how the radiative and non-radiative decay rates of a fluorophore are altered in the aperture, and how the intrinsic quantum yield of the fluorophore relates to fluorescence enhancements of the nano-aperture [36, 56]. Further, the effect of the excitation polarization on the fluorescence emission in a rectangular aperture was investigated [33]. The nano-aperture design was improved by Aouani et al. by corrugating the surroundings of the aperture with a pattern of concentric rings [20, 57]. Here, the essential physics is that a dominant loss channel in nano-aperture FCS, is that part of the fluorescence in the nano-aperture is coupled into surface plasmon polariton waves that are bound surface waves that ultimately get absorbed without contributing to far-field signal. Thus, the periodic corrugation provides the momentum required to recuperate the surface plasmons as photons, by scattering them into the microscope objective. Additionally, the corrugation provides highly directional emission.

The main strength of nano-aperture enhanced FCS, is that the use of a nano-aperture in a thick metal film imposes a strong geometrical confinement for the pump light, irrespective of any plasmonic effects. In fact, even when field enhancements in a nano-aperture are moderate, a large reduction in volume of the MDF is obtained. Several researchers have also attempted to obtain improved FCS using the inverse structure, i.e., nano-particles instead of nano-apertures. However, without the blocking effect of the metal film, it is much more difficult to obtain a reduction in detection volume, as one obtains an MDF that is the sum of the bare background focus, and the plasmon-enhanced near-field of the antenna. Yet, in FCS measurements with colloidal particles as antennas, reductions of the detection volume ranging from 2 to even as high as 10^4 have been claimed [58–60]. In self assembled nano-islands made of silver, a factor of 10 in reduction of the detection volume has been measured [61]. Next to a single gold nano-rod, 1000× enhancement of fluorescence brightness was observed from low quantum efficiency dye slowly diffusing in glycerol [62]. In antennas with bow-tie geometry, fluorescence enhancements of a factor of 1000 were measured with immobilized fluorophores [15]. In FCS experiments with the same type of antennas [63], similarly high count rate enhancements were observed, but the detection volume reduction could not be reliably determined due to the fact that molecules suffered from non-diffusive kinetics. Indeed, several experiments on plasmon-antenna enhanced FCS [16, 60, 63] reported sticking of molecules to the glass/antenna surface. A recent experiment in which a large reduction in detection volume was obtained, and in

which sticking effects were verified to be absent was reported by Punj et al. [64]. This experiment combines the merits of a nano-aperture, and of a nano-particle antenna. Punj et al. placed a dimer antenna inside a subwavelength nano-aperture, so that the dimer provides strong field enhancement, while the aperture blocks background fluorescence. A reduction of the detection volume of 4 orders of magnitude compared to the diffraction limit was obtained.

2.3 Correlation contrast of the full field of a Mie sphere

To obtain some intuition on how a nano-antenna modifies the fluorescence in a tight focus, here we consider a Mie-sphere [65]. The exact molecular detection function (MDF) near a gold sphere, when illuminated by a focused beam, is calculated. To construct the full MDF three functions need to be calculated. First, the excitation efficiency function (EEF) which is given by the intensity distribution of the excitation field. Second, the local quantum efficiency $\eta(\mathbf{r})$ which quantifies the fraction of decays with the emission of a photon. Third, the collection efficiency function CEF, which quantifies the probability that a photon emitted at a given position is detected. From the MDF we calculate the effective detection volume, and the related correlation contrast which can be achieved by an FCS experiment.

2.3.1 Field profile of a gold sphere in focus

First we calculate the field distribution around the nano-antenna to obtain the excitation efficiency function. The near-field of a spherical scatterer excited by a plane wave polarized along x and propagating along the z-axis is exactly given by

$$\mathbf{E}_{\text{Mie}} = \mathbf{E}_x e^{ikz} + \sum_{n=1}^{\infty} \sum_{m=-n}^{n} [a_n \mathbf{N}_{nm}(r,\theta,\phi) + b_n \mathbf{M}_{nm}(r,\theta,\phi)] \tag{2.7}$$

where a_n and b_n are the well known Mie coefficients and where $\mathbf{N}_{nm}(r,\theta,\phi)$, $\mathbf{M}_{nm}(r,\theta,\phi)$ are the vector spherical harmonic basis functions as completely specified by C. T. Tai and many other textbooks [66]. We construct the near field of the Au particle in a focused field by linear superposition, starting from the notion that a high NA focus can be represented as a sum of plane waves. We use the formulation of Novotny and Hecht [39]

$$\mathbf{E}_f(x,y,z) \propto \iint_{|\mathbf{k}_{||}|<\text{NA}\cdot|k|} E(k_x,k_y) \begin{pmatrix} k_y^2 + k_x^2 k_z/|k| \\ k_x k_y (k_z/|k| - 1) \\ -(k_x^2 + k_y^2) k_x/|k| \end{pmatrix} \frac{1}{|\mathbf{k}_{||}|^2 \sqrt{|k| k_z}} e^{i\mathbf{k}_{||}\cdot(x,y) + i k_z z} d\mathbf{k}_{||}$$

where $k_z = \sqrt{|k|^2 - |\mathbf{k}_{||}|^2}$, $|k| = \omega/c$ and $\mathbf{k}_{||} = (k_x, k_y)$, and where the field incident on the back-aperture of the high-NA focusing lens was taken to be x-polarized with amplitude distribution $E(k_x, k_y)$, assumed constant over the back aperture in this work. We generate the field in and around the focus by tabulating the plane wave Mie solution (terms up to $n = 45$) for an x-polarized wave incident along z, and use that as a look up table to find the full complex vectorial field for any incident plane wave using interpolation. The integral is

approximated as a discrete sum, sampling the back aperture (up to $\sin\theta = 0.95$ in water, corresponding to an NA= 1.26) with 1800 incident wave vectors. For the Mie calculation we take optical data from Johnson and Christy [67] and assume as wavelength 568 nm, the Ar/Kr laser line closest to the plasmon resonance of the sphere. Figure 2.4b shows

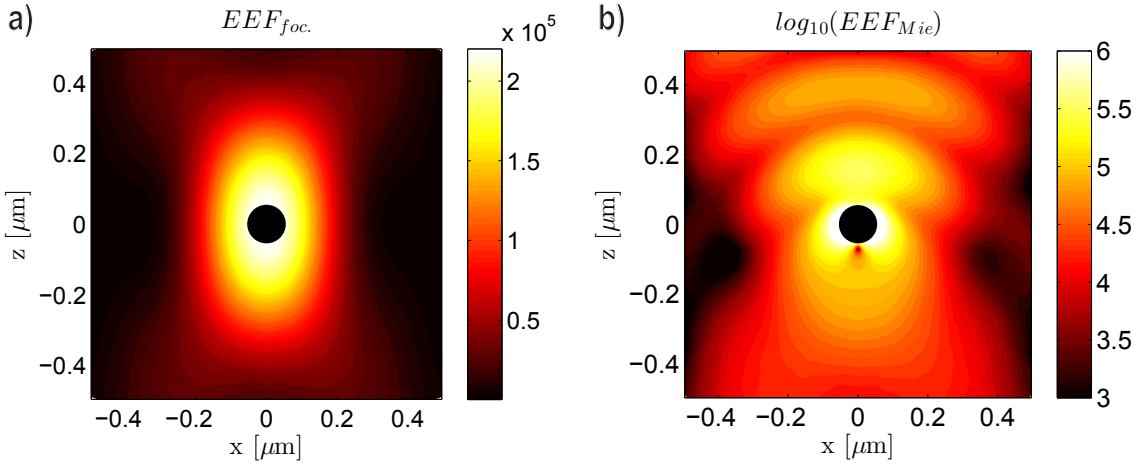

Figure 2.4: a) calculated focal field intensity in absence of the Mie particle from plane wave reconstruction assuming $\lambda = 568$ nm, $n = 1.33$ and an input $NA = 0.95n = 1.26$. Cut shown is in the xz plane, with x-polarized illumination incident from above. b) calculated total field in presence of the ø100 nm Au sphere. The color scale is logarithmic, spanning four orders of magnitude and reaching up to a field intensity enhancement of around 40 compared to the bare focus, attained at the particle edge, and decaying within 10 nm when moving away from the particle. Note the standing wave pattern on the incident side ($z > 0$).

a cross cut in the xz-plane of the electromagnetic field intensity around the Au sphere. For reference fig. 2.4a shows the field distribution $|E|^2$ in absence of the Mie sphere. As expected, the coherent superposition of plane waves results in a diffraction-limited focus. Figure 2.4b shows the calculated intensity distribution in the presence of the nano-particle, which is the EEF, the first factor of the wanted MDF. At the particle surface, a enhancement of $|E|^2 \sim 13$ over the incident field is obtained in two lobes on either side of the particle along the polarization direction, as expected for a dipole resonance. A standing wave pattern is evident on the incident side $z > 0$. Strong reflection by the particle forms a standing wave, as is expected from the high scattering efficiency of large Au nano-particles on resonance, that present a cross-section close to the diffraction limit.

2.3.2 Role of LDOS and quantum efficiency

According to $MDF(\mathbf{r}) = CEF(\mathbf{r}) \cdot \eta(\mathbf{r}) \cdot EEF(\mathbf{r})$, the next step in composing the MDF is to include the quantum efficiency of the emitter. Quantum efficiency is defined as the fraction of decays, from the excited state, which yield a photon in the far-field. A plasmon nano-particle can change the quantum efficiency of a nearby fluorophore significantly since it can accelerate radiative decay as well as induce quenching [7, 68, 69]. Let us denote with γ_{tot} the total decay rate and quantum efficiency η_0 assumed for the fluorophore in absence of any plasmonic structure. The associated radiative and non-radiative rates are

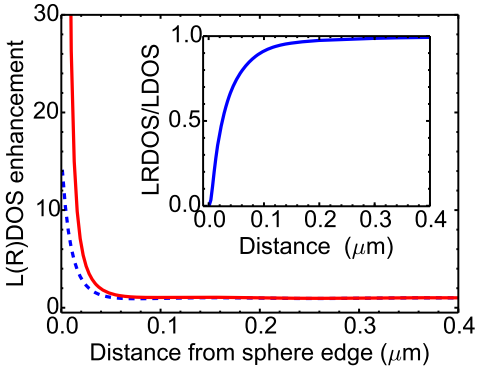

Figure 2.5: Enhancement of the local density of states (LDOSe) and radiative part of the local density of states enhancement (LRDOSe), both normalized to the host LDOS, as function of distance to the Au sphere. The inset shows the ratio of the two, which is equivalent to the quantum efficiency of emission, assuming one brings a unit quantum efficiency emitter in proximity of the sphere.

$\gamma_r = \eta_0 \gamma_{\text{tot}}$ and $\gamma_{nr} = (1-\eta_0)\gamma_{\text{tot}}$. In presence of the plasmonic structure, the total decay rate will be

$$\gamma_{\text{tot}}(\mathbf{r}) = \gamma_{nr} + \gamma_r \text{LDOSe}$$

while the radiative part of this enhanced rate is given by

$$\gamma_r(\mathbf{r}) = \gamma_r \text{LRDOSe}.$$

Here we have introduced two new quantities, namely LDOSe and LRDOSe. The first quantity, LDOSe[†], is the local optical density of states as introduced by Sprik et al. [70]. The second quantity LRDOSe is the radiative part of the local density of states as introduced by Mertens et al. [68]. Physically, the LDOSe represents the number of photon modes available for the emitter to emit into, as needed in the summation over all final states in Fermi's Golden Rule. The quantity LRDOSe is needed to account for the fact that some of the electromagnetic decay channels involve quenching, so that LRDOSe ≤ LDOSe.

$$\eta(\mathbf{r}) = \frac{\gamma_r(\mathbf{r})}{\gamma_{\text{tot}}(\mathbf{r})} = \frac{\eta_0 \text{LRDOSe}(\mathbf{r})}{1 + \eta_0(\text{LDOSe}(\mathbf{r}) - 1)}.$$

This equation summarizes the well known facts that (1) at unit intrinsic quantum efficiency, the quantum efficiency of the coupled system reads LRDOSe/LDOSe < 1, implying no efficiency enhancement, and at worst even significant quenching of efficient emitters by metal surfaces, (2) at very low intrinsic quantum efficiency ($\eta_0 \ll 1$), the quantum efficiency may be significantly enhanced.

Figure 2.5 shows the calculated orientation-averaged LDOSe and LRDOSe for the Au sphere at hand in this work, as calculated using the analytical formulas in Ref. [68]. A finite LRDOSe enhancement of nearly 15 can be obtained at the sphere surface. The

[†]Strictly with LDOS(R)e we indicate enhancement of LDOS(R), as obtained by normalizing to the LDOS of free space. In nano-optics one often uses 'LDOS' and 'LDOS enhancement' interchangeably.

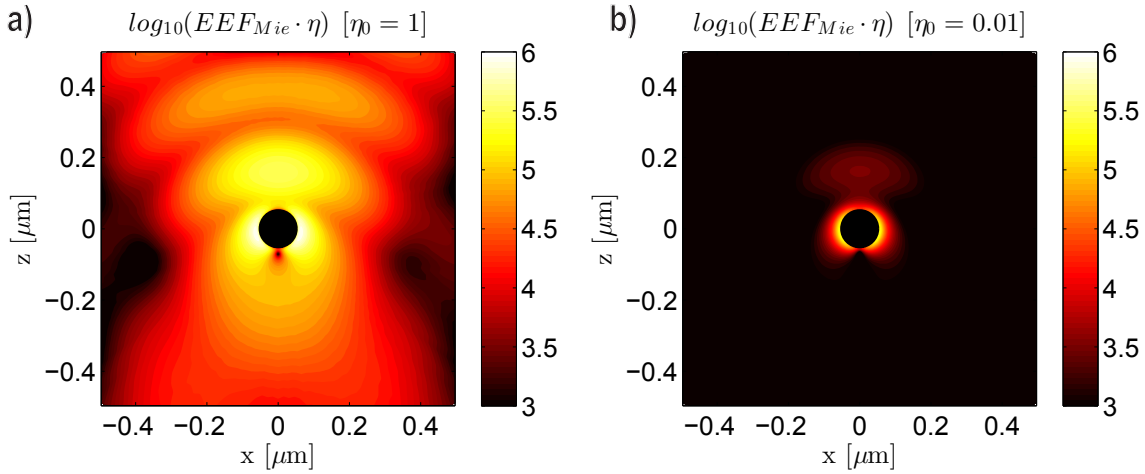

Figure 2.6: Excitation efficiency function multiplied by the local quantum efficiency $\eta(\mathbf{R})$ for two different intrinsic quantum efficiencies a) $\eta_0 = 1$ and b) $\eta_0 = 0.01$.

LDOS diverges and hence the effective quantum efficiency of emission for any emitter reaches zero at the metal surface.

Having calculated the local quantum efficiency $\eta(\mathbf{r})$, we multiply it to the EEF to see which spatial dependence is added by the quantum efficiency. In the remainder, we consider the MDF for two typical limits, i.e., a low quantum efficiency emitter $\eta_0 = 0.01$ and a high quantum efficiency emitter ($\eta_0 = 1$). Figure 2.7 shows $EEF(\mathbf{r}) \cdot \eta(\mathbf{r})$ (panels a,b) in the xz-plane. If one starts with a unit quantum efficiency fluorophore (fig. 2.7a), we find no enhancement compared to a bare focus, as coupling to the particle simply reduces the quantum efficiency. In contrast, if one starts with a very poor quantum efficiency emitter ($\eta_0 = 0.01$, fig. 2.7b), the probability of emission, given that it is excited, can be boosted approximately 5-fold, due to the LRDOS enhancement by the particle. The maximum emission boost occurs at a distance of about 10 nm away from the metal surface, as quenching dominates at closer distances [68]. Consequently, the apparent MDF right at the particle surface vanishes, but it reaches a maximum that is approximately 5.5-fold enhanced compared to the MDF one would have for a dye molecule centered in a free focus.

2.3.3 Collection Efficiency Function

The collection probability for photons, given that a molecule is excited at $\mathbf{r}$ also depends on position. In a true confocal scheme, if one uses the same diffraction limited pinhole or single mode fiber through which to illuminate and detect, and assuming a negligible Stokes shift between emission and absorption, reciprocity applies to relate the calculated pump focus distribution to the detection probability enhancement, even in presence of the metal nano-particle. Reciprocity ensures that the enhanced field locally set up by a focused beam incident from afar, conversely means that a classical current dipole, of given strength at the same location, radiates power with the same enhancement factor back into the incident mode [71]. However, a molecule is not a fixed current source, but rather emits at most one photon per excitation cycle [7, 71, 72], as a constant power source. Thus, dividing by the

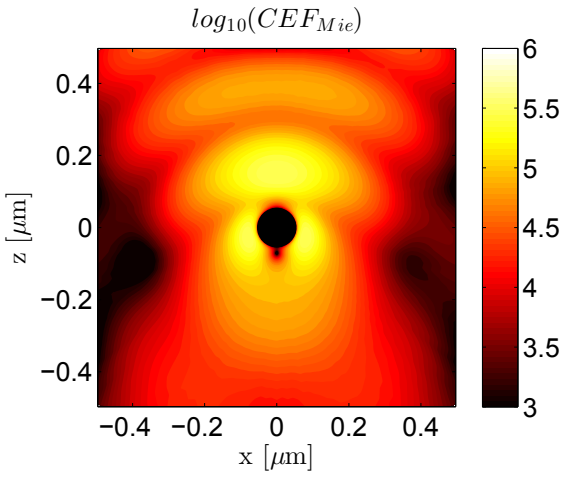

Figure 2.7: Collection efficiency function $CEF(\mathbf{r}) = |\mathbf{E}_{\text{NP+focus}}|^2/\text{LDOSe}(\mathbf{r})$.

local density of optical states yields the correct collection efficiency function for a constant power source, as realized by a unit-quantum efficiency molecule in absence of any intrinsic or nano-structure induced quenching. The collection efficiency function CEF then reads

$$\text{CEF}(\mathbf{r}) = \frac{|\mathbf{E}_{\text{NP+focus}}|^2}{\text{LDOSe}(\mathbf{r})} = \frac{\text{EEF}(\mathbf{r})}{\text{LDOSe}(\mathbf{r})}$$

where LDOSe is the "local density of optical states" that quantifies the power radiated by a constant current source in classical electrodynamics and the enhancement of radiative decay rates for spontaneous emission.The CEF is shown in fig. 2.7. Close to the surface of the gold sphere, the CEF is *reduced* compared to the EEF due to the increased local density of states.

2.3.4 Molecular detection function

Having constructed the excitation efficiency function, the local quantum efficiency and the collection efficiency function, we can construct the full molecular detection function

$$\text{MDF}(\mathbf{r}) = \text{EEF}(\mathbf{r})\,\eta(\mathbf{r})\,\text{CEF}(\mathbf{r})\ .$$

Figure 2.8 shows cuts through the MDF in the xz-plane. For low quantum efficiency, the MDF is tightly confined. For the case of an efficient emitter, the MDF is much less strongly confined, as field enhancement at the particle is countered by the strong quantum efficiency reduction near the particle. Notably, the first maximum of the reflected standing wave in front of the particle is a strong contributor to the MDF. We note that this observation further implies that FCS measured through a coverslide, on which particles reside, should strongly depend on illumination direction, and should be quite different from FCS on particles in a bulk liquid, as the accessibility of the standing wave lobe differs.

Having calculated the MDF for a given intrinsic quantum efficiency, we can obtain the corresponding effective detection volume

$$V^* = \frac{(\iiint \text{MDF(r)}\,dr)^2}{\iiint \text{MDF(r)}^2\,dr}\ .$$

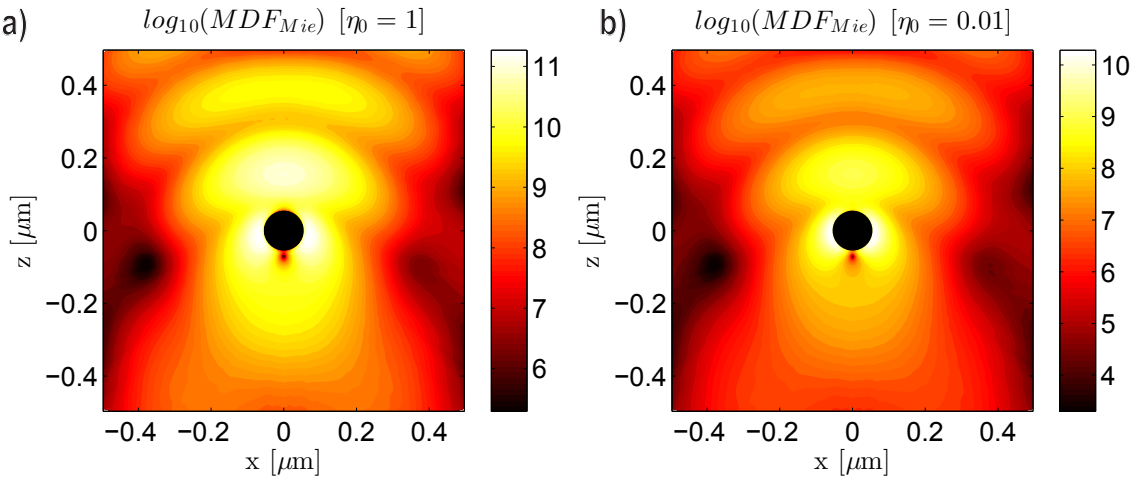

Figure 2.8: Full molecular detection functions calculated as the product of the excitation field intensity, the local quantum efficiency and the collection efficiency function for emitters of a) 100% and b) 1% intrinsic quantum efficiency. Note that the MDF only occupies a small volume in the case of a low efficiency emitter.

Assuming spherical symmetry of the hotspot we can relate this volume to a width of the hot-spot via $V^* = [\sqrt{\pi}\,\sigma]^3 \approx [1.8\sigma]^3$. In figure 2.9 we compare the effective detection volumes of the MDF in a confocal measurement scheme, with and without nano-particle, including their dependency on the intrinsic quantum efficiency η_0 of the used fluorophores. For all MDFs we exclude the volume in which the plasmon particle resides.

For the focus without the nano-antenna, in a confocal detection scheme ($MDF(\mathbf{r}) = EEF(\mathbf{r})^2\eta_0$), the effective volume is given by $[\sqrt{\pi}\cdot 0.44\,\mu\text{m}]^3$ and does not depend on the quantum efficiency. Now we turn to the detection volume in the presence of the gold sphere when assuming a confocal detection scheme ($MDF(r) = EEF_{Mie}(\mathbf{r})\,\eta(\mathbf{r})\,CEF_{Mie}(\mathbf{r})$). At unity quantum efficiency we find a detection volume of $[\sqrt{\pi}\cdot 0.32\mu\text{m}]^3$, which is a factor just

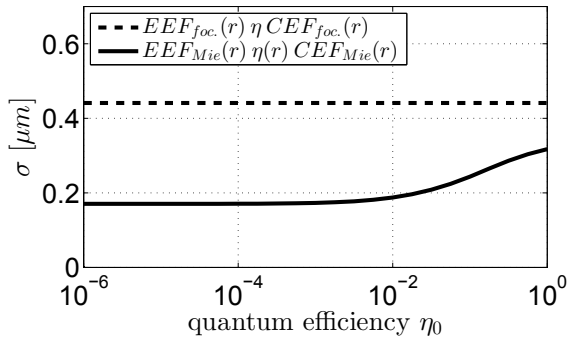

Figure 2.9: Effective detection volumes V^* of two different MDFs by plotting the dimension $\sigma = \sqrt{\pi}^{-1}\,\sqrt[3]{V^*}$ of a spherical gaussian with equal detection volume. The NA=1.2 focus in water with confocal detection in absence of the nano-antenna with an excluded volume of the 100nm sphere in its center (dashed line). In the absence of the nano-antenna the detection volume does not depend on the quantum efficiency and the CEF is identical to the EEF. The black line show the effective detection volume in a confocal detection scheme in the presence of the nano-antenna.

2.5 smaller than in the confocal scheme without the antenna. When reducing the quantum efficiency to $\eta_0 = 1\%$, the detection volume shrinks to a volume of $[\sqrt{\pi} \cdot 0.19\,\mu\text{m}]^3$. This corresponds to a volume reduction, and equivalently a correlation contrast enhancement of $12.5\times$ compared to the confocal detection without nano-antenna. Reducing the quantum efficiency further does not reduce the effective detection volume significantly. One has to keep in mind that the countrate for all measurement scenarios scales with quantum efficiency. Hence working with low quantum efficiency dyes does result in the smallest detection volume in antenna-enhanced FCS, but at the price of loss in intensity.

3

Modelling plasmon-enhanced fluorescence correlation spectroscopy

3.1 Introduction

One of the promises of plasmonics is the improvement of sensing schemes at the single molecule level. Impressive advances have been made towards this goal utilizing different physical properties, such as refractive index changes [73], surface-enhanced raman spectroscopy [74], or fluorescence spectroscopy [10, 34, 69]. The detection of fluorescently labeled specimens can profit threefold from properly designed plasmonic antennas: first, a plasmonic antenna can increase the excitation rate by enhancing the local pump-field; second, the antenna can funnel the fluorescence emission into a certain direction or polarization state; and third, for fluorophores with low intrinsic quantum efficiency the offered additional photonic states of the antenna can greatly improve the quantum yield [7, 75].

Fluorescence correlation spectroscopy [31] (FCS) is widely used to locally investigate the diffusion coefficient of single molecules. FCS exploits random fluorescence intensity fluctuations that occur as individual molecules diffuse in and out of focus in a confocal measurement configuration. These random fluctuations are correlated on a time scale given by the diffusion constant. By its very nature, diffusion measurements via FCS require the number of detected molecules (fluorophores in the diffraction limited focus) to fluctuate significantly due to brownian motion, which limits the maximal concentration at which FCS measurements can be performed with a standard diffraction limited excitation volume. This limitation can be overcome by employing plasmonic antennas for light. Two quintessential geometries have emerged for plasmon enhanced FCS: nano-apertures and nano-antennas. Small nano-apertures in a metal film [76, 77], effectively block background signal by an optically thick metal layer. They have proven to be very useful for FCS measurements [20, 32, 78, 79] by shifting the limit of the highest concentration at which measurements are possible by 2-3 orders of magnitudes, towards physiologically relevant concentrations [17].

This improvement is mostly due to the geometric confinement of the detection volume. Nano-antennas [16, 80] also localize fields in deep-sub-wavelength volumes, but do not provide an effective suppression of the excitation focus in the solute, which reduces the benefits of the strong field confinement around the antenna in fluorescence fluctuation measurements, unless the intensity enhancement at the antenna is very large. Several reports have recently claimed FCS enhancement with plasmon antennas, notably including the bow tie antenna [63] famous for its large field enhancement, as well as simple colloidal metal nano-particles [58–60, 81], or self assembled silver nano-islands [61].

In this chapter, we model the effect of nano-antennas (or any other object causing a non-gaussian intensity distribution) on fluorescence fluctuation measurements, and identify which configurations can actually improve an FCS measurement. In section 3.2 we derive expressions which allow to calculate the auto-correlation functions for arbitrary detection volumes and find similarities to expressions derived for dual focus fluorescence cross correlation spectroscopy [82]. In section 3.3 we apply our model to nano-antenna enhanced FCS experiments by constructing a simplified MDF made up of only two Gaussian constituents: one representing the diffraction limited '*background focus*', as in standard FCS, and a second smaller Gaussian '*hotspot*' which represents the confined and enhanced near-field intensity created by the nano-antenna. Exemplified by this model system, we quantify the benefits for FCS measurements that can be obtained depending on the intensity enhancements and sizes of the hotspot. We predict the suitability of realistic nano-antennas to improve an FCS measurement by mapping their near-field parameters, extracted from literature, onto our parameter phase space diagram. In the last section we discuss in which cases the total correlation function can be used to extract information about the hotspot size and/or intensity. Finally, we identify the limits at which it is valid to interpret a nano-antenna enhanced FCS measurement with a simple single focus FCS model.

3.2 Fluorescence fluctuation correlation

We briefly recapitulate standard FCS theory and the definition of the molecular detection function and the correlation functions, as we have derived in Chapter 2, section 2.1.3. In a typical fluorescence correlation spectroscopy measurement [31], a collimated laser is focused by a microscope objective in a solution of fluorophores which undergo brownian motion. The fluorescence signal is picked up through the same objective, passes a spectral filter to block the scattered laser light, and the fluorescence is then detected on a sensitive detector and stored as a function of time. The temporal fluctuations in the fluorescence intensity originate from single molecules randomly entering and leaving the focus. The stochastic trajectories are reflected in temporal fluctuations in the fluorescence signal $F(t)$.

The fluorescence intensity $F(t)$ is linked to the spatial distribution of fluorophores $C(\mathbf{r}, t)$ by the molecular detection function (MDF): $F(t) = B \int \mathrm{MDF}(\mathbf{r})\, C(\mathbf{r}, t) \mathrm{d}^3\mathbf{r}$ [10]. The MDF($\mathbf{r}$) describes the spatial dependence of the detection efficiency of a fluorophore at certain position $\mathbf{r}$. It is defined as the product of the excitation probability $EEF(\mathbf{r})$, the local quantum efficiency $\eta(\mathbf{r})$, and the probability to detect fluorescence originating from the same position, quantified by the collection efficiency function CEF($\mathbf{r}$). In standard

FCS applications, the MDF is approximated as a single 3D Gaussian Γ determined by its strength S, center position $\mathbf{R}$ and width in each dimension σ

$$\Gamma(\mathbf{r}, S, \mathbf{R}, \sigma) = \left(\frac{2}{\pi}\right)^{\frac{3}{2}} \frac{S}{\sigma_1 \sigma_2 \sigma_3} \exp\left[-2 \sum_{k=1,2,3} \left(\frac{r_k - R_k}{\sigma_k}\right)^2\right].$$

The correlations in the fluorescence intensity fluctuations are extracted by auto-correlating the fluorescence intensity $G(\tau) = \langle F(t)\, F(t+\tau)\rangle / \left[\langle F(t)\rangle \langle F(t)\rangle\right]$ where the angle brackets denote the average of the signal over time $\langle F(t)\rangle = T^{-1} \int_0^T F(t)\, \mathrm{d}t$

$$G(\tau) = \frac{B^2 \int \mathrm{MDF}(\mathbf{r}) \int \mathrm{MDF}(\mathbf{r}') \left\langle \delta C(\mathbf{r}, 0)\, \delta C(\mathbf{r}', \tau)\right\rangle \mathrm{d}^3\mathbf{r}' \mathrm{d}^3\mathbf{r}}{\left[B \langle C\rangle \int \mathrm{MDF}(\mathbf{r}) \mathrm{d}^3\mathbf{r}\right]^2} + 1. \tag{3.1}$$

Here $\left\langle \delta C(\mathbf{r}, 0)\, \delta C(\mathbf{r}', \tau)\right\rangle$ is the probability to find a fluorophore at time $t+\tau$ on position $\mathbf{r}'$, when it was located at $\mathbf{r}$ at time t. In the case of free translational diffusion, which we will assume throughout this thesis, this term is given by the solution of the diffusion equation $\left\langle \delta C(\mathbf{r}, 0)\, \delta C(\mathbf{r}', \tau)\right\rangle = \langle C\rangle (4\pi D\tau)^{-\frac{3}{2}} \exp\left[-\left(\mathbf{r} - \mathbf{r}'\right)^2 / (4\, D\, \tau)\right]$ where D is the diffusion coefficient, and $\langle C\rangle$ the average concentration of the fluorophores.

Using the solution of the diffusion equation, and a gaussian MDF, allows an analytical solution of Eq. (3.1) which then reads [10, 34]

$$G'(\tau) = \left[\langle C\rangle \prod_{k=1,2,3} \sqrt{\pi} \sqrt{4\, D\, \tau + \sigma_k^2}\right]^{-1}.$$

where we have introduced $G'(\tau) = G(\tau) - 1$ for convenience in notation.

3.2.1 Molecular detection functions of arbitrary shape

In a nano-antenna enhanced FCS experiment, an antenna is positioned in the focus of a tightly focused laser beam to locally enhance the pump field as well as the detection probability [20, 32, 59, 64, 76, 77, 79, 83]. Generally, the presence of the antenna results in a MDF that is not simply gaussian. We now introduce a framework to calculate the auto-correlation $G'(\tau)$ for such an MDF. Since a single Gaussian MDF allowed an easy mathematical treatment (Chapter 2, section 2.1.3), we propose to describe any MDF as a sum of gaussians

$$\mathrm{MDF}(\mathbf{r}) = \sum_{i=1}^{N} \Gamma_i(\mathbf{r}) = \sum_{i=1}^{N} \Gamma(\mathbf{r}, S_i, \mathbf{R}_i, \sigma_{\mathbf{i}}). \tag{3.2}$$

It is evident that such a Gaussian expansion can approximate any MDF with arbitrary precision, since in the limit of $\sigma \to 0$ the Gaussians tend to δ-functions, which form a complete set.

In a plasmon enhanced FCS experiment, we would choose the first Gaussian Γ_1 to correspond to the diffraction limited pump spot, as in standard FCS. We add the local pump field enhancement of the nano-antenna with one narrower Gaussian Γ_2. More Gaussians

can be added to map the pump field distribution more accurately, or to account for the suppression of fluorescence emission by quenching in close proximity to the metal surface.

Inserting a sum of Gaussians (Eq. (3.2)) into the general definition of the normalized autocorrelation function (Eq. (3.1)) yields:

$$G'(\tau) = \frac{1}{\langle C \rangle \, S_{MDF}^2} \left[\Sigma_n A_{n,n}(\tau) + \Sigma_{n \neq m} A_{n,m}(\tau) \right] \tag{3.3}$$

with $(n, m = 1 \ldots N)$. The square brackets consists of N^2 summands, each of them a volume integral of the product of two Gaussians $A_{n,m}(\tau) = \int \Gamma_n(\mathbf{r}) \cdot \Gamma_m^D(\mathbf{r}, \tau) \, \mathrm{d}^3\mathbf{r}$. As in Eq. (3.1), the second Gaussian Γ_m is broadened by the convolution with the diffusion kernel. Since the diffusion kernel is also gaussian with a τ-dependent width, the convolution yields again a Gaussian

$$\Gamma_m^D(\mathbf{r}, \tau) = \Gamma\left(\mathbf{r}, S_m, \mathbf{R}_m, \sigma_m^D(\tau)\right) = \Gamma_m(\mathbf{r}) * (4\pi D\tau)^{-\frac{3}{2}} \exp\left[-\left(\mathbf{r} - \mathbf{r}'\right)^2 / (4\,D\,\tau) \right]$$

with a τ-dependent width of $\sigma_{m,k}^D(\tau) = \sqrt{{\sigma_{m,k}}^2 + 8\,D\tau}$, with $*$ denoting convolution. The volume integral $A_{n,m}(\tau)$ is then given by

$$A_{n,m}(\tau) = S_n \, S_m \prod_{k=1,2,3} \left(\frac{\sqrt{2}}{\sqrt{\pi} \sqrt{\left(\sigma_{n,k}\right)^2 + \left(\sigma_{m,k}^D(\tau)\right)^2}} \exp\left[-2 \, \frac{(\mathrm{R_{n,k}} - \mathrm{R_{m,k}})^2}{\left(\sigma_{\mathrm{n,k}}\right)^2 + \left(\sigma_{\mathrm{m,k}}^{\mathrm{D}}(\tau)\right)^2} \right] \right). \tag{3.4}$$

The overall normalization factor in Eq.(3.3) is given, as in a normal single focus FCS, by the square of the volume integral of the entire MDF times the concentration $\langle C \rangle \, S_{MDF}^2 = \langle C \rangle \left[\Sigma_{n=1}^N S_n \right]^2 = \langle C \rangle \left[\Sigma_{n=1}^N \int \Gamma_n(\mathbf{r}) \, \mathrm{d}^3\mathbf{r} \right]^2$. Equation (3.4) can be applied to a vast variety of FCS experiments with nontrivial intensity distributions, e.g. standard single focus FCS at intensities where fluorescence saturates in the focus [42], multifocus FCS [47, 82] or an FCS experiment with a complex intensity distribution, as it occurs with nano-antennas. The decomposition into Gaussians allows calculating the auto-correlation function (ACF) for any MDF.

We recognize two different types of contributions: $A_{n,n}$ terms correspond to the standard single focus FCS measurements in each Gaussian, whereas the $A_{n,m}$ $(m \neq n)$ correspond to contributions of diffusion from one Gaussian to another, as it is established in dual-focus cross correlation FCS experiments [82]. In the case of pure diffusive transport, it can be rigorously shown that $A_{n,m}(\tau) = A_{m,n}(\tau)$, thus the number of independent summands reduces to $\frac{1}{2}N(N+1)$. While the ACF obtained from an FCS measurement of *multiple species* in a single focus [10, 84] shows strong similarities to Eq. (3.3), it lacks the crossterms $A_{n,m\,(n\neq m)}$. As we will see in Fig. 3.3(a) in the following section, the crossterms can have a higher contribution to the correlation function than the associated diagonal terms. Therefore, employing a multi-species model for a multi-gaussian detection experiment as done in [58, 59] to explain the ACF for a plasmonic structure can lead to erroneous results. The cross-terms are well known in dual focus FCS [47], where one creates two spatially separated diffraction limited foci from which autocorrelations $A_{n,n}$ and cross correlations $A_{n,m}$ can be separately measured. For plasmon-antenna enhanced

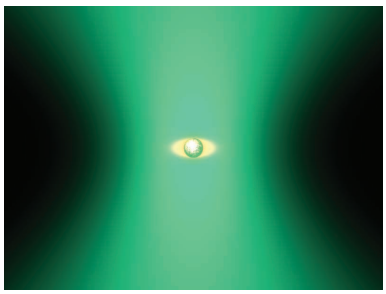

Figure 3.1: Schematic of a non-Gaussian MDF: a focused laser beam (green) illuminates a metallic nano-particle (center) which gives rise to field enhancement in its vicinity (orange).

FCS, however, only the sum of all terms can be measured, as the fluorescence from all gaussians that construct the MDF is detected in only one detection channel.

3.3 Two coinciding Gaussians

We now apply our formalism to the case of plasmon-enhanced FCS. In particular, we consider a scenario where a plasmonic antenna is illuminated by a focused laser beam, as illustrated in Fig. 3.1. If the excitation wavelength overlaps with an antenna resonance, the electric field intensity $|E_2|^2$ will be locally enhanced close to the antenna as compared to the intensity in absence of the antenna $|E_1|^2$.

We show in section 3.4 how this field-enhancement contributes to the total correlation contrast. In particular, we calculate how one should optimally design the enhancement and volume of a plasmonic hotspot to obtain the highest $G'(\tau = 0)$ at a given concentration. This is of large importance in the quest to apply FCS at physiological concentrations [17]. Afterwards, we investigate (section 3.4.1) how the antenna affects the roll-off time of $G'(\tau)$ for $\tau > 0$. This question is relevant from two distinct viewpoints: on the one hand, given a known solution of fluorophores, one can ask how trustworthy an FCS measurement is to determine the hotspot size and volume. On the other hand, one can ask how suitable a given plasmon antenna, in order to accurately determine the concentration and diffusion constant of a given solute.

In order to answer these questions we consider a simple model of plasmon-enhanced FCS. For the sake of simplicity we compose the MDF as the superposition of only two coinciding spherical Gaussians ($\mathbf{R_1} = \mathbf{R_2}$; $\sigma_{n,1} = \sigma_{n,2} = \sigma_{n,3}$), one representing a diffraction limited focus Γ_1, and the other representing the locally enhanced near-field Γ_2 with smaller width ($\sigma_2 < \sigma_1$). Figure 3.2(a) shows a typical example of such a scenario. Superimposed in the center of a focus of 500 nm width we consider a hot spot 50 nm across, reaching an intensity enhancement of $|E_2|^2/|E_1|^2 \approx 30$ at its peak position, a typical value for a metal nano-sphere. By this we assume that the increase of the MDF is only caused by the near-field intensity enhancement $P_2/P_1 = |E_2|^2/|E_1|^2$. Quenching could be easily incorporated into the model by including an additional, and even narrower Gaussian, with negative peak height to the sum. Calculations (not shown) with a third Gaussian to account for quenching have shown negligible influence of the quenching on the total correlation function in the

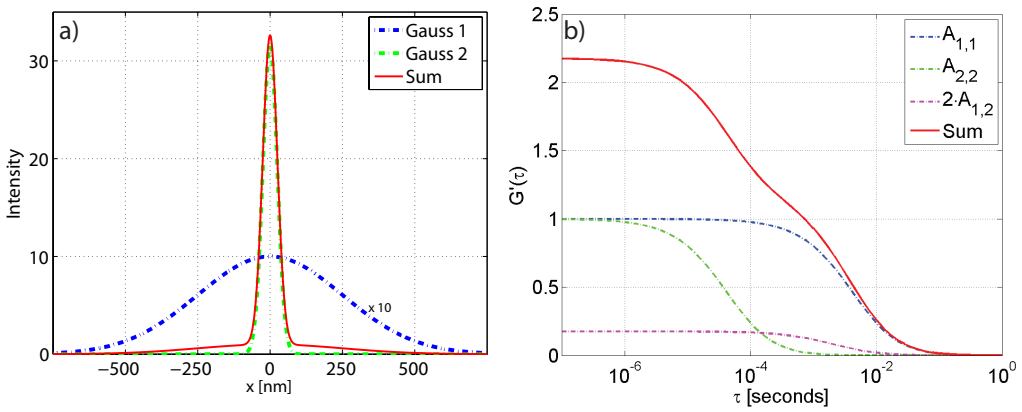

Figure 3.2: a) Crosscut though a MDF (red line) constructed of two Gaussians: a wide Gaussian (blue dashed line, width: $\sigma_1 = 500$ nm; peak height: $P_1 = 1$; integral: $S_1 = 0.7\mu\text{m}^3$), representing a diffraction limited focus, and a narrow Gaussian (green dashed line; $\sigma_2 = 50$nm; $P_2 = 31$; $S_2 = 0.023\mu\text{m}^3$) mimicking a 'hot spot' of a plasmonic nanoparticle. b) Calculated autocorrelation function for the entire MDF (red solid line) and its constituents: the autocorrelation of the background focus $A_{1,1}$ (blue dashed line), the hotspot $A_{2,2}$ (green dashed line) and the sum of the identical cross-terms $2\,A_{1,2}$ (magenta dashed line).

scenario presented in Fig. 3.2. The calculated $G'(\tau)$ (Fig. 3.2(b), red solid line) clearly shows an enhanced contrast (the diffraction limited Gaussian only (not shown) would show a contrast of 1), consisting of three contributions: $A_{1,1}$ (blue dashed line) the contribution of the background focus and $A_{2,2}$ (green dashed line) the contribution from the hotspot. In addition the contribution of the two identical cross-terms $A_{1,2}$ and $A_{2,1}$ is not negligible (magenta dashed line). Furthermore, we see that the hotspot reduces the roll-off time. The ratio $\sigma_2/\sigma_1 = 10^{-1}$ translates into a ratio of effective volumes of $V_2^*/V_1^* = 10^{-3}$. Thus, the hotspot *alone* would exhibit a correlation contrast 1000× higher than the focus volume, whereas the superposition illustrated in Fig. 3.2(a) shows a correlation contrast only twice as large as the bare focus. This shows the importance of properly accounting for the background focus when conducting an antenna-enhanced FCS measurement.

3.3.1 Different contributions to the total correlation contrast

We now proceed to find the ideal parameters for the hotspot in order to enhance the total correlation contrast. Because the total correlation contrast is inversely proportional to the concentration of fluorophores, increasing the contrast by utilizing a hotspot allows to measure at higher concentrations, at a given signal to noise ratio. To understand when the correlation contrast is maximum, we extract the relative contributions of the hot spot and the background focus. To compare their relative contributions, we calculate $A_{n,m}$ at $\tau = 0$ for $n = m = 1,2$. With $\mathbf{R_1} = \mathbf{R_2}$ Eq. (3.4) simplifies to

$$A_{n,m}(0) = S_n\, S_m \prod_{k=1,2,3} \frac{\sqrt{2}}{\sqrt{\pi}\sqrt{\sigma_{n,k}^2 + \sigma_{m,k}^2}}. \tag{3.5}$$

For summands with $n = m$ the expression further reduces to

$$A_{n,n}(0) = \frac{S_n^2}{\pi^{3/2}\,\sigma_{n,1}\,\sigma_{n,2}\,\sigma_{n,3}} = \frac{S_n^2}{V_n^*}\ . \tag{3.6}$$

This shows that a hot spot of 10× smaller width (1000× smaller volume) than the background focus, contributes as much to the total correlation contrast as the background focus, if the hot spot has a peak intensity $\sqrt{1000} \approx 30\times$ higher than the background focus. This is exactly the case we have illustrated in Fig. 3.2.

As can be seen in Fig. 3.3(a) (red curves), the cross terms $A_{1,2}(0)$ (dash-dotted line) clearly exceed the background focus contribution $A_{1,1}(0)$ (dashed line) for $\sigma_2/\sigma_1 > 0.2$, although they remain below the diagonal hot spot contribution $A_{2,2}(0)$ (dotted line). Generally, the cross term never exceeds the largest diagonal term, but it can significantly exceed the smaller of the two diagonal contributions. Throughout all figures subsequent to 3.3(a) we plot the complete G', that is the sum of all contributions.

3.4 Total correlation contrast

In this section, we analyze the contrast at zero time as a function of the hot spot parameters. Figure 3.3 shows how the total correlation contrast $G'(\tau = 0)$ depends on the width and peak intensity of the hot spot. All calculations shown in this chapter were performed with a background focus of $\sigma_1 = 500\,\text{nm}$ width, a peak height of $P_1 = 1$ and a diffusion coefficient $D = 10^{-11}\ \text{m}^2\text{s}^{-1}$. Figure 3.3(a) displays the total correlation contrast (solid lines) for hot spots with three different peak intensities $P_2 = 1$, 10 and 32 as a function of the relative width σ_2/σ_1. As expected, the higher the field enhancement, the higher the contrast boost that can be achieved. For a hot spot with ten-fold peak enhancement (solid green line) we observe that the total correlation contrast can be increased from 1 to 4, when the hot spot is a third of the size of the diffraction limited spot ($\sigma_2 = 150$ nm). For a peak enhancement of 32 (solid red curve) the correlation contrast can exceed 9 for a hot spot width of $\sigma_2 = 100$ nm ($\sigma_2/\sigma_1 = 1/5$). Surprisingly, we find that there is an optimum size at which the highest correlation contrast is achieved. This optimum shifts with increasing enhancement factor to smaller hot spot sizes. If a hot spot is too small its contribution to the total fluorescence signal is too small to influence $G'(\tau)$. If, on the other hand, the hot spot is too big (about the size of the focus field), there is no reduction in effective volume, thus no increased correlation contrast.

Figure 3.3(b) provides an overview of $G'(0)$ in a large parameter space in a color plot with logarithmic color scale, taking the width ratio σ_2/σ_1 as the horizontal and the peak ratio P_2/P_1 as the vertical axis. We explore the content of this phase diagram by means of a few limiting cases. At the right hand side of the diagram, at $\sigma_2/\sigma_1 = 1$, the hot spot has the same width as the Gaussian, which is equivalent to just increasing the amplitude of the MDF but leaving its shape unaltered. The ACF is not affected by scaling the amplitude of the MDF, thus $G'(0) = 1$, independent of P_2/P_1. In other words, there is no point offering any field enhancement, unless it is confined to a fraction of the focus. A horizontal cut at $P_2/P_1 = 1$ (blue line) corresponds to a hot spot with the same peak amplitude as the background Gaussian. Walking on a line from right to left corresponds to reducing the size

of this hot spot, keeping its amplitude constant at 1. As can be seen in Fig. 3.3(a) (blue solid line) this improves the total contrast merely from 1 to ≈ 1.3 at $\sigma_2/\sigma_1 \approx 0.6$. Further reducing σ_2/σ_1 makes the contribution of the hot spot vanish. While reducing the hot spot does induce even stronger relative fluctuations in the hot spot fluorescence by having fewer molecules, reducing the number of molecules by confinement ultimately means that they simply provide insufficient photon counts compared to those in the background focus. If we now consider a vertical cross section at $\sigma_2/\sigma_1 = 10^{-1}$ while increasing the field intensity enhancement, we find that at first the contrast barely increases. However, when crossing the horizontal red line at $P_2/P_1 = 32$ the contrast doubles to $G'(0) \approx 2$, meaning that the hot spot has gained enough intensity to contribute the same amplitude to the total correlation function as the background focus (as in Fig. 3.2). Further increasing the peak intensity value of the hot spot greatly improves the total correlation contrast, until it saturates at $P_2/P_1 \approx 10^4$ approaching $G'(0) \approx 1000$, associated with the 1000 times smaller volume of the hot spot. For even higher enhancements the $G'(\tau)$ is fully determined by the signal from the hot spot and the background focus is not relevant anymore.

We notice that on horizontal cross sections, at any given peak enhancement, there is an optimal size of the hot spot to maximally increase the total correlation contrast, exactly as seen in the cross cuts in Fig. 3.3(a). The gray dashed line in Fig. 3.3(b) indicates the optimum hot spot size for each peak enhancement. The optimum shifts to smaller hot spot sizes for larger enhancements. We can thus analyze where actual plasmonic antennas

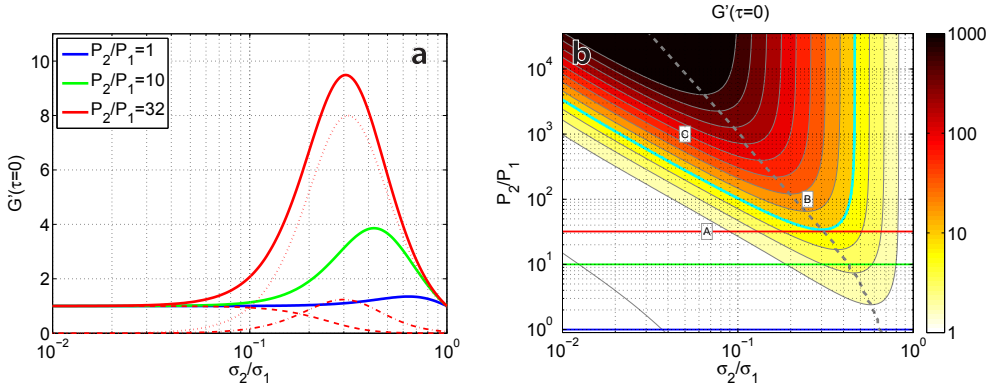

Figure 3.3: The background focus is kept constant at $\sigma_1 = 500$ nm and $P_1 = 1$ whereas the parameters of the hot spot are varied. a) The total correlation contrast $G'(0)$ (solid lines) for three different peak to peak ratios. For the red curve ($P_2/P_1 = 32$) we additionally show its constituents: $A_{1,1}$ (dashed line), $A_{2,2}$ (dotted line) and $2\,A_{1,2}$ (dash-dotted line). In the range of ideal correlation contrast enhancement for a given peak intensity enhancement, the cross term $A_{1,2}$ can have a stronger influence on the total correlation function than the background focus $A_{1,1}$ itself. The time dependence of the red curves at $\sigma_2/\sigma_1 = 10^{-1}$ is shown in Fig. 3.2(b).
b) Shows how the total correlation contrast depends on the relative width σ_2/σ_1 and relative peak intensities P_2/P_1. The cyan line indicates where the total correlation contrast is 10× enhanced compared to the bare background focus. Crosscuts along the blue, green and red lines corresponds to the solids lines in Fig. 3.3 of the same colors. The gray dashed line shows which relative width yields the maximum contrast for given peak intensities. The labels A,B,C denote realistic antenna parameters from literature listed in Table 3.1.

reside in this diagram. Fluorescence fluctuation measurements have recently been reported for Au-spheres, bow-tie antennas and nano-rods [16, 59, 63]. For the bow-tie and nano-rod antennas we have estimated the field enhancement and extent from literature calculations and for gold nano-spheres we have calculated these using analytical Mie theory [65]. The hot spot parameters extracted (or calculated) for these three realistic antennas are compiled in Table 3.1. The labels *A*, *B* and *C* in Fig. 3.3(b) show where these antennas reside in our hot spot parameter space. Evidently, Mie spheres (label *A*) supply poor intensity enhancement and are too confined to yield optimal FCS enhancement. This is consistent with the experimental findings of a total correlation contrast enhancement of $\approx 2\times$ and $\approx 12\times$ for gold colloids in [58] and [59], taking into account the different quantum efficiencies used in the experiments. Estrada et al. have claimed measurable correlation contrast assisted by a gold colloid (∅80 nm) in a 150 μM dye-solution, i.e. at '10^4 times the concentration used in standard experiments' [60]. The reported experiment could not pinpoint the origin of the enhanced correlation, and an equal contribution of altered molecule kinetics by sticking at interfaces and reduced diffusion volume, is suggested by the authors. Our model suggests that the reduced volume for freely diffusing particles is unlikely to have such a strong effect in the described system.

Nano-rods (label *B*) perform much better than Mie spheres due to their higher intensity enhancement. The bow tie antenna (label *C*) seems ideal, and our model predicts that a 1000-fold increase in correlation contrast might be reached. It should be noted that in the experimental realizations of the latter two antennas [16, 63], the fluorescence fluctuation signal was afflicted by 'sticking' of the fluorophores to the particle or substrate surface. Thus, those experimental correlation functions can not be compared with our model which only includes free diffusion. A recent experiment by Punj et al. [64] has quantified the correlation enhancement for a so called 'antenna in a box', a particle dimer antenna enclosed in a rectangular void in a gold film. They established detection volumes down to 60 zl, meaning a 30× contrast enhancement compared to a reference measurement that utilized the same rectangular void but without bow-tie. This reference measurement in itself already implied a 100-fold reduced detection volume compared to a free focus.

	Structure	σ_2	$(E_2/E_1)^2$	λ_0	$\sigma_1 = \lambda_0/2$	σ_2/σ_1
A	Au sphere	20 nm	32	580 nm	290 nm	1/15
B	single nanorod	80 nm	100	620 nm	310 nm	1/4
C	Bow Tie antenna	20 nm	1000	780 nm	390 nm	1/20

Table 3.1: Properties of gold nano-antennas in literature: A) Gold Mie sphere (ø100 nm); near field intensity enhancement was calculated and σ_2 was approximated by the cubic root of the calculated effective mode volume; B) single nanorod ([85], Fig. 2(b) inset), hot spot diameter approximated by rod diameter; C) Bow tie antenna [63], hot spot diameter approximated by the gap size. All hot spot diameters were put into ratio to the extend of the background focus given by a diffraction limited focus of $\sigma_1 = \lambda/(2\,\mathrm{NA})$ assuming a NA=1 objective.

3.4.1 Roll-off time of $G'(\tau)$

The correlation contrast at zero time is important because it directly determines the maximal concentration at which fluorescence fluctuation measurements can be performed. However, measuring a diffusion constant requires the measurement of the roll off time of $G'(\tau)$. On the one hand one can ask how suitable a given plasmon antenna is to determine the concentration and diffusion constant of a solute accurately. On the other hand, given a known solution, it is interesting to check how trustworthy an FCS measurement is to determine the hot spot volume from a measured diffusion time. We define the effective diffusion time τ^* as the time when $G'(\tau)$ has dropped to half its maximum value $G'(\tau^*)/G'(0) = 1/2$. Figure 3.4(a) shows the effective diffusion time as a function of the hot spot parameters.

Again, we explore the meaning of Fig. 3.4 by walking along limiting cases. When the hot spot is the size of the background focus ($\sigma_2/\sigma_1 = 1$), the diffusion time is unaffected because the shape of the MDF is unchanged. When the enhancement is very low (e.g. $P_2/P_1 = 1$), the diffusion time is dominated by the background focus, and shrinking the hot spot further does not change τ^*. Whenever the enhancement is high (e.g. $P_2/P_1 = 10^4$), the total correlation function $G'(\tau)$ is dominated by the hot spot, and τ^* then scales like $\propto (\sigma_2)^2$. Now assume we increase the hot spot intensity for a given size (e.g. $\sigma_2/\sigma_1 = 0.1$) starting from $P_2/P_1 = 1$: for a weak hot spot the diffusion time is determined by the background focus. Increasing the hot spot intensity to ≈ 30, we find a steep transition for τ^* at the point when both hot spot and background focus contribute equally to $G'(\tau)$ (close to label *A*). As we further increase the hot spot intensity, τ^* saturates at the diffusion time of the bare hot spot.

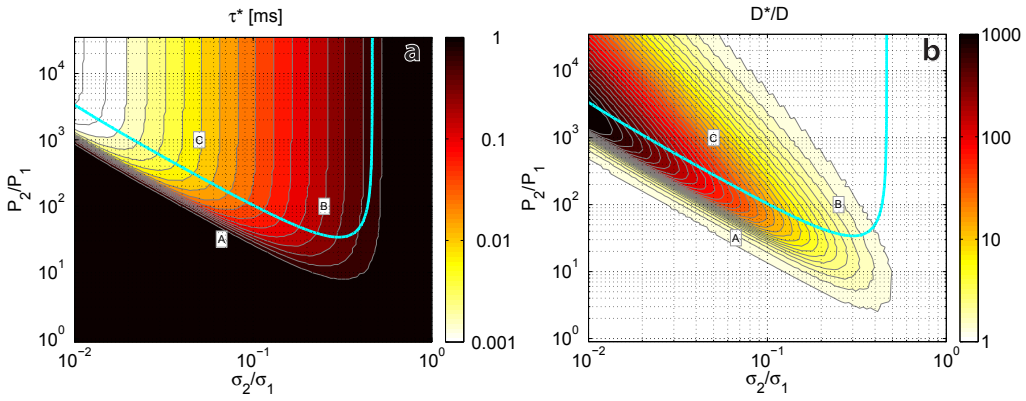

Figure 3.4: a) Shows how the effective diffusion time τ^* of the total correlation function depends on the hot spot size and amplitude. The apparent diffusion coefficient D^* was extracted from $G'(0)$, τ^* and known concentration assuming a single focus FCS experiment. b) Shows the ratio D^*/D_0 of the apparent divided by the real diffusion coefficient, showing a possible misjudging of 1000× in the calculated parameter range. The cyan lines (from Fig. 3.3(b)) shows the parameters for which the total correlation contrast in enhanced 10×.

3.4.2 Retrieval of electromagnetic parameters of the hot spot

Having explored how the parameters $G'(0)$ and τ^*, which characterize $G'(\tau)$, behave for different hot spot parameters, we now investigate in which cases we can safely deduce information about the hot spot from the total correlation function $G'(\tau)$. Since fitting experimental data with a closed expression for $G(\tau)$ with a given number of Gaussians to experimental data is expected to be error-prone, we attempt to retrieve information from parameters which can be extracted robustly: first, the total correlation contrast $G(0)$, and second, the effective diffusion time τ^*.

We assume a calibrated solution of known diffusion coefficient and concentration which could, for instance, be measured via a standard single focus FCS measurement in the same solution without the antenna. Performing a measurement with the antenna would yield a different correlation contrast $G'(0)$ and diffusion time τ^*. But since the concentration is known, the correlation contrast $G'(0)$ would allow to retrieve the effective volume V^*. If the correlation contrast is more than 10× enhanced (above the cyan contour line in Fig. 3.3(b) and Fig. 3.4(a,b)) the measured diffusion time τ^* would be in good approximation determined by the hot spot. This can be seen in Fig. 3.4(a) as τ^* does not change with changing field enhancement anymore. Thus, in this case one could deduce the extent σ_2 of the hot spot by the measured diffusion time and the known diffusion coefficient D, neglecting the background focus. Having determined σ_2 one has essentially fixed the position on the horizontal axis in our color plots. If the boost in correlation contrast is not at the limit of the bare hot spot of $(\sigma_2/\sigma_1)^{-3}$, meaning the contour lines in Fig. 3.3(b) are *not* vertical yet, then this value of $G'(0)$ corresponds to a unique peak enhancement P_2/P_1 for the antenna. In other words, an FCS measurement on an antenna in a calibrated solution allows to retrieve the size and the peak enhancement of the hot spot just by extracting $G'(0)$ and τ^*, if the temporal shape of $G'(\tau)$ is dominated by the hot spot, but only if the enhancement $|E_2|^2/|E_1|^2$ is modest.

3.4.3 Retrieval of the diffusion coefficient

Converse to asking when the total correlation function allows reading off hot spot properties, we may ask in which conditions the antenna enhanced FCS can be used to measure the diffusion coefficient of an unknown solute. If the very same antenna was calibrated in a reference measurement (with known diffusion coefficient D_0 and concentration C_0) the measurement of the unknown solution can be compared to the reference and hence the diffusion time and total contrast can be related to the diffusion constant and concentration of the reference. It should be noted, that due to the dispersive character of a plasmonic antenna the calibration has to be carried out within the same dielectric environment (refractive index of the solvent) with a fluorophore showing the same absorption and emission spectrum as well as the same quantum efficiency as the target solution. Moreover, we expect that one should use exactly the same antenna, as field enhancements may vary strongly between nominally identical antennas. Such a calibration is hence a significant challenge.

If a full calibration of the nano-antenna is not possible, one might nonetheless attempt to derive analyte properties by using the temporal dependence of $G'(\tau)$. For instance, one might attempt to determine the diffusion constant, given a solute of known concentration,

on basis of the correlation at zero time delay and the roll-off time. As an example, suppose that only the average concentration C_0 would be known and that one would calculate the diffusion coefficient from $G'(0)$ and τ^*. This would proceed as follows. First, from C_0 and the total correlation contrast $G'(0)$, one would calculate the effective volume $V_{eff} = \left(G'(0)\, C_0\right)^{-1}$. Assuming spherical symmetry this would yield an effective width of the Gaussian $\sigma_{eff} = \pi^{-1/2}\, V_{eff}^{1/3}$. Next, one would convert the measured roll off time τ^* into a diffusion constant $D^* = (\sigma^*)^2/(4\,\tau^*)$. Figure 3.4(b) shows the ratio D^*/D_0 of the calculated diffusion coefficient divided by the real diffusion constant used in the calculations. We see that the diffusion coefficient might be misjudged by a factor of 1000 when interpreting the correlation curve as in a single focus FCS experiment. Only in two limits does this retrieval yield a correct diffusion coefficient. These two cases are on the one hand, when the hot spot does not affect the $G'(\tau)$ at all, namely at low peak enhancements, or on the other hand at very high peak enhancements when the hot spots totally dominate $G'(\tau)$, which is the case in regions where the contour lines in Fig. 3.3(b) *and* Fig. 3.4(a) are vertical. Unfortunately, especially for the regions in parameter space relevant to realistic plasmonic antennas, this procedure would yield diffusion coefficients up to a factor 100 higher than the real values.

3.5 Conclusion

We have presented a mathematical framework to treat fluorescence correlation measurements of systems with a non-gaussian Molecular Detection Function, as in the case of nano-antenna enhanced FCS measurements. In a plasmonic environment the MDF is the product of the pump field intensity, the detection efficiency and the quantum efficiency. All these quantities are dependent on position, and require the spatial mapping of the electromagnetic field at the excitation wavelength, at the emission wavelength, and the local density of optical states at the emission frequency. Once obtained, the MDF can be decomposed into Gaussians and the expressions we derived allow an analytical treatment of simple problems as well as efficient numerical handling for MDFs of arbitrary complexity.

For the example of a plasmon enhanced FCS experiment approximated by two Gaussians, mimicking the diffraction limited background focus and the nano-antenna hot spot, we discussed how the hot spot affects the total correlation function. Marking realistic values for plasmonic hot spot sizes and peak amplitudes in our calculations allows the prediction of their benefit for FCS applications. We found that a bow tie antenna can outperform a Mie sphere by two orders of magnitude in terms of increasing the total correlation contrast, since its field enhancement is 30× higher than the Mie sphere. Further, we showed that for a given hot spot peak intensity there is an optimal size at which the total correlation contrast becomes maximal. Characteristic parameters of the correlation function, such as total contrast and diffusion time scale differently with the hot spot width or peak height. This has severe implications: even if the total correlation function seems to be dominated by the hot spot –exhibiting strongly increased contrast or significant reduction of the diffusion time– this does, in general, not allow to interpret the total correlation function as in a single focus FCS experiment, but rather leads to diffusion coefficients orders of magnitude different from the real value. We identify hot spot parameter regimes in which an interpretation

of the correlation curve as in a single focus experiment is tolerable, yielding correct results. Our model is a versatile tool to efficiently predict how non-gaussian intensity distributions alter fluorescence fluctuation measurements. As such, it allows to benchmark proposed antenna designs for FCS against the requirements that MDF enhancements of at least around 10^2 are obtained, and that the antenna sustains such a high MDF over a sufficiently large volume to maximally improve the FCS contrast. This is by no means an easy challenge, as large MDF enhancements typically involve narrow gaps.

Part II

Spatial information encoded in non-intensity observables

4

Mapping of emitter position into far-field observables

4.1 Introduction

In the past two decades super-resolution (SR) fluorescence microscopy has revolutionized the imaging of biological systems. SR techniques have quickly evolved in easy-to-use microscopes which are commercially available, allowing fluorescence imaging with resolutions at least 10× higher than the diffraction limit [86]. SR microscopy has already become an indispensable tool to study biological systems, and therefore three inventors of SR techniques have been awarded the Nobel prize in chemistry in 2014.

The awarded techniques break the diffraction limit via two different basic principles. The first principle is used by photo activated localization microscopy and stochastic optical reconstruction microscopy [87, 88]. It consists of building up an image by taking a large set of frames, where in each frame only a small, random subset of molecules is fluorescent while all the other emitters are inactive. If the active emitters have separations above the diffraction limit, one can localize them with nanometer accuracy, not limited by diffraction, but only by photon count. Merging frames hence leads to a superresolved image. The method requires an (in)activation mechanism to ensure that only few molecules fluoresce at a time, which is typically attained via photoswitchable molecules. The second principle (named stimulated emission depletion microscopy) is to perform confocal scanning with two overlapping beams, one conventional focus to excite the fluorescence and the second (of ring-shaped cross-section) which actively suppresses the fluorescence into the detector by stimulated emission [89]. This results in a confocal volume much smaller than given by the diffraction limit. Both techniques win in resolution at the expense of measurement time. Consecutive imaging of N subsets increases the acquisition time of the full image at least by a factor of N. Furthermore, a reduced confocal volume requires a reduced step-size in the confocal scanning. However, many biological processes happen too fast to image them with these SR techniques. One purpose of microscopy is to measure distances

between objects and their fluctuations in time. Images with confocal resolution or the above-mentioned SR techniques are instead designed to provide extended 2D maps of spatial distributions. If one does not require information on a large field of view, but rather on the distance between two objects, alternative techniques can be used that can be much faster. For example, Förster Resonant energy transfer (FRET), a technique that allows fast measurement of the distance between two fluorescent markers in distance range of a few nanometers [90]. In particular, since FRET only measures *distances* and not 3D *coordinates* or displacement vectors, it can not be used to trace out trajectories.

In this chapter we propose a technique which allows the localization of fluorophores in the near-field of a metallic nano-antenna, typically in a volume 50 nm around the antenna surface. Our technique does not require scanning of the incident beam and only relies on far-field observables. Thus, it can be easily incorporated into standard fluorescence microscopes. Additionally, it allows fluorophore localization with respect to a fixed reference coordinate system given by the nano-antenna.

In the following section 4.2, we describe the geometry of the sample under consideration and the observables we are interested in. In Section 4.3 we explain the computation methods, numerical simulations and the post processing used. Sections 4.5-4.7 show the results for the different far-field observables, such as intensity, polarization, back focal plane intensity distribution and fluorescence lifetime.

4.2 Model system

We highlight model geometries which are realistic and easy candidates for experimental realization. Therefore, we choose as geometry a gold colloid of 100 nm diameter immobilized on a glass surface and surrounded by water. In a homogeneous environment, the electromagnetic response of the gold-sphere could be treated efficiently via Mie-Theory [65]. Because of the presence of the glass-water interface we resort to numerical full-wave simulations. In an experiment, the source could be diffusing fluorophores in water, or a biological system where fluorescently marked proteins are diffusing or actively transported. The source shall not have any particular orientation, either because the rotational diffusion time is faster than the fluorescent decay time [91], or because the

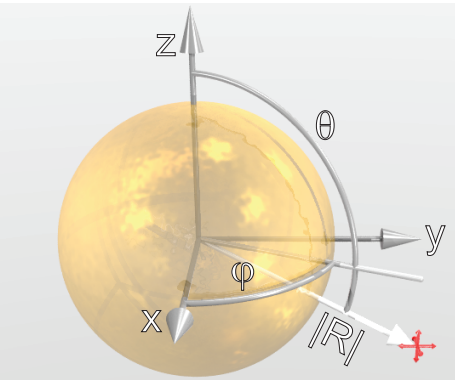

Figure 4.1: 3D sketch of a ø100 nm gold colloid and the used coordinate system. The glass interface (not shown) is touching the sphere at the top ($\theta = 0°$).

source consist of an ensemble of emitters immobilized with random orientation in a host material, e.g. as in the case of a dye-doped polystyrene bead. We then ask the question how the presence of the antenna changes the far-field properties of the fluorescence, i.e. fluorescence lifetime, polarization or back focal plane intensity distribution. In the absence of the antenna, the lifetime corresponds to the natural lifetime of the fluorophore, the emission is unpolarized and the radiation pattern is isotropic.

To answer the question of how far-field properties change with emitter position, we define a set of observables which are easily accessible in standard fluorescence microscopy. Then, we perform a numerical study in which we simulate our model system in 3D full-wave simulations and extract the desired observables from the simulations. We explain the details of the computation methods in the following section.

4.3 Methods

In figure 4.1 we show a schematic of the system and illustrate the coordinate system we use. The origin of the coordinate system coincides with the center of the gold colloid, which has a radius of $R_0 = 50$ nm.We denote the radial distance $|R|$, the azimuthal angle φ and the polar angle Θ. The colloid is touching the glass interface at $|R| = R_0; \theta = 0°$. For brevity in notation, we define the distance from the surface of the colloid as $R' = |R| - R_0$. We refer to the plane cutting the sphere midway, as the equatorial plane.

We use COMSOL 4.3b, a three dimensional numerical full wave simulation software [92], to calculate the electromagnetic response of the antenna to local driving, and from this obtain observables of a typical fluorescence experiment. The computation volume consists of a cylinder of water ($n = 1.33$) joined to a hemisphere of glass ($n = 1.52$) as shown in Fig. 4.2. The cylinder is $\approx 2\,\mu$m in diameter and $1\,\mu$m in height. The benefits of this choice are that it is compatible with perfectly matched layer boundary conditions in COMSOL and that the hemispherical halfspace has proven compatible with the calculation

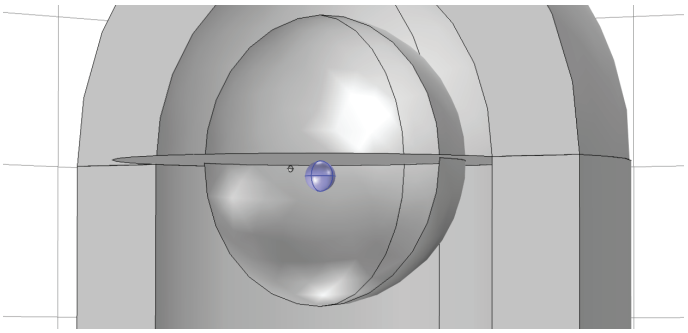

Figure 4.2: The geometry of the FEM simulation system. A ø100 nm gold sphere (blue sphere) is embedded in a transparent medium representing water $n = 1.33$ and touches the top halfspace representing glass ($n = 1.52$). Next to the colloid is a small virtual sphere (ø10 nm) which encloses our driving dipole and serves as monitor for the total radiated power. The entire system is surrounded by a bigger virtual sphere (ø$\approx 1\mu$m) on which the local fields are evaluated and then propagated to the far-field. The computation volume is terminated in all directions by perfectly matched layers (grey walls).

of the far-field differential emission patterns which we require on the glass side (as reported in Chapter 7). All the outer surfaces are terminated by perfectly matched layers. On the symmetry axis of the volume we have placed the gold sphere, touching the glass interface (blue sphere in Fig. 4.2). As optical properties of gold we interpolate tabulated data [67].

This chapter focuses on how far-field observables change as functions of the position of the local source. All simulations are performed in the frequency domain, at a frequency corresponding to $\lambda_0 = 660$ nm wavelength in vacuum. To obtain maps of the far-field observables as functions of local source position, we perform a sequence of simulations in which we sweep the position of the local driving point-dipole of constant current in increments of 50 nm along the x direction and 25 nm in z, each over a range of $0-400$ nm. This sampling appears coarse, but already requires ≈ 100 simulations of ≈ 1 hour each. We have verified, by performing additional simulations for select positions not on the grid, that interpolating between grid points gives a good estimate for the far field observables. Due to the rotational symmetry around the z-axis of our system, calculations in one plane are sufficient to retrieve the emitter-antenna interaction in the entire volume around the antenna. For each position we sample three dipole orientations, aligned with the x, y or z axis. One can rigorously show for all quantities reported in this chapter, that summing over the three orthogonal orientations is equivalent to averaging over all possible dipole orientations. We map four observables, namely:

- *Intensity*, the total power radiated into the detection optics on the glass side,
- *local density of photonic states enhancement (LDOSe)*, which quantifies the change in emission lifetime,
- *polarization*, the integrated intensity in two orthogonal polarization channels, and
- *radiation pattern*, the angular distribution of radiation on the glass side.

To obtain the local density of states, we determine the total power radiated by the dipole as measured by integrating the total power flux through the boundary of a virtual sphere (ø10 nm), enclosing only the dipole. To not violate the integrity of the virtual sphere

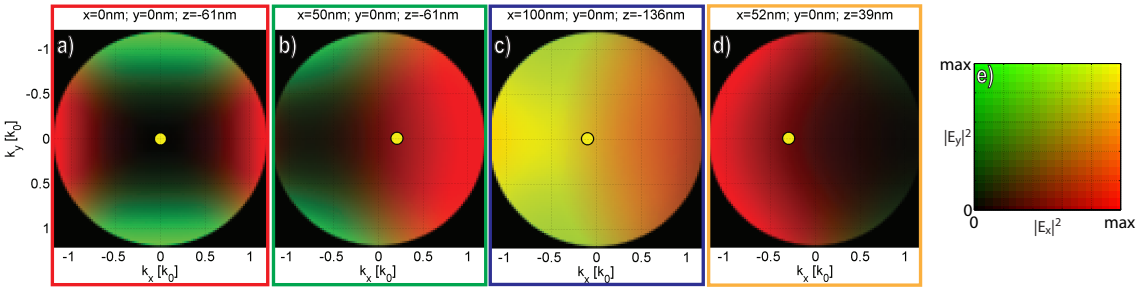

Figure 4.3: a-d) Polarization resolved intensity distribution in the BFP (radiation pattern) averaged over three source dipole orientations at different locations near the antenna. We show the axes in natural units of the free-space wave-vector $k_0 = \omega/c$. In following figures (4.5-4.8) we indicate the source position of the shown four BFP intensities by dots with the same color as the frames. Intensity of x (y) polarization is encoded in the red (green) color channel. e) Shows the colormap used for the plots.

surrounding the point-sources, the calculated source positions are at a minimal distance of 15 nm from the gold and glass interfaces. The total power that a fixed current dipole delivers to its environment is proportional to the local density of optical states [39].

To obtain the far-field collected by the detection optics on the glass side, we enclose the entire system in a ø≈ 1 μm virtual sphere and perform a Stratton Chu near- to far-field transformation [93]. We note that this transform is only approximate, since it incorrectly deals with the glass-water interface. However, benchmarks (reported in Chapter 7) have shown that it gives adequate results if the near-field sphere used for the transform is not chosen too close to the interface-plane. For each calculation we store the far-field radiation pattern with the full complex vectorial electric field.

We assume a collection numerical aperture of $NA = 1.2$ at the glass side, corresponding to a half-opening angle of $\theta_{\mathrm{max}} = 62°$. To derive our far-field observables, we use the complex electric field in the solid angles within our collection NA. The near- to far-field transformation provides the fields in spherical coordinates. However, in an experiment, the collection objective transforms the spherical wave-front into a cylindrical beam according to the Abbe sine condition for aplanatic lenses [39][Ch. 3], which we illustrate in Fig. 4.4. We numerically perform this transformation according to the formulation of Török et al. [94] to obtain a back focal plane (BFP) distribution of the electric fields, as one would obtain in an experiment. For all purposes, we sum up intensities in the BFP of the three orthogonal source dipole orientations for each position. We show four orientation-averaged BFP images in Fig. 4.3 corresponding to four different emitter locations. Each BFP image shows two intensities of orthogonal linear polarization color-coded in the red and green channel. The calculated source orientation-averaged BFP images are the basis to obtain the fractional radiative LDOS, the polarization, and the asymmetry of the BFP intensity distribution.

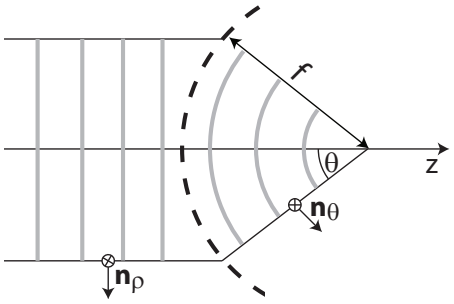

Figure 4.4: Schematic of the Abbe sine condition: the refraction of the light rays is determined by a spherical surface with radius equal to the focal length of the objective. This corresponds to a transformation from a spherical to a cylindrical coordinate system. The rotation of the polarization needs to be accounted for as indicated. Sketch is adapted from [39].

4.4 Intensity

While this chapter truly revolves around experimental observables that are *not related* to total detected intensity, plasmon antennas are usually judged in terms of the near-field enhancement they provide [71]. For a fluorophore located close to the antenna, the near-field enhancement translates into fluorescence enhancement due to the increased excitation rate [14]. For reference, we present the intensity characteristics of the antenna. We show the near-field of the antenna, when excited by a plane wave of normal incidence from the glass side in Fig. 4.5a. We observe an intensity enhancement of ≈ 50 close to the metal surface. Furthermore we show the increase of the radiated power (at fixed classical dipole current strength) into the assumed NA = 1.2 collection objective on the glass side in Fig. 4.5b. This corresponds to an orientation-averaged fractional radiative LDOS map by integrating the total power in the BFP. We find up to 4 times more intensity is radiated into the collection optics close to the nano-antenna.

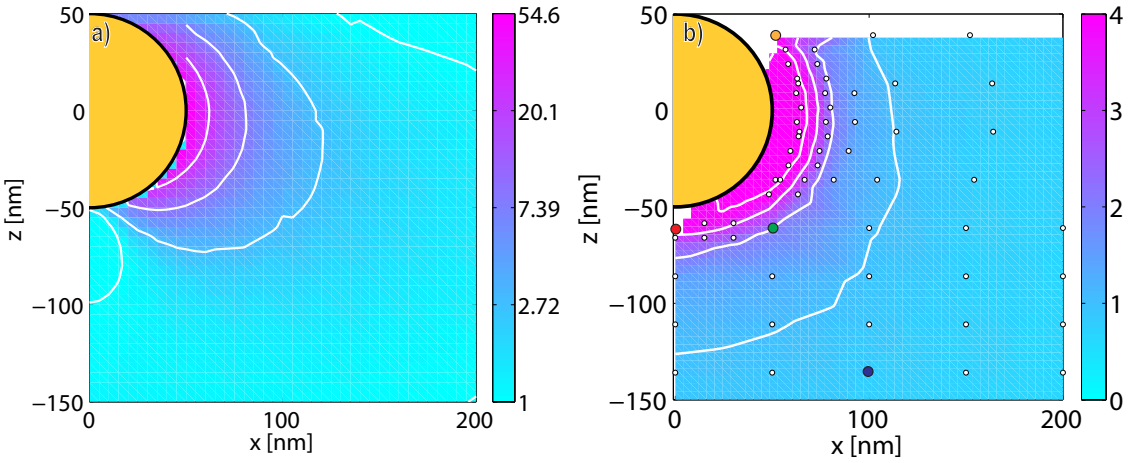

Figure 4.5: a) Intensity enhancement of an incident plane wave from the glass side around the nano-antenna. The lines of equal intensity correspond to 36%, 16% and 5% of the maximum value of 51. The driving field from the glass side has an amplitude of $1V/m$ and is polarized in the x direction. b) Map of the fractional radiative LDOS picked up by an NA = 1.2 objective at the glass side, also averaged over source orientations. The dots colored in red, green, blue and orange indicate computation points of which we show the BFP image in Fig. 4.3a-d. The areas in the color plots between the metal surface and the first computation points have values obtained from interpolation, and do not necessarily represent physical values accurately. The values in those areas should be disregarded.

4.5 Lifetime

Now we turn to experimental observables other than total detected intensity. Apart from localizing fields in small volumes, metallic nano-structures can modify the decay dynamics of photon sources in their vicinity. Fluorescence decay happens on a characteristic timescale, the fluorescence lifetime, which for organic fluorescent molecules is typically in the range of a few nanoseconds. This change in emission characteristics is described

by the photonic local density of states (LDOS), which is locally modified by the nano-antenna [14, 95, 96]. The LDOS can be deduced from a classical calculation, as it also describes the total emitted power from a classical fixed current source [97]. Therefore, we map the total radiated power, which we obtain by integrating the total power flux through a small virtual sphere surrounding the emitter. We average the radiated power over the three source dipole orientations. The total radiated power is proportional to the photonic local density of states [39]. Dividing by a reference value, obtained sufficiently far from the nano-antenna, gives us the LDOS enhancement at each position. For an emitter with unity quantum efficiency, this translates into a lifetime reduction by a factor of the LDOS enhancement, which can be measured by normal fluorescent lifetime measurements. We find that the radiative decay rate essentially only depends on the distance to the metal surface R', and contains no information about azimuth or polar angle. The radiative decay rate increases 10× over a distance of 50 nm.

To estimate the feasibility of fast position measurement on the basis of the lifetime, we consider a typical time-correlated single photon counting (TCSPC) experiment. A repetition rate of the pulsed excitation laser of 80 MHz allows the measurement of a few hundred fluorescence photons in 1 ms. Based on ref. [98] we estimate that this photon count allows an accuracy in fitted lifetime of 10% or better. This translates into a distance measurement with an accuracy of $\Delta R' = (\delta R')/(\delta \mathrm{LDOS}) \cdot \Delta \mathrm{LDOS} = 5$ nm. When considering an FCS experiment with a randomly diffusing source, it would require a viscous host medium to slow down diffusion sufficiently to trace lifetime fluctuations. Chapter 5 is devoted to the subject of diffusing sources close to a nano-photonic environment.

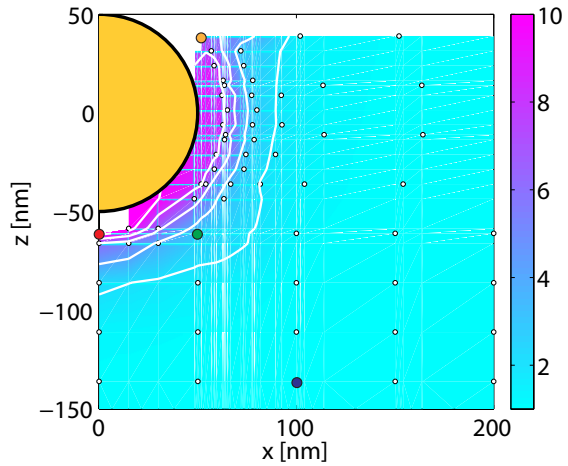

Figure 4.6: Map of the orientation averaged LDOS enhancement. White dots indicate the computation grid on which the emitter has been placed. The colorplot is an interpolation of the values calculated at the computation points. Areas of the plot between the metal surface and the first computation point does not contain physically accurate data. The dots colored on red, green, blue and orange indicate computation points of which we show the BFP image in fig. 4.3.

4.6 Polarization

Now we turn to the polarization characteristics of the collected far-field emission. The basis of the analysis are the source-orientation averaged polarization-resolved BFP intensities shown in Fig. 4.3. We now have a closer look at the polarization content of the four examples shown. We plot x and y polarized intensities in two different color channels, x intensity in red and y intensity in green. The colors lying on a straight line from black to yellow in the colormap in fig. 4.3e correspond to equal intensities in x-y polarization. We now investigate how, in a measurement scheme of only two detectors sensitive to orthogonal polarizations along x and y, yet integrating over the entire BFP, one can deduce information on the source position. Experimentally this measurement can easily be implemented with two intensity detectors placed after a polarizing beam splitter. Out of the two intensities measurements we derive the linear polarization contrast (LPC) which we define as LPC = $\left(I_x - I_y\right) / \left(I_x + I_y\right)$. We show the spatial dependence of the LPC in Fig. 4.7. We find that the strongest effect is close to the interface in the equatorial plane, reaching a LPC of more than 0.95. Due to the rotation symmetry of our system, the emitted photons are polarized along the radial vector projected on the x-y plane. This corresponds to a polarization along φ in the coordinate system as we have drawn in Fig. 4.1. The LPC-map in the equatorial plane is shown in fig. 4.7b. If the source is located at an angle of $\varphi = 0°\,(90°)$ in the equatorial plane and $R' \approx 20$nm the LPC reaches almost $1, (-1)$. If it is positioned at $\varphi = \pm 45°$ at the same distance, the LPC becomes zero, this is because even though the fluorescence is still highly polarized, it gives equal intensities in both detectors. Figure 4.7b shows that the polarization contrast does not uniquely map all azimuth angles. Naturally, we expect a degeneracy in the polarization contrast upon inversion at the origin - the polarization is x-polarized if the fluorophore is on the x-axis next to the colloid, no matter if it is left or right of the colloid. Additionally, the use of only two detectors results in two mirror planes along the axis, so only angles between $0° - 90°$ can be retrieved, but the quadrant in which the source is located can not be identified. We will find, in Section 4.7, that the analysis of the radiation pattern lifts this degeneracy. In a typical fluorescence experiment, in a time frame of 1 ms, we can expect to collect 500 counts. Distributing them equally over the two detectors and assuming poissoinian statistics, results in a relative error in the photon counts of $\frac{\sqrt{250}}{250} \approx 6\%$ in each detector. We can propagate the error to find

$$\Delta LPC = 2\sqrt{\frac{I_1 I_2}{(I_1 + I_2)^3}}$$

which results, for $I_1 = I_2 = 250$, in $\Delta LPC = 1/\sqrt{2I} = 0.04$. This corresponds to an error in angle of $\Delta\phi = (90°/2) \cdot 0.04 = 1.8°$. For an emitter in the equatorial plane, 10 nm away from the metal surface this translates into an error position along the equator of 2 nm.

The polarization analysis could be further improved by adding detectors at $\pm 45°$ or even mapping the full Stokes vector [22] with six detectors, including both circular polarizations. Measuring the full Stokes vector would allow to retrieve the total degree of polarization, the eccentricity of the polarization ellipse, as well as the orientation of the long and short axis and their relative phase. Retrieval of the long axis of the polarization ellipse directly reduces the degeneracy of a measurement of the azimuth angle from four quadrants to

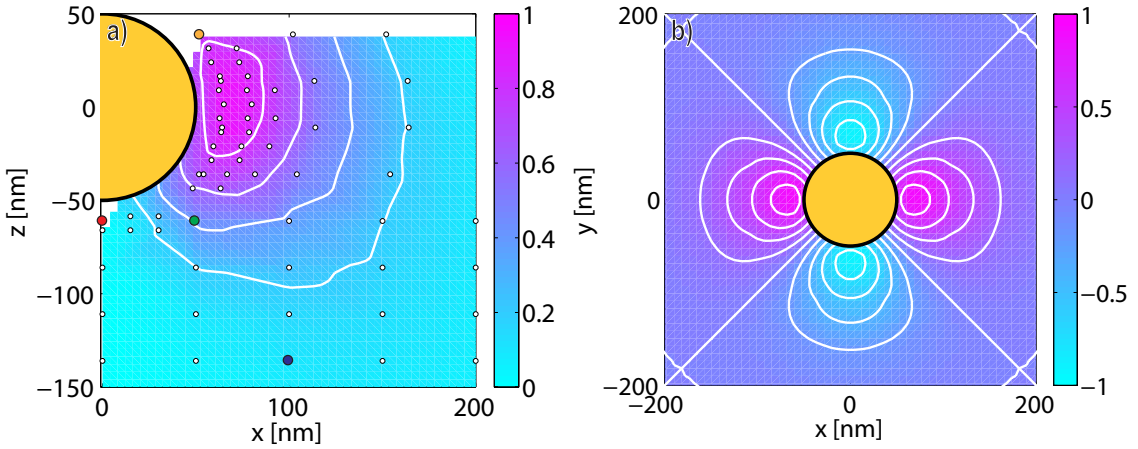

Figure 4.7: Spatial dependence of the linear polarization contrast, induced on an isotropic emitter by a spherical nano-antenna. a) colorcoded on the XY-plane of the emitter position. b) linear polarization contrast plotted for emitter positions in the x-y (equatorial) plane of the system. This plot has been calculated form the calculation in the x-z plane and invoking rotation symmetry of the system.

two quadrants. Measuring the total degree of polarization would also provide a distance measurement, which is easier to implement than a lifetime measurement.

4.7 Radiation pattern

We have seen that fluorescence lifetime and polarization are strongly modified by the nano-antenna. Now we assess how the *radiation pattern* changes with emitter position [99–102]. Therefore we calculate the center of gravity $\langle \mathbf{D} \rangle$ of the BFP intensity

$$\langle D \rangle_i = \frac{\iint \left[I(k_x, k_y) \cdot k_i \right] \mathrm{d}k_x \mathrm{d}k_y}{\iint \left[I(k_x, k_y) \right] \mathrm{d}k_x \mathrm{d}k_y},$$

with $i = x, y$, summing over the total intensity $I = |E_x|^2 + |E_y|^2$. Experimentally, this measurement could be implemented by placing a quadrant photo diode in the back focal plane. The advantage of a quadrant photo-diode over a CCD is that the signal is not diluted over many, but just 4 pixels, and quadrant photo diodes allow fast acquisition (tens of kHz).

We again have a look at the four selected BFP images shown in Fig. 4.3, now looking at the intensity distribution instead of the polarization. In each of the BFP maps, the center of gravity is indicated by a yellow circle. The center of gravity in the BFP evidences a large displacement for some source positions. When the emitter is placed 10 nm below the colloid on the symmetry axis of the system (Fig. 4.3a), we find high intensities at large collection angles and zero intensity at the center position, as we would expect for a z-oriented dipole. Displacing the emitter 50 nm along x, off the symmetry axis (Fig. 4.3b) causes the BFP intensity distribution to lose its rotational symmetry. In fact, we now observe a strong asymmetry in the intensity distribution, with a displacement of the center of gravity of $0.2k_0$ into the x-direction, with k_0 denoting the wave-vector in vacuum ($k_0 = \omega/c$). Even at larger distances, when placing the emitter at $[x, y, z] = [100, 0, -136]$ nm

(Fig. 4.3c) the effect of the antenna on the fluorescence emission pattern is not negligible, and we find a structured and asymmetric intensity distribution with a displacement of its center of $0.07k_0$. The strongest effect appears when the emitter is in between the gold surface and the glass (Fig. 4.3d). This configuration results in a displacement of the center of gravity of $0.25k_0$ in the BFP.

Having calculated $\langle\vec{D}\rangle$ for each emitter position, we express the displacement vector in polar coordinates with the total distance from the origin $|\langle D\rangle| = \sqrt{\langle D\rangle_x^2 + \langle D\rangle_y^2}$, and the angle $\theta_{\langle D\rangle} = \arctan\left[\langle D\rangle_y / \langle D\rangle_x\right]$. Figure 4.8 shows the extracted BFP parameters in a color-coded spatial map of the emitter position, as we did previously for the linear polarization contrast.

The cross-cut at $y = 0$ (fig. 4.8a) shows a non-trivial spatial distribution of the asymmetry parameter, with two regions of strong BFP asymmetry close to the antenna surface. For our computation points in the XZ-plane, the BFP center only moves on the x axis. The white arrows originating at each computation point indicate in which direction the BFP image is shifting. As expected, the BFP asymmetry is zero on the symmetry axis of the system, meaning directly below the colloid at $\theta = 180°$. With decreasing polar angle, but keeping the distance to the gold surface around 20 nm, the BFP asymmetry peaks around $\theta \approx 135°$, further approaching the glass surface, the asymmetry decreases again and vanishes around $\phi \approx 100°$. Even closer to the glass surface, the asymmetry in the BFP increases again and reaches its maximum of $0.25k_0$, with a shift into the opposite direction to the case in fig. 4.3b.

The colormap in the equatorial plane (fig. 4.8b) shows that in one plane the displacement of the BFP center lifts the degeneracy of azimuthal angle retrieval, which is inherent in the polarization-based measurement. Unfortunately, we find that the orientation of the BFP displacement changes not only in magnitude but also in sign with the polar angle, when the source crosses the equator.

This complex behavior can be explained by a simple picture which we illustrate in fig. 4.9. We have illustrated four different dipole orientations by arrows in different colors. To each dipole orientation corresponds a radiation pattern which is illustrated by two lobes of the same color as the dipole, with their maximum located orthogonal to the dipole axis. The black dashed line indicates the collection angle of the objective. The small graph in the top illustrates the intensity distribution in the BFP. The induced dipole moment in the antenna will be mainly aligned along the connection vector of the emitter to the colloid. If the emitter is located below the sphere, the dipole moment lies along the z-axis. Thus, the radiation pattern is a doughnut-shape with maximum intensity in the XY plane (red). If we position the emitter at a polar angle of $\theta = 135°$, the induced dipole moment is tilted accordingly, as will the radiation pattern (green). Hence, only one lobe will be collected by the collection optics at the glass side, showing a strong asymmetry. Increasing the polar angle further to $\approx 90°$ would give, in a homogeneous environment an exclusive polarization in the x-direction (black). Then the radiation pattern collected on the glass side will have a lobe in the normal direction, again mirror symmetric along the x and y-axes, and thus the asymmetry parameter will be zero. Further increasing the angle of the emitter position further shifts the lobe to the other side of the radiation pattern and the asymmetry parameter again becomes finite (orange).

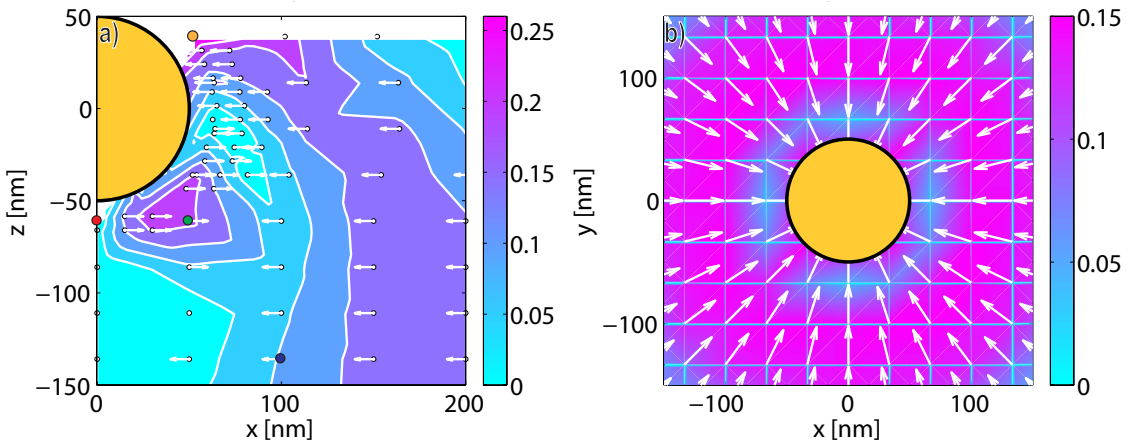

Figure 4.8: Displacement of the center of gravity of the BFP intensity in units of k_0. The colormap indicates the magnitude of the displacement, the white arrows indicate the direction of the displacement along the radial vector. a) XZ-plane and b) the calculated BFP displacement in the equatorial plane.

Figure 4.8b shows a crosscut at a constant height of $z = 0$ nm, in the equatorial plane of the colloid. The BFP evidences an asymmetry up to $0.1k_0$ in close proximity to the colloid. A plot in the XY-plane allows to visualize the direction of the BFP asymmetry, by plotting at each source position an arrow indicating $\phi_{\langle D \rangle}$. We find that the displacement is always oriented in the radial direction, which is expected due to the symmetry of our system.

We perform a similar error analysis for the center of gravity of the BFP intensity, as we did for the linear polarization contrast. We assume a quadrant photodiode to calculate the center of gravity in the BFP, which we calculate by $\Delta\langle D \rangle_x = (I_1 + I_2 - I_3 - I_4)/\Sigma I$ and

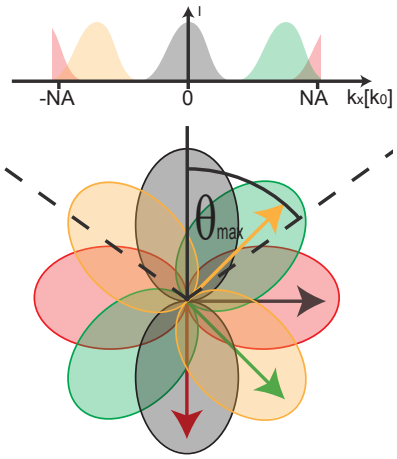

Figure 4.9: Bottom) illustration of four radiation patterns (lobes) in dependency of the dipole moment, sketched as arrows in the corresponding color. The black dashed line indicates the maximum collection angles. Top) schematic of the intensity distribution on the BFP. Only the green and orange lobes, corresponding to 90° and 135° dipole orientation show an asymmetric intensity distribution. The dipole with 0° and 90° show different but symmetric radiation patterns.

$\Delta\langle D\rangle_y = (I_1 - I_2 + I_3 - I_4)/\Sigma I$ with $\Sigma I = I_1 + I_2 + I_3 + I_4$. Assuming an error in each intensity measurement, we obtain an error on each axis of

$$\Delta\langle D\rangle_x = \frac{1}{\Sigma I}\sqrt{(1-\langle D\rangle_x)^2\left[(\Delta I_1)^2 + (\Delta I_2)^2\right] + (-1-\langle D\rangle_x)^2\left[(\Delta I_3)^2 + (\Delta I_4)^2\right]}$$

and

$$\Delta\langle D\rangle_y = \frac{1}{\Sigma I}\sqrt{\left(1-\langle D\rangle_y\right)^2\left[(\Delta I_1)^2 + (\Delta I_4)^2\right] + \left(-1-\langle D\rangle_y\right)^2\left[(\Delta I_2)^2 + (\Delta I_3)^2\right]}\,.$$

When the error is given by shot noise in each of the intensity measurements, and assuming an equal count-rate on each detector $I_i = I$ (corresponding to small BFP asymmetry), we obtain an absolute error of $\Delta\langle D\rangle_i = \frac{1}{2\sqrt{I}}$ in each dimension. A total photon budget of 500 distributed over four detector gives 125 photons per detector and an absolute error of $\Delta\langle D\rangle_{x,y} = 0.04$. This results in an error in the polar angle of $(90°/0.4)\cdot 0.04 = 9°$, which corresponds to a displacement of 9 nm at $R' = 10$ nm.

4.8 Summary and outlook

We have shown that with a photon budget of 500 counts for each axis, one can in principle localize a single emitter in all three dimensions in the vicinity of an antenna, with an accuracy of a few nanometers. We can obtain the radial distance R' via lifetime measurements with an accuracy of 5 nm. The azimuthal angle is accessible by the BFP asymmetry and polarization analysis, with an accuracy of 1°. The polar angle can be obtained with an accuracy of 9° via the total asymmetry of the BFP. The mapping of the considered observables is not unique, as there remains a degeneracy for inversion at the center of the gold colloid. For practical purposes this is not a severe problem when measuring trajectories if continuity of the trajectory is assumed, meaning that the displacement of the emitter is small compared to the antenna size for two successive localizations. If the antenna rests on a interface on which fluorophores are moving in a plane, the position reconstruction is unique.

Placing a gold nano particle close to or into a delicate biological system like a cell in order to localize fluorescent markers is invasive, and difficult to achieve in a controlled way. The proposed localization technique is thus not meant as an alternative to conventional super resolution imaging. Nevertheless, there are imaginable scenarios where the presence of a nano-particle is tolerable or even desired and the potentially high bandwidth of our method of emitter localization rates in the kHz regime is beneficial. Surface functionalization for selective protein binding has become a powerful tool to investigate protein function [103]. Gold surfaces are easy to handle in standard micro/nano-fabrication steps and have been used to locally bind specific proteins, e.g. to reconstitute basic elements of a cell and investigate its mechanics [104].

A potential experiment that could hugely benefit from our localization technique is in the field of protein or RNA/DNA folding [105, 106]. For instance, one end of a fluorescently labeled protein could be attached to the gold colloid, which would serve as the optical antenna allowing localization of the fluorescent label in a volume of 50 nm

around the antenna. If the protein were then triggered to fold or unfold, our measurement technique would allow to track the full position vector of the fluorescent label with a rate of approximately 1 kHz. This would allow to reconstruct the energy landscape of the RNA folding in real time with unprecedented accuracy, on length- and time-scales which are not accessible by SR microscopy or FRET.

5

Non-intensity fluctuations of emitters diffusing near nano-antennas

The motivation to use nano-antennas for fluorescence correlation spectroscopy is twofold. First, the field enhancement close to a nano-antenna can reduce the detection volume and thus allow FCS measurements at higher solute concentrations. Second, using fluorophores with known diffusion coefficients allows to measure the size of the detection volume. Thereby, FCS provides an experimentally simple and non-invasive method to characterize the size of the near-field of a nano-antenna. As we have shown in Chapter 3, the main limitation to deriving such information from intensity fluctuations is that, the signal originating from the excitation focus, that typically surrounds an antenna in a microscopy experiment, reduces the effect of the high intensity volume given by the hot-spot.

In the previous chapter we showed the spatial dependence of various far-field observables of an isotropic photon emitter in the vicinity of a nano-antenna. Here, we conversely assess what information can be obtained about a nano-antenna, especially its near-field volume, by monitoring fluctuations of the far-field observables when a fluorophore randomly walks through the near-field of the antenna. First, in section 5.1, we point out experimental complications imposed by the necessity to acquire sufficient photons to calculate the derived observable. Second, in section 5.2, we find how to extract meaningful quantities from correlating time-resolved measurements of the observable, assuming a freely diffusing source. The key question is whether non-intensity observables allow the measurement of the near-field volume of the nano-antenna without being affected by the background focus. In section 5.3, we show how time-gating the photon detectors can be used to enhance the contribution of the near-field to the correlation function, and furthermore eliminate the background signal completely, when multiplying with a filter function based on the lifetime histogram. Section 5.4 focuses on polarization fluctuations and shows that the characteristic timescales of these fluctuations are a robust quantity, which is not altered by the background signal.

5.1 Timescales of interest

Measurement of the observables derived in Chapter 4, i.e., fluorescence lifetime, linear polarization contrast and backfocal plane asymmetry requires the detection of multiple photons. In most microscope setups, fluorescence of a bright single emitter can reach count-rates of upto 1 MHz. Calculating the auto-correlation of temporal fluctuations of an observable requires that the time needed to measure the observable, to be shorter than the diffusion time. Further, the total measurement time should be much larger then the diffusion time, in order to average over a sufficient amount of diffusion events. Since uncorrelated noise does not add features to the correlation function, we relax our accuracy target compared to the previous chapter, and estimate that one requires only 100 counts for each derived observable. This sets a temporal resolution of 100 μs in which we can calculate the observable.

We assess different diffusive systems to probe the electromagnetic properties of an plasmonic antenna, which typically extend on a length scale of ≈ 50 nm. The average displacement of a particle in a purely diffusive system is given by $\Delta r = \sqrt{\langle |\mathbf{r} - \langle \mathbf{r} \rangle|^2 \rangle} = \sqrt{2 \cdot n \cdot D \cdot \Delta t}$; with the diffusion coefficient D in a bulk liquid ($n = 3$) or in a 2d interface ($n = 2$), as would be the case of fluorescently labeled molecules in a membrane. In fig.

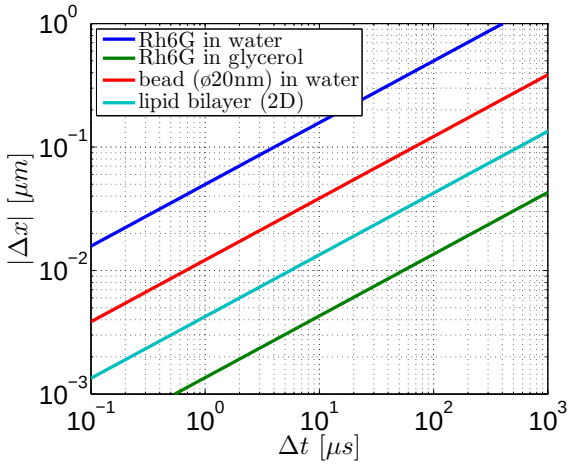

Figure 5.1: Mean distance an object displaces in a diffusive system after a given time: Rhodamine6G in water (blue, $D = 4.14 \cdot 10^{-6}\text{cm}^2\text{s}^{-1}$, [107]), Rh6G in glycerol (green, $D = 3.07 \cdot 10^{-9}\text{cm}^2\text{s}^{-1}$); ø= 20 nm bead in glycerol (red, $D = 1.8 \cdot 10^{-10}\text{cm}^2\text{s}^{-1}$, [38]) and 2D-diffusion of lipids in a bilayer (cyan, $D = 4.5 \cdot 10^{-8}\text{cm}^2\text{s}^{-1}$, [108]).

5.1 we show the mean displacement as a function of the time delay Δt for four different diffusive systems on a logarithmic scale. We then calculate the diffusion length for the 100 μs time-window. The organic dye molecule Rhodamine 6G (Rh6G) in water (blue line) moves ≈ 500 nm in 100 μs, which is too far to locally probe a near-field. A host liquid with higher viscosity reduces the diffusion coefficient. Assuming the same hydrodynamic radius for Rh6G as in water but now taking glycerol as a host liquid with higher viscosity (green) the diffusion length is ≈ 15 nm. Instead of increasing the viscosity, increasing the particle size also reduces the diffusion time. Fluorescent polystyrene tracer beads (ø20 nm) immersed in water (red, [38]), give a diffusion length of ≈ 100 nm. Dissolving the beads

in a liquid of higher viscosity would allow to again reduce the diffusion length by up to 2 orders of magnitude. Alternatively, we can use a two-dimensional system such as a lipid bilayer (cyan) which has a diffusion length of ≈ 40 nm in $\Delta T = 100\mu$s.

The gradient in the electromagnetic properties of the nano-antenna calculated in the previous chapter have characteristic length scales in the order of ≈ 50 nm. This sets an upper limit for the diffusion coefficient of the emitter which can be used to probe temporal fluctuations of the far-field observables, given a 10 kHz sampling rate. We identify as viable diffusive systems to perform this experiment: 1) organic dyes in a highly viscous host as glycerol, 2) ø20 nm tracer beads in a host medium more viscous than water, or 3) supported lipid bilayers. All calculations in this chapter assume a diffusion coefficient of $D = 1 \cdot 10^{-9}\mathrm{cm}^2\mathrm{s}^{-1}$, which corresponds approximately to Rh6G in glycerol at a concentration of $\langle C \rangle = 1 \cdot 10^{12}\mathrm{cm}^{-3}$.

5.2 Auto-correlation of fluctuating observables

In standard intensity FCS essentially two parameters of the sample can be retrieved from the auto-correlation, if the diffusion coefficient D is known. First, the detection volume can be retrieved by the roll-off time of the auto-correlation. Second, the correlation contrast $G(0) - 1$, which is inversely proportional to the average number of emitters $\langle N \rangle$ in the detection volume. This inverse proportionality is guaranteed by the linear scaling of the observable, in this case intensity, with emitter number [10, 34]. None of the quantities derived in chapter 4 (emission decay rate, polarization contrast and back focal plane asymmetry) are linear superposition of the single particle quantity. Hence, the correlation contrast calculated from the fluctuations of those observables does not allow to deduce the number of particles which contribute to the signal, as it is done in intensity FCS [10].

To be able to use common FCS theory, we proceed by turning changes in fluorescence lifetime into an intensity-contrast, and then employing standard FCS post-processing. Alternatively, in the case of polarization, we construct the auto-correlation of the polarization contrast $\Delta I = I_x - I_y$ via the auto- and cross-correlations of the intensities in two polarization channels. This also allows us to use the established tool set from standard FCS.

5.3 Lifetime fluctuations due to varying LDOS

In this section we consider a time-resolved lifetime measurement and present two ways to turn a change in lifetime into an intensity contrast. The molecular detection function, as introduced in Chapter 2 section 2.1.3, thus gains an additional, spatially dependent, function $W[\tau(\mathbf{r})]$, which weights the intensity dependence on the decay-time. The decay time at position $\mathbf{r}$ is given by $\tau(\mathbf{r}) = \tau_0 / LDOSe(\mathbf{r})$, with the intrinsic decay time τ_0 and the local density of states enhancement $LDOSe$. The molecular detection function (MDF) then reads

$$\mathrm{MDF}(\mathbf{r}) = \mathrm{EEF}(\mathbf{r})\, \eta(\mathbf{r})\, \mathrm{CEF}(\mathbf{r})\, \mathrm{W}(\tau(\mathbf{r}))$$

as a function of the excitation efficiency function (EEF), the quantum efficiency η and the collection efficiency function (CEF), as introduced in Chapter 2. We will propose two different weighting functions which turn a lifetime change into a intensity change, that are compatible with standard equipment used for determining fluorescence lifetime.

In a fluorescence lifetime microscope, one typically uses a pulsed excitation laser such that less than 1% of the pulses results in a detected photon. A decay trace is obtained as a histogram of arrival times, requiring that one acquires the precise time of arrival of each photon relative to the preceding excitation laser pulse. Technically, the measurement is realized by acquiring both the absolute arrival time of an electronic pulse synchronized with the laser, and the arrival time of the electronic pulse provided by the fluorescence detector, which is typically an avalanche photodiode with sub-100 ps resolution. The same hardware applies to FCS experiments. For a typical FCS experiment one uses a continuous wave laser, and only the arrival times of photons are stored, and afterwards correlated in software. For a technical description we refer the reader to ref. [109].

5.3.1 Turning a lifetime reduction into an intensity enhancement via detector gating

We can make our detector become selective to emitters that show a shortened lifetime, due to an enhancement in the local density of states (LDOS), by gating the detector in such a way that only photons up to a time delay of τ_F after the excitation pulse are recorded. The gating of the detector corresponds to a filter function $F(\tau, \tau_F) = 1 - \Theta(\tau - \tau_F)$, where Θ is the Heaviside function and τ_F the time after the excitation at which the detector is switched off (see red solid line fig. 5.2a). Assuming a fluorescence species with a time decay dynamics $I(\tau) = [I_0/\tau_0]\exp(-\tau/\tau_0)$, this gating scheme converts time-dependence into a lifetime dependent intensity

$$I_G = \int_0^{\tau_F} I(\tau)\, d\tau = I_0[1 - \exp(-\tau_F/\tau_0)].$$

Clearly, one must optimize the delay τ_F such that on the one hand it is long enough that one does not lose too much signal, while on the other hand it is short enough to have good selectivity to changes in the LDOS. Taking as gating time $\tau_F = \ln(2)\tau_0$, a reasonable compromise is obtained, since for the unperturbed emitters the penalty in intensity is 50%. In other words, given the intrinsic lifetime τ_0, half the photons are discarded by the proposed gating scheme. Now turning to LDOS enhancement effects, for the chosen gating time, the gating converts the spatially dependent LDOS enhancement ($LDOSe$) into a weighting function

$$W_G(LDOSe) = 1 - 2^{-LDOSe}.$$

This weighting is shown as the red solid line in fig. 5.2b. This function approaches 1 for large LDOS enhancement, meaning that all the photons are included in the MDF for high-LDOS regions, while for regions of no LDOS enhancement 50% of the photons are discarded. The benefits of this gating technique are the following: First, since a lifetime change is converted to intensity, the observable to be correlated remains proportional to solute concentration. Thereby, the correlation contrast is still a concentration measure.

Second, this gating scheme is easily implemented in hardware. However, it can also be easily included in the postprocessing software. A disadvantage of this gating technique is that the weighting function does not tail off to 0, but only goes from 1 to 0.5. Hence, it does not strongly limit the MDF in space. By tuning the gating time, stronger selectivity to high-LDOS regions can be obtained, but only at the price of a drop in signal.

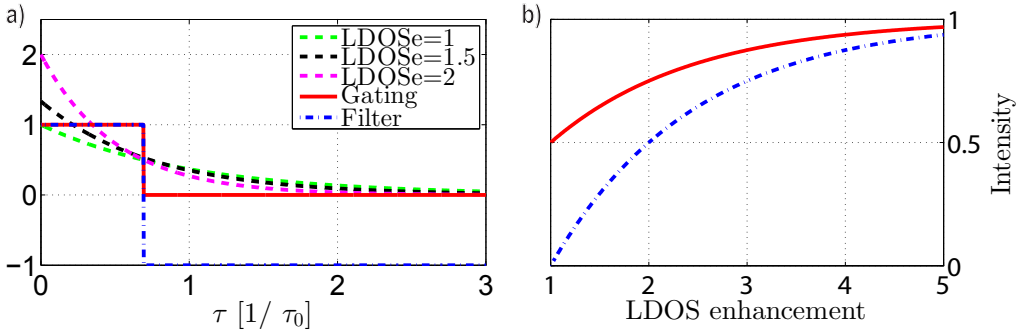

Figure 5.2: a) We show three single exponential decays: with the lifetime τ_0 (green dashed line), with a lifetime reduced by a factor of 1.5 (black dashed line) and a lifetime reduced by a factor of 2 (magenta dashed line). The red solid line illustrates the effect of gating the detector, such that it becomes insensitive after a time τ_F. For $\tau_F = ln(2)\tau_0$, half of the intensity of the green line is not detected. The dashed blue line illustrates a different filtering, where counts arriving after τ_F are multiplied by -1, hence the integral of the single exponential of natural lifetime multiplied with the filter function integrates to zero. Faster decays show a positive integral. b) Effect of detector gating (red solid line) and histogram filtering (blue dashed line) on the measured counts, as functions of lifetime reduction.

5.3.2 Background field suppression by lifetime histogram filtering

The concept of detector gating can be extended to a more complex, but linear operation on the lifetime histogram. We show such filter-function in fig. 5.2a as the blue dashed line. This filter function multiplies counts arriving after τ_F with a weight of -1. This yields a signal $I_F = \int_0^{\tau_F} I(\tau)d\tau - \int_{\tau_F}^{\infty} I(\tau)d\tau$. When choosing for τ_F the half-time of the natural decay, $\ln(2)\tau_0$, we can calculate the filtered intensity as a function of the LDOS enhancement ($LDOSe$) and obtain the filtered intensity $W_F = 1 - 2^{1-LDOSe}$ (fig. 5.2b, blue dashed line). This weighting of the lifetime histogram completely suppresses the fluorescence signal originating from decays at the natural lifetime τ_0 completely, and singles out the region of high local density of states enhancement in the MDF. Thereby, it can be viewed as an additional, effective background suppression, suppressing in particular contributions from the background focus where the nano-antenna does not enhance the LDOS. Figure 5.3a shows the spatial dependence of the weighting function $W_F(\mathbf{r})$. We obtain the filter-map from the LDOS enhancement map calculated in Chapter 4 (fig. 4.6). The weight function W_G of the simpler gated detection scheme discussed in section 5.3.1 has the same spatial distribution, but only reaches 50% suppression.

To illustrate the effect of the background suppression by time gating, we calculate the auto-correlation function (ACF), modeling a FCS experiment done with 50%, 100% and without background suppression, with an approximated gaussian model. To set up this

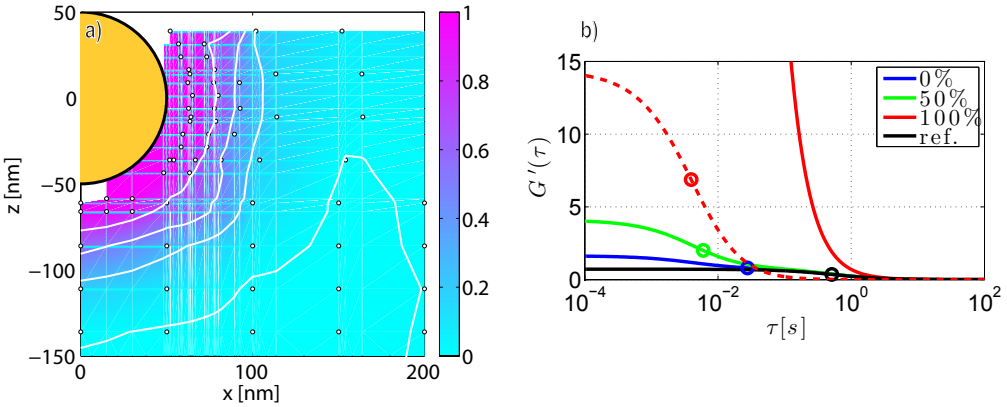

Figure 5.3: a) The weight function W_F obtained by lifetime filtering tuned to the natural lifetime of the fluorophore. Time gating of detectors can suppress intensity originating from fluorophores that experience no LDOS enhancement. This filter function hence serves to strongly localize the overall MDF, obtained by multiplying with the usual intensity-FCS MDF, to regions of highly enhanced LDOS. b) Simulated FCS curves calculated for a gaussian approximation to the MDF given by the excitation field, the near-field enhancement and the weight function. The excitation field is approximated by a Gaussian of 500 nm with and 1 μm length, the near-field enhancement by a gaussian hot-spot of width 50 nm in all three dimensions. The background gaussian has a peak intensity of 1, the hot-spot of 50. The effect of the weighting function is modeled as an additional scalar weighting of the background focus with: 1 for the case with no background suppression (blue), 0.5 (green) for the suppression as provided by detector gating, and 0 for full suppression of the background focus (red solid line, dashed line scaled by 1/100), as provided by the histogram filtering. As reference, the black line shows the ACF of the background focus without a hotspot.

approximated gaussian model, we first determine the MDF from simulation, taking it as the product of a flat collection efficiency function (CEF) (corresponding to a detection with flat spatial filtering), assuming unit molecular quantum efficiency, and taking as excitation efficiency the near field pump field distribution created by the excitation focus and the field enhancement near the antenna. For the calculation we employ the model developed in chapter 3. We construct the MDF with two Gaussians, an elongated background focus of width 500 nm and 1 μm length, and a hot-spot of width 50 nm in all three dimensions. The background Gaussian has a peak intensity of 1, the hot-spot of 50 as we have found for the near-field enhancement in the full wave simulation shown in fig. 4.5. In fig. 5.3b we show the calculated auto-correlation functions by scaling the intensity of the background focus by 1, 0.5 and 0, corresponding to the case of no time gating, i.e., no background suppression on basis of LDOS (blue line), 50% suppression (green), as provided by the detector gating, and complete suppression (red) as provided by the histogram filtering. As a reference we show the autocorrelation function of the assumed Gaussian background focus in absence of the plasmon antenna (black line). The background focus shows a correlation contrast of 0.8 and a roll of time of 511 ms. With the known diffusion coefficient D, we can relate the roll-off time τ_0 to a characteristic length of $\Delta x = \sqrt{6\,D\,\tau_0}$. For the background we obtain a characteristic length of $\Delta x_{BG} = 550$ nm, which is compatible with the elongated gaussian. In the presence of the nanoantenna, we find that in the case calculated with the full intensity of the background focus, the ACF shows two roll-

offs, corresponding to the volume of the background and the hot-spot, respectively. The correlation contrast is 1.6 and we find a roll-off time of 28 ms which corresponds to a characteristic length of $\Delta x_{100\%} = 130$ nm. Suppressing the background by 50%, increases the correlation contrast 2.5 times to 4.0, and reduces the roll-off time to 6.0 ms, yielding a $\Delta x_G = 60$ nm. Complete elimination of the background yields a correlation contrast of ≈ 1400 and shortens the correlation time to 4.0 ms, which corresponds to a characteristic length of $\Delta x_F = 49$ nm, in good agreement with the dimensions of the spherical gaussian we have assumed for the calculations. In our model we retrieve the effective volume of the gaussian hotspot as $V^* = [\sqrt{\pi}50 \text{ nm}]^3 \approx 7 \cdot 10^{-4} \mu\text{m}^3$. In an experiment, the correlation time retrieved by suppressing the background signal through lifetime filtering, corresponds to the characteristic volume in which the LDOS is modified by the nano-antenna.

5.4 Polarization fluctuations of a diffusing, isotropic source near a gold colloid

We now turn to polarization as the second non-intensity observable that we analyze in this chapter. The linear polarization contrast (LPC), introduced in section 4.6, is not linear in emitter number due to the normalization by the total intensity $I_x + I_y$. Instead if the normalization is omitted and a contrast $\Delta I = I_y - I_y$ defined, then its auto-correlation can be constructed from the normalized auto and cross-correlations of the fluctuations of the two polarization channels.

In this section we assess the feasibility of FCS on the basis of polarization contrast at a nano-antenna. To do so, we build an approximate replication of the simulated MDF using a superposition of Gaussians. Thereby we construct two polarized MDFs in subsection 5.4.1. We calculate the auto- and cross-correlation of both X and Y polarized intensities, assuming free 3D diffusion, and then construct the correlation of the non-normalized polarization contrast $\Delta I = I_x - I_y$ from the auto- and cross-correlations.

5.4.1 Constructing the MDF for x- and y- polarization

As shown in section 4.6 of the previous chapter, in close proximity to the nano-particle, the fluorescence emission is highly polarized. For each polarization, the MDF is expected to show two lobes on either side of the particle. To model this, we start with a prolate gaussian that encompasses both lobes with a width of 100 nm and a radius of 50 nm, comparable to the particle. To turn this elongated MDF into a two-lobe MDF, we need to essentially remove the central particle. To this end, we subtract a gaussian of width 50 nm in each dimension. We neglect the modification of the diffusion kernel by the impenetrable boundaries of the gold colloid. First we examine FCS in the absence of a background focus, while in section 5.4.2 a background focus is added.

In fig. 5.4c we show the various correlation functions which we can obtain and construct from two intensity measurements. We calculate both the auto-correlation functions (ACF), corresponding to an FCS experiment with each of the detection functions (blue), and the two cross-correlation functions (CCF, green), which correspond to a dual-focus FCS experiment with two MDFs. Because both MDFs are identical in shape but just differently oriented,

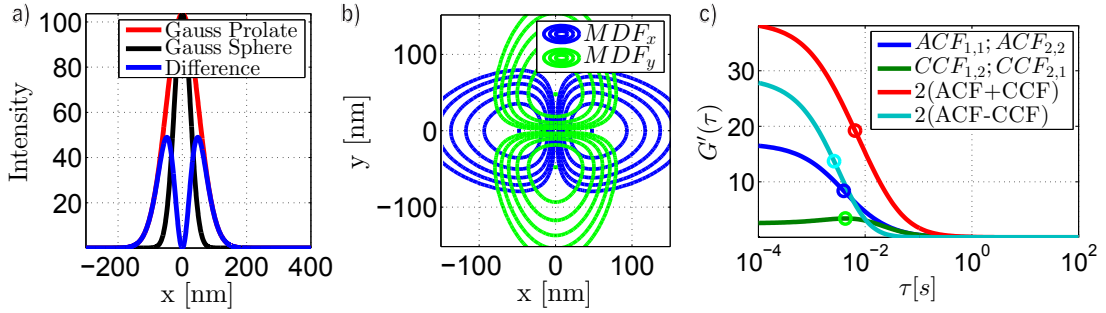

Figure 5.4: Construction of the MDF for one polarization channel; a) cross-cut through the MDF_x along the x-axis ($y = z = 0$). Shown are the elongated gaussian (red), the spherical gaussian (black) which are subtracted to construct the final MDF (blue). We then get a double peak with zero intensity at the center. The peaks are located at $\approx \pm 50$ nm. b) Crosscut of the two MDFs (blue, x-polarized, green y-polarized) through z=0. The contour lines are at values [37, 14, 5.0, 1.8, 0.67]% of the maximum of each MDF (from inside to outside). c) Auto-correlation of ΔI (cyan), constructed by the ACFs and CCFs of the X and Y polarization detector channels. The characteristic times (indicated as circles) are: CCF (peak): 4.2 ms; ACF(50%): 4.0 ms; ACF+CCF (50%): 6.4 ms; ACF-CCF (50%): 2.6 ms.

they have identical ACFs, and show a roll-off time of $\tau^*_{ACF} = 4.0$ ms. This corresponds to a mean diffusion length of $\Delta x_{ACF} = \sqrt{6\,D\,\tau^*_{ACF}} = 49$ nm. The CCFs are always identical, independent of the two MDFs. From these we can construct the correlation function of the sum of both detectors (red). The correlation function, corresponding to an FCS experiment of the combined MDFs, is given by $ACF(I_x + I_y) = ACF(I_x) + ACF(I_y) + 2CCF(I_x, I_y)$,. This ACF shows the longest roll-off time $\tau^*_{sum} = 6.4$ ms, as expected, because it represents the biggest volume. The auto-correlation of the polarization difference

$$ACF(\Delta I) = \int \left[I_x(t) - I_y(t)\right]\left[I_x(t+\tau) - I_y(t+\tau)\right] dt$$

can thus be constructed as

$$ACF(\Delta I) = ACF(I_x) + ACF(I_y) - 2CCF.$$

This quantity is plotted in Figure 5.4 (cyan curve), from which we find a roll-off time of $\tau^*_{\Delta I} = 2.6$ ms, corresponding to a diffusion length of $\Delta x_{\Delta I} = 39$ nm. The auto-correlation of the polarized contrast ΔI corresponds to a detection volume half the size of the single channel ACF.

Having a closer look at the CCF, we find a peak at $\tau^*_{CCF} = 4.2$ ms. As known in two focus FCS [82] and discussed in section 2.2.2.1, the peak time of the cross-correlation function is mostly determined by the distance R_0 between the peaks of the two MDFs. We can obtain the effective distance R_0 between the two MDFs employing Eq. (2.6) from chapter 2, which yields

$$R_0 = \sqrt{6\,D\,\tau^*_{CCF} + \frac{3}{2}\Delta x_{ACF}} = 78 \text{ nm}$$

which agrees well with the actual peak distance between the two MDFs of $\sqrt{2} \cdot 50$ nm = 71 nm. In chapter 6, we will focus on an optimized antenna geometry which provides a

calibrated distance reference for two different molecular detection functions based on this principle.

5.4.2 Two polarization MDFs with background signal

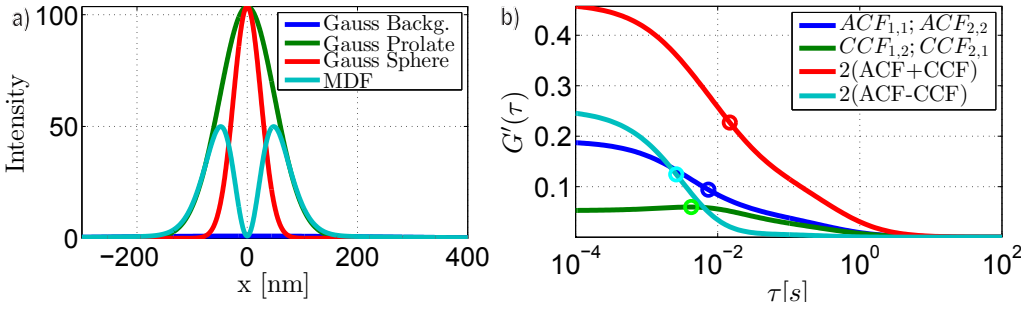

Figure 5.5: a) Construction of the MDF for one polarization channel with background focus of 500 nm width, 1 μm length and a peak intensity of 1. The near-field volume thus corresponds to an intensity enhancement of 50×. b) Auto-correlation of ΔI, constructed by the ACFs and CCFs of the detection channels. The roll-off times are: CCF (peak): 4.2 ms; ACF (50%): 7.4 ms; Sum (50%): 15 ms; ACF-CCF (50%): 2.6 ms.

In section 5.4.1 we assumed two strongly localized MDFs for both polarizations, with no background. However, a background focus will result in a strong, unpolarized, background intensity in both detectors. To assess how much this suppresses the correlation we modify both MDFs and add to each detection channel a broad background Gaussian. A prolate gaussian of 500 nm width, 1 μm length and a peak intensity 50× smaller than the peak of the twin-hotspots is added to both MDFs (cross-cut is shown in fig. 5.5a). Figure 5.5b shows the resulting ACFs and CCFs in the presence of the background. As the correlation functions are normalized by the total intensity, we observe a reduction in the correlation contrast by a factor of ≈ 100, resulting from the large increase of the effective detection volume by the background Gaussian. Apart from the reduction in magnitude, also the shapes of the correlation functions change. The peak of the CCF remains at 4.2 ms, but is less pronounced in the presence of the background. The roll-off time of the ACF (7.2 ms) is approximately twice that without the background focus. In contrast, the roll-off time of the auto-correlation of the polarization contrast ΔI, calculated as $2\,[ACF(\tau) - CCF(\tau)]$, stays the same at 2.6 ms. Hence, even in the presence of a common background focus in both molecular detection functions, we retrieve the same characteristic length scale. The correlation function of the polarization contrast ΔI thus allows the measurement of polarization fluctuations induced by the near-field of a nano-antenna, as it eliminates background contributions which are common to both detection channels.

5.5 Conclusion

We have shown for two non-intensity observables how we can obtain near-field dimensions by the analysis of far-field fluctuations in lifetime and polarization. First, we have shown

how to use changes in fluorescence lifetime, in combination with detector gating or histogram filtering, to make the detectors more (or exclusively) sensitive to fluorescence of faster decay in the near-field of the antenna. This gating technique can be easily implemented in an electronic fashion and thus does not require any post-processing of the data, other than that needed for standard correlation. Applying a more complex filter function can be done with software post-processing, and allows to completely suppress the signal originating from the unaltered fluorescence of natural lifetime. Thereby, lifetime filtering is a technique which can make an FCS experiment selective to the near-field of the antenna.

Furthermore, the polarization can be used to measure the near-field volume of an antenna, and to find characteristic polarization volumes. We find that the auto-correlation of the polarization contrast is adversely affected in amplitude by the presence of a background focus, whereas the roll-off time is not. Thus, if the contrast can be measured, the near-field properties can be obtained with a polarization sensitive measurement, via the time constant of the roll-off.

Further, we have seen that the cross-correlation function of the two polarization channels has a peak at $\tau_{CC} > 0$. This time-delay is directly related to the distance between the two volumes. In the following chapter 6 we design a geometry which allows a calibration free measurement of the diffusion coefficient, with an intrinsic distance calibration provided by a polarization-sensitive nano-antenna design.

6

Nano-antenna enhanced two-focus fluorescence correlation spectroscopy

6.1 Introduction

Standard FCS implementations employ a single diffraction limited detection volume to deduce the mobility of particles from the mean diffusion time through a focus of known volume [34]. Therefore, accurate knowledge of the focus size and shape is required to correctly retrieve the kinetic properties of the specimen of interest. Deviations of the focus-shape from its ideal, due to aberrations or imperfect alignment, can significantly change the measured properties [41]. It is thus necessary to perform a reference measurement with a sample of known kinetic properties in order to calibrate the effective shape and size of the detection volume. In the case of nano-antenna enhanced FCS, the detection volume depends not only on the shape of the excitation beam, but also on the optical properties of the antenna at the pump and fluorescence wavelengths, the quantum efficiency [56], and even the ratio of the fluorescence decay time and the rotational diffusion time. This makes it challenging to perform proper reference measurements, because the reference specimen should have exactly the same photo-physical properties and similar hydrodynamic properties.

In dual focus FCS (2fFCS), the intensity fluctuations originating from two spatially separated volumes are measured and then cross-correlated. 2FFCS has proven to be a robust method to measure absolute diffusion coefficients, due to the fact that the distance between the two detection volumes can be precisely known in an experiment, even if the exact shape of the foci is prone to aberration and thus not exactly known [47, 48]. Hence, the distance between the molecular detection functions provides an intrinsic reference which allows the measurement of the absolute diffusion coefficient without additional reference measurements.

We now explore if the concept of calibration free 2fFCS can be implemented with an arrangement of nano-antennas, and how a nano-antenna enhanced cross-correlation experiment can mitigate or eliminate the problematic calibration of a nano-antenna

enhanced FCS experiment. Further we check if nano-antennas can reduce the complexity of 2fFCS experiments while preserving the benefits they provide, such as pump field enhancement, reduction of the detection volume, and enhancing the detection efficiency by directing emission into the detector [75]. First, we simulate a geometry of two orthogonally oriented nano-rods and find a vanishing cross-correlation peak due to high overlap of the two MDFs. We then improve the design with the use of an array of nano-apertures of alternating orientation, as nano-apertures have been proven to efficiently suppress background fluorescence [110].

6.2 Structure design and constraints

A 2fFCS experiment requires two molecular detection functions $MDF_1(\mathbf{r})$ and $MDF_2(\mathbf{r})$ which are spatially separated. Standard implementations are basically two FCS experiments integrated into a single microscope [111, 112], which allows separate alignment and free positioning of the two detection volumes in the sample. More compact designs use a Normaski prism [48] to send spatially overlapping laser modes of orthogonal linear polarization through a birefringent wedge, introducing a well defined tilt in the wavefront at the BFP of the objective, and thus two spatially separated excitation foci in the sample plane. A timeresolved detector collects the fluorescence from both foci. The origin of the fluorescence is deduced from the arrival time, as compared to the pulsed interlaced excitation of two lasers [47].

Here, we design a nano-structure which encodes the fluorescence emission originating from two different volumes into two orthogonal polarization channels in the far-field. This can be easily incorporated into a standard FCS setup, by adding a polarizing beam splitter and an additional detector. The measurement of the cross-correlation function imposes a range of requirements on the geometry. First, to use the cross-correlation peak as intrinsic distance reference, high visibility of the peak is needed. This requires a small spatial overlap of the two detection volumes. The height of the cross-correlation peak decreases with R^{-3} in the case of diffusion in the volume and with R^{-2} in a 2D system, e.g. diffusion at an interface. Therefore, the two detection volumes should be as close together as possible without introducing a significant spatial overlap, in order to yield a peak cross-correlation at finite time delays.

In this chapter we limit our design to measure diffusion in a 2D system, such as in a lipid bilayer [78, 108]. We assume a small fraction of the lipids to be labeled with a fluorescent marker. We choose gold as material for the nano-structures, which requires us to design the geometry for a red-fluorescent dye, e.g. Alexa647. This choice sets the spectral environment in which our nano-antenna should perform: 650 nm for excitation light and 670 nm for emission. Nano-structures can be fabricated easily on a glass substrate. The other half-space is assumed filled with water to accommodate the lipid bilayer. For all calculations in this chapter we will use a diffusion coefficient of $D = 4.5 \cdot 10^{-8}\mathrm{cm}^2/\mathrm{s}$, a typical value for a lipid-bilayer [108] at a concentration of $C_0 = 1 \cdot 10^{-13}\ 1/\mathrm{m}^2$. We assume the antennas to be embedded in a dielectric layer to planarize the interface and provide a flat plane, which we will refer to as *sample plane*, for the diffusing lipids in a membrane.

6.3 Gold nanorods

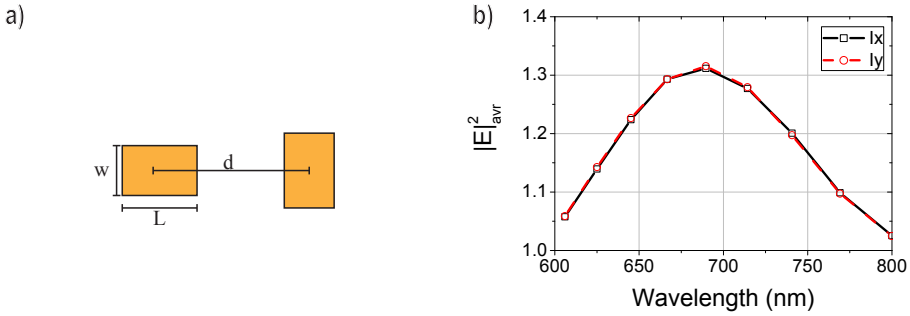

Figure 6.1: a) Sketch of the geometry of the two orthogonal nano-rods antennas. The length along the long axis is $L = 60$ nm, the width $w = 40$ nm and height 30 nm. The center-to-center distance of the two rods is $d = 120$ nm. b) Local field intensity $|E/E_0|^2$ in the sample plane averaged over the computation domain ($\approx 1.4\,\mu m^2$), when exciting with a normal incident plane wave of x-polarization (black solid lines) and y-polarization (red dashed line).

Metal nano-rods are the simplest nano antenna geometry that shows a polarization sensitive response. We therefore choose as building block a gold nano-rod of 60 nm length in the long axis aligned along x, a width of 40 nm and height of 30 nm which resides on a glass interface and is surrounded by water. This gives a plasmon resonance along the long axis at ≈ 660 nm vacuum wavelength, when exciting with x-polarized light. The spectral width of the resonance is broad enough to cover excitation (650 nm) and emission wavelength (670 nm). We then place a second nano-rod at a distance of 120 nm, now with its long axis aligned along the y axis, as illustrated in fig. 6.1a. This simple configuration localizes field intensities of different incident far-field polarizations into near-fields around the accordingly oriented nano-antenna. Additionally, excitation of one antenna, will result in highly polarized emission into the far-field. Therefore an isotropic source in close proximity to a nano-rod with emission frequency matching the long-axis plasmon mode, will efficiently excite the plasmon resonance. Measurement of the far-field polarization therefore allows to determine if the emitter is close to the x- or y- oriented nano-rod. Of relevance for an experiment is the near-field intensity in the sample plane. To assess the spectral match of the optical response of the antenna, we perform full wave simulation of the structure (as we will explain 6.3.1). The field intensities obtained from the full wave simulations in a wavelength range from $600-800$ nm are averaged over an area of $1.4\,\mu$m^2 in the the sample plane over the antennas. Figure 6.1b shows the average intensities for x-polarized excitation (black solid line) and y-polarization (red dashed line) and we find a good match with the desired operation wavelength.

6.3.1 Electromagnetic wave simulations

To verify if our nano-antenna system is suitable for 2fFCS experiments we need to obtain the MDFs for both detection channels. The next section explains how we obtain approximated molecular detection functions from full wave simulations. We assume the

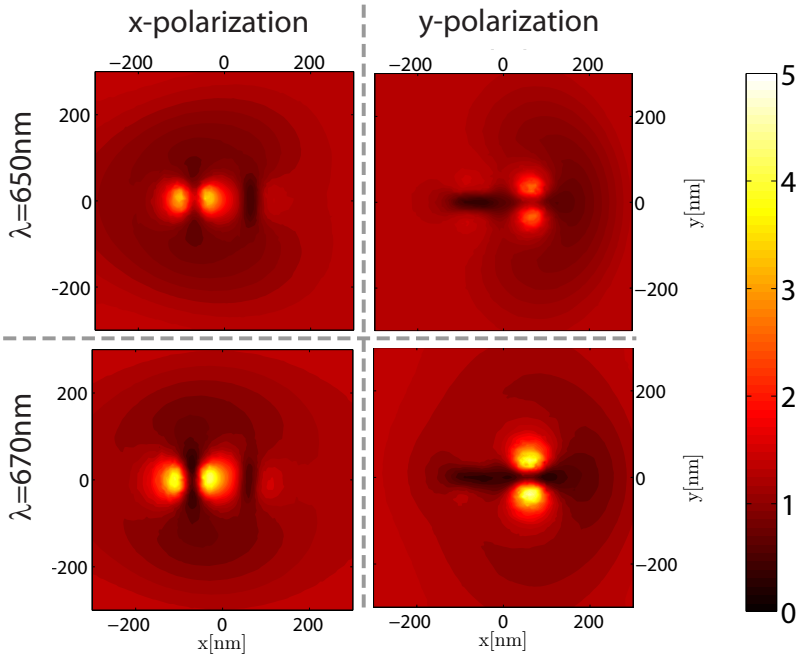

Figure 6.2: Near-field intensity enhancement $|E/E_0|^2$ in a plane 30 nm above from the top surface of the nano-rods for the excitation wavelength 650 nm and emission wavelength 670 nm each for x- and y-polarized excitation. All plots share the same colormap.

fluorophores diffuse in a plane as per definition of section 6.2. As the nano antennas present a geometric protrusion of 30 nm height to the flat substrate, the planarization layer, which would have to be fabricated to implement the experiment modeled here, would need to satisfy two opposing requirements. On one hand it must embed the nano-antennas and be sufficiently thick to provide a flat interface as diffusion plane. On the other hand to benefit maximally from the field enhancement the planarized interface should be as close as possible to the nano antennas. We choose the sample plane to be 30 nm above the nano antennas, corresponding to a total thickness of the planarization layer of 60 nm, as a compromise between the surface flatness and the local field enhancement.

The computation volume is composed of a cylinder of which one side is terminated with a hemisphere. The cylinder (ø≈ 1 μ m) represents the water volume ($n_{H2O} = 1.33$) which surrounds the gold nano-structures. For the optical properties of gold we use the tabulated dielectric function from [67]. The top volume is a hemisphere of glass $n_{glass} = 1.52$. In all simulations we use a plane-wave excitation, incident from the glass side, normal to the interface. All outer surfaces are terminated by perfectly matched layers. We perform four simulations, and all for normal incident plane waves: for the excitation and emission wavelength and each for x and y polarization. The obtained fields were evaluated on a square grid with 10 nm resolution and a width of 600 nm in each dimension. We show the field intensities in figure 6.2, in the plane of the diffusing fluorophores. In the following we will explain how we construct our MDFs from these four simulations.

6.3.2 Molecular detection functions

The molecular detection functions are in essence given by the excitation efficiency function (EEF) and the collection efficiency function (CEF) $MDF(x,y) = EEF(x,y,z_0) \cdot CEF(x,y,z_0)$. The EEF is the probability to excite the fluorophore at a given position and scales linearly with the pump field intensity. In an experiment, unpolarized or circularly polarized light would be used to excite the fluorophores close to both nano-rods with equal probability. Therefore we choose as EEF for both MDFs the sum of the excitation field intensities calculated for the two orthogonal linear input polarizations. The excitation causes a constant background intensity of the driving field in the sample plane. This is included in our EEF definition, to take into account that in actual measurements the background focus can have a large influence (see Chapter 3).

The second factor in the MDF is the CEF. This could be modeled by scanning a local point dipole source in the sample-plane and then integrate over the far-field emission into a solid angle- given by the collection system, as we have done in chapter 4. This requires multiple simulations for each point in the sample plane, which is computationally expensive. We here choose a computation procedure which is much more efficient and gives us a good approximation for the CEF with a single simulation for each polarization channel. We assume our collection to be only into one far-field mode, a plane wave of normal incidence. On the basis of reciprocity, the calculation of the near-field resulting from the incident plane wave provides us with the fractional radiative LDOS at each point in the sample plane, which corresponds to the radiation efficiency of a local source into a plane wave of normal incidence [71]. This is a good approximation for emitters which act as a constant-current source, such as fluorophores driven in saturation or low-quantum efficiency emitters. We use these near-field intensities as collection efficiency functions: $CEF_{(X,Y)} = I_{E,(X,Y)}$.

Now we have all information to calculate the molecular detection functions which

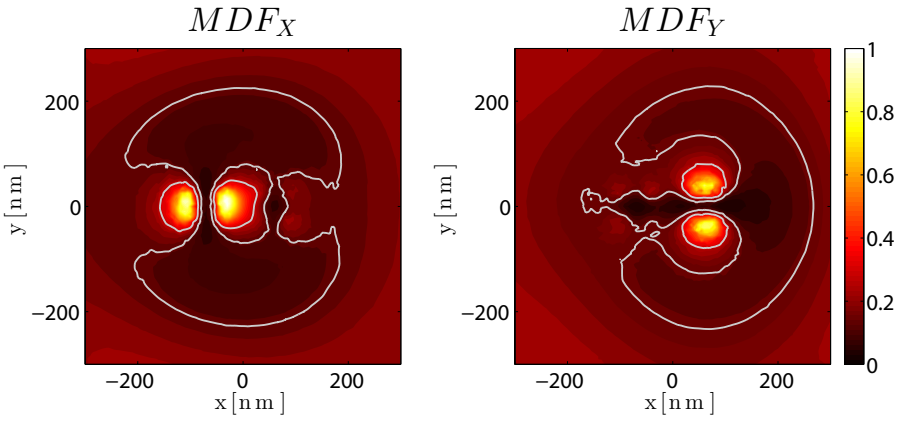

Figure 6.3: Molecular detection functions for x and y polarized far-field detection channels. As the scaling does not influence the calculated correlation function, the both MDFs are normalized by a common normalization factor, given by the maximum value of both MDFs. The grey lines indicate values of the MDF of 30% and 15% of the maximum. Far away from the antenna, in the corner of the computation box the MDF has a value of ≈ 20%.

correspond to the two far-field polarization channels, shown in figure 6.3:

$$MDF_X(x,y,z_0) = EEF(x,y)\cdot I_{E,X}(x,y,z_0)$$

$$MDF_Y(x,y,z_0) = EEF(x,y)\cdot I_{E,Y}(x,y,z_0).$$

To calculate the correlation function, we follow the same procedure as in Chapter 3, with the difference that now we have a two dimensional system and perform all calculations numerically with the calculated MDFs. We calculate the correlation curves numerically by calculating the time dependent solution $G_D(r-r';t)$ of the diffusion equation for a $\delta-$source in space and time at r' and $t=0$, and at evaluation point and time r,t. This solution is a Gaussian similar to the case of 3D free diffusion treated in section 2.1.2, and we evaluate it on the same 2D-grid on which we have mapped the MDFs. To calculate the ACF we compute

$$ACF(MDF_x,\tau) = \frac{\langle MDF_x\cdot[MDF_x * G_D]\rangle}{C_0\langle MDF_x\rangle^2}$$

where $\langle\rangle$ is shorthand for integration over the 2D plane at height z_0, and where $*$ indicates convolution over coordinates in the same plane. For the CCF we do the analogous calculation

$$CCF(MDF_x,MDF_y,\tau) = \frac{\langle MDF_x\cdot[MDF_y * G_D]\rangle}{C_0\langle MDF_x\rangle\langle MDF_y\rangle}$$

In figure 6.4 we show the calculated correlation functions. As the MDFs for x and y polarization are not identical, also the ACFs show different roll-off times of 2.5 ms in case of the x-polarization and 3.1 ms for the y polarization.The CCF rolls off in a similar fashion with a roll-off time of ≈ 4 ms. Unfortunately no peak in the CCF is observed that could be used as intrinsic distance calibration. The difference between the ACF and

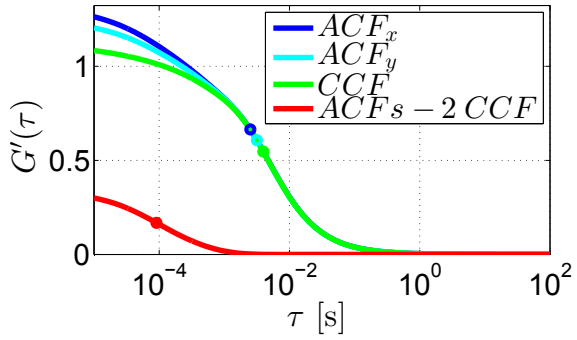

Figure 6.4: Auto- and cross-correlations of the orthogonal nano-rod antenna, when used in a FCS experiment. The ACFs correspond to FCS experiments conducted with MDF_x (blue) or MDF_y (cyan) assuming diffusion in a plane. The ACFs are not identical, due to differences in the MDF shapes and volumes. Both show a long roll-off with a characteristic time of 2.5 ms (MDF_x, blue dot), respectively 3.1 ms (MDF_y, cyan dot). The CCF (green), corresponding to a dual focus FCS experiment of the two MDFs, does not show a peak at nonzero time, as would be desired for implementing a calibration-free distance ruler in FCS. The CCF rolls off at 4.0 ms (green dot). The ACF of the polarization contrast (red), constructed as $(ACF_x + ACF_y - 2CCF)$ shows the shortest roll-off time of 0.091 ms (red dot).

CCF provides us with the characteristic times on which polarization fluctuates, as we have discussed in section 5.4 of the previous chapter.

We see that there is no peak at $\tau > 0$ in the cross-correlation function as a result of the high starting value of the CCF at $\tau = 0$. This is caused by the strong spatial overlap of the two MDFs.

To conclude, the nano-rod geometry is not suited for nano-antenna two-focus FCS. The antenna does provide two well-separated hot spots that are addressable by orthogonal polarizations. However, due to the background focus that enters both the MDF, both MDFs have a large spatial overlap. This overlap will dominate the cross-correlation, so that a distinct peak in the CCF at a time characteristic for diffusing from hot spot to hot spot does not appear.

6.4 Nanoapertures in a gold film

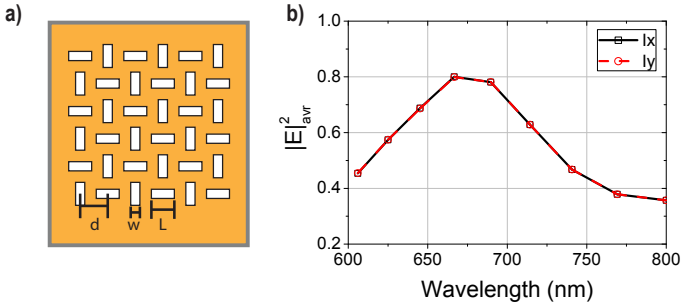

Figure 6.5: a) Sketch of the nano-aperture array. The apertures are arranged on a square grid with a pitch of $d = 120$ nm. The orientation of the apertures is alternating such that nearest neighbors alsways have opposite orientation. Dimensions of each aperture are $L = 100$ nm length and $w = 40$ nm width. b) Local field intensity in the sample plane averaged over an area of 1.41 μm^2, 30 nm away from the gold surface, calculated for a normal incident plane wave of x- (black solid lines) and y-polarization (red dashed lines).

In order to increase the amplitude of the cross correlation peak, we modify the geometry in two ways. First we make the structure periodic, such that the amplitude of the CCF increases, and second we turn to a nano-aperture geometry. This type of nano-structures has proven in single focus FCS to suppress efficiently the background, thus allowing to measure diffusion at ultra-high concentrations [20, 113]. The proposed structure consists of an optically thick gold-film of 100 nm thickness deposited on the glass surface which is perforated by nano-apertures. Each nano-aperture is rectangular with 100 nm length along the long axis and a width of 40 nm. The nano-apertures are arranged on a square grid with a nearest neighbor center-to-center distance of 120 nm. The orientation of the aperture alternates along the x or y axis, such that the nearest neighbors always have opposite orientations. This periodic arrangement has the advantage that the chance to detect an emitter in an aperture of opposite orientation does not require the diffusion from on aperture to another but from one aperture to any of four others which are all located at

the same distance. This increases the cross-correlation term by a factor of four, but keeps its shape and the peak position the same.

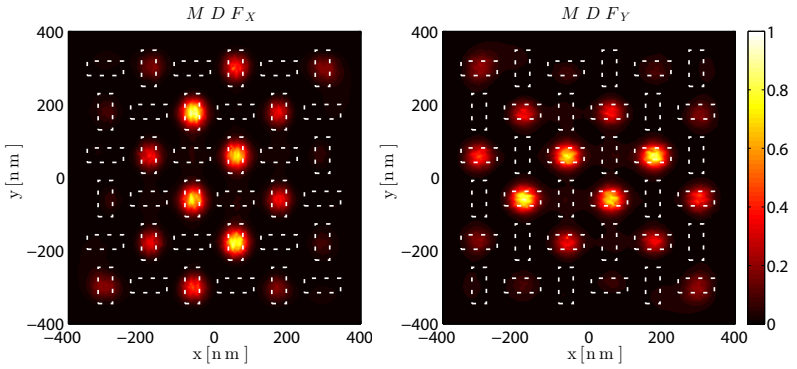

Figure 6.6: Molecular detection functions for x and and y polarized detection channel of a nano-aperture array in a plane of 30 nm above the gold surface. The MDFs are constructed by the local field intensities at 650 nm and 670 nm wavelength each calculated for x and y polarized excitation by a plane wave.The dashed lines indicate the outlines of the apertures. In the corners of the computation box the MDF has a value of approx. 2%.

6.4.1 Simulation correlation functions of diffusing sources

To test if the nano-aperture array allows high-contrast 2fFCS experiments, we perform the full wave simulations for the excitation and emission wavelength each with x- and y-polarized plane waves. Figure 6.6 shows the MDFs constructed in the same manner as previously for the nano-rod geometry. The sample plane is chosen 30 nm above the gold surface.

We find high intensities above nano-apertures oriented perpendicular to the driving field polarization, as expected according to Babinet-principle [114–116]. Even though the excitation field is a plane wave with equal intensities over the array, apertures in the center of the array show higher intensities, due to surface plasmon polaritions launched at the gold-dielectric interface [117].

The correlation function obtained for free 2D diffusion for MDFs calculated for the nano-aperture array are shown in 6.7. Both auto-correlation functions are indistinguishable (blue, cyan lines), indicating equal size and shape of the MDF for x and y polarization. Due to the presence of multiple displaced detection volumes, it does not roll-off smoothly, but shows a shoulder near 1 ms, and a roll-off time at 1.6 ms. The CCF (green) shows a peak at $\tau_{peak} = 0.65$ ms, proving that the nano-aperture design provides a sufficiently small spatial overlap between the x- and y polarized MDFs to perform a dual focus cross-correlation FCS. The auto-correlation of the polarization fluctuation ΔI (red) yields a roll-off time of 0.10 ms, corresponding to the diffusion time through a single aperture. Despite the fact that in the nano-aperture geometry many hot-spots are present, the higher correlation contrast compared to nano-rod geometry shows a smaller effective detection volume for the nano-aperture array, due to the effective blocking of the background field.

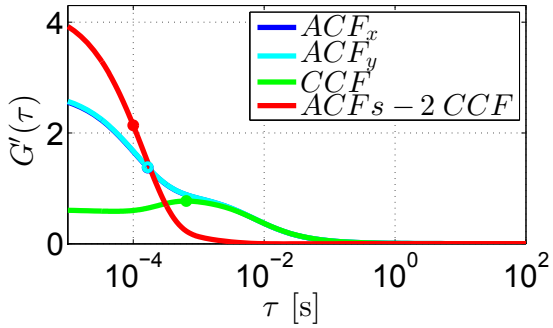

Figure 6.7: Various correlation curves obtained from the two MDFs shown in fig. 6.6. The two identical auto-correlations (blue,cyan) of the MDFs shows a bump in its roll-off, originating from the diffusion into apertures of same alignment. The spatial overlap of the two MDFs is sufficiently small, such that we observe a peak at 0.65 ms in the cross-correlation function (green dot). The auto-correlation of the polarization contrast as given by subtracting $2CCF$ form the sum of the $ACFs = ACF_x + ACF_y$ shows a shorter roll-off time of 0.10 ms (red dot).

6.4.2 Retrieval of the diffusion coefficient

In section 5.4 we have established that the cross-correlation signal expected when performing 2fFCS with two non-coinciding gaussians MDFs results in a peak correlation at a delay of $\tau_{peak} = \left(2R^2 - \sigma_i^2 - \sigma_j^2\right) / (8D)$. The roll-off time of the polarization fluctuations (fig. 6.7, red line) of $\tau_{\Delta I} = 0.10$ ms is a measure of the size of the individual hot-spot, not altered by a common background, as we have seen in sec. 5.4. We thus can calculate the individual hot-spot size σ from the roll-off time of the polarization fluctuation via $\sigma^2 = 4\tau_{\Delta I} D$, assuming circular symmetry of the hotspot. Knowing the position of the cross-correlation peak τ_{peak} and the distance between the two MDFs $R = 120$ nm allows to retrieve the diffusion coefficient: $D = R^2 / \left[4\left(\tau_{peak} + \tau_{\Delta I}\right)\right] = 4.8 \cdot 10^{-8}\mathrm{cm}^2/\mathrm{s}$. This is in good agreement with the value assumed that we assumed for the diffusion in numerical simulation of $4.5 \cdot 10^{-8}\mathrm{cm}^2/\mathrm{s}$.

The relevance of this result is that the alternating nano-aperture array geometry in cross-polarized FCS will allow a calibration free measurement of diffusion constants. Even though the precise shape of the MDF is strongly dependent on the actual nano-apertures shape, the distance to the metal surface and even on the properties of the fluorophore, the spacing between the holes and hence the MDFs is a robust quantity that is entirely independent of both emitter properties and imaging optics. This spacing translates into a calibration-free ruler for the diffusion coefficient. Determining the peak position in an correlation function obtained in a measurement can be difficult in the presence of noise. A more robust and more accurate method would be the global fitting of a model of two displaced detection volumes to the ACFs and the CCF [47, 82].

6.5 Conclusion and outlook

We have shown a nano-antenna design which encodes fluorescence emission in different spatial regions with high contrast into two orthogonal far-field polarization states. It

combines the advantages of calibration free 2fFCS measurement and the benefits of nano-antenna enhanced fluorescence spectroscopy, like smaller detection volumes, and pump and emission enhancements. The use of polarization sensitive nano-antennas to provide spatial selection reduces the complexity of 2fFCS experiments compared to existing far-field implementations. In the proposed nano-optical implementation, only the addition of a polarization splitter and one detector is necessary. In the excitation path, no additional source is needed.

The shown geometries are a proof of principle simulation and not optimized. The periodic array can further be tailored in such a way to beam emission lost in the SPP guided mode into the far-field, as shown in chapters 7, to increase the collection efficiency of the fluorescence. Furthermore other far-field channels could be used to address different near-field volumes For instance, [118] shows that dividing the radiation pattern in different channels allows to select distinct near-field volumes around complex nano-structures with sub-diffractive spacing.

Part III

Shaping fluorescence of an ensemble of emitters

7

Plasmonic hole array shapes spontaneous emission

7.1 Introduction

Achieving a complete manipulation of the generally weak optical signal from a single quantum emitter is a key objective in nanophotonics. To this end, two major routes have been investigated: plasmonic metal nano-structures [7, 15, 18–21, 57, 119–122] and dielectric photonic crystals [58, 123–131]. Both routes have demonstrated breakthrough results in tailoring the photoluminescence intensity, spectrum or directionality of single emitters. The plasmonic approach has put most emphasis on the nanoscale antenna element to control single emitter radiation [7, 15, 68, 132, 133] via the strong electromagnetic enhancement in the near-field of metals. In contrast, the photonic crystal approach centers on the use of coherent scattering to boost the interaction strength of intrinsically weakly scattering building blocks. State-of-the-art structures use thin high index membranes perforated by nano-apertures, in which the guided modes fold into a complex bandstructure. Spontaneous emission control then revolves around the targeted coupling of an emitter to select Bloch modes, with well-controlled out-coupling characteristics. Very recently, interest has emerged in the interplay between these two approaches, implying the use of a coherent array of plasmonics resonators to shape the luminescence emission properties. Two key examples are provided on one hand by the use of diffractive modes in 2D arrays of plasmon particles to shape emission of thin emissive layers [121, 122, 134–136], and on the other hand by the demonstration of Yagi-Uda antenna with a single quantum dot emitter in the optical regime [18], where coherent near-field coupling between scattering nanoparticles is determinant to achieve directional emission [120].

Here, we investigate the emergence of coherent antenna array effects to shape the fluorescence emission of single molecules in finite-sized bidimensional arrays of apertures milled into a metal film that supports surface plasmon guided modes. Transmission properties of quasi-infinite aperture arrays and single holes have been thoroughly investigated in the framework of extraordinary optical transmission [117]. As reviewed by Garcia-Vidal and de Abajo [137, 138], transmission measurements show sharp, dispersive features that

are frequently likened to a folding of the free surface plasmon dispersion relation into a bandstructure, where the scattering potential that sets the interaction strength is set by the single aperture polarizability. The influence of the array size was studied by Przybilla [139] and by Henzie [140]. The transmission of just a small patch of nano-aperture lattice is the well-known very broad single hole resonance, on which already for very small patches the sharp features of extraordinary optical transmission are superimposed. As function of patch size, these features sharpen and show small shifts. On basis of this work we examine if already in small nano-aperture patches, periodic lattice physics controls phased array antenna design for single molecules. We show the possibility of effective beamshaping by as few as 25 scatterers.

In this chapter, we show that the plasmonic crystal band structure of surface plasmon polaritons (SPP) is effective even in very small clusters of apertures to tailor the radiation pattern of single molecules and provide a substantial absolute increase in measured brightness per molecule. To support our experiment, we implement a general model to calculate the radiation pattern for arbitrary arrangements of nano-apertures driven by a single molecule, which enables the design of radiation patterns without symmetry constraints. For the specific case of periodic arrangements as in our experiment, the calculation ultimately reduces to a folding of the dispersion relation of the SPP dispersion into bands that emerge in the radiation patterns. While formally, a band structure, i.e., a sharp $\omega(k)$ relation, only exists in infinite, lossless systems, in the plasmonic case, the band structure pertains to lossy modes (radiative loss and absorptive loss). For perforated films, this band structure is well known, reveals itself in experiments as broadened bands, and is close to the folded free surface plasmon dispersion relation, in which narrow stop gaps open up [141–143]. In agreement with our data and full wave simulations, the model predicts strong directionality for frequencies near the closing of the second plasmon band, at the center of the Brillouin zone. We find that the local density of photonic states (LDOS) enhancement that we measure, is independent of the lattice and primarily determined by the central aperture. Fluorescence directionality and absolute extracted flux per molecule as caused by the phased array behaviour, can thus be tuned independently from LDOS enhancement.

The significance of this study is twofold. First, from a conceptual point of view, it investigates the build-up of directionality by coherent scattering in antenna arrays driven by a single emitter. Second, from an application-driven point of view, we demonstrate enhanced directional emission of fluorescence into a narrow angular cone that can be efficiently collected by a simple low numerical aperture optical lens. On basis of fluorescence correlation spectroscopy data, we provide quantitatively calibrated evidence of a large per-molecule brightness increase of 40 times in the forward direction. This property is desirable to achieve high sensitivity fluorescence detection with simple optical systems. The performance of our structures is on par with earlier work [20, 57, 144] that used nano-apertures surrounded by milled corrugations in so-called 'bull's eye' configuration. Conceptually, however, nano-aperture arrays have as major advantage that the emission characteristics rigorously factorize in a single hole 'structure factor', and an 'array factor' that encodes the geometric hole arrangement. This separation tremendously simplifies modeling, and opens up a rich set of beam shaping design options for metasurface substrates, much alike to the beam shape and polarization control possible with broad area

photonic crystal emitters [131]. Furthermore, we note that the aperture arrays reported here are technically much simpler to fabricate, for instance lending themselves to large-scale replication via soft conformal imprint techniques or template stripping [145–147].

This chapter is structured in the following way in the following way. First, the sample geometry and the experimental techniques are introduced in section 7.2. The measurements of the directionality of fluorescence emission are presented in section 7.3, together with the calibration measurements performed for each sample geometry. The measurements are reproduced with full-wave simulations in section 7.4. With a simple analytical model, developed in section 7.4, we explain the angular and spectral behavior of the different sample geometries.

7.2 Experiment

7.2.1 Sample design

In a direct plasmonic analogy of photonic crystals milled in dielectrics, we consider hexagonal arrays of nano-apertures milled in gold film, immersed in a dilute solution of fluorescent molecules (Figure 7.1). Our samples consist of a metal film deposited on a glass cover slide (Menzel Gläser #1.5, thickness: 0.17 ± 0.01 mm) by thermal evaporation. We first evaporated 2 nm chromium and then 150 nm gold (10^{-6} mbar, 0.6 Å/s). Several arrays of nano-apertures (140 nm) were milled into the metal film by focused ion beam (FIB) milling. In particular, the arrays are small periodic lattices of hexagonal or square symmetry.

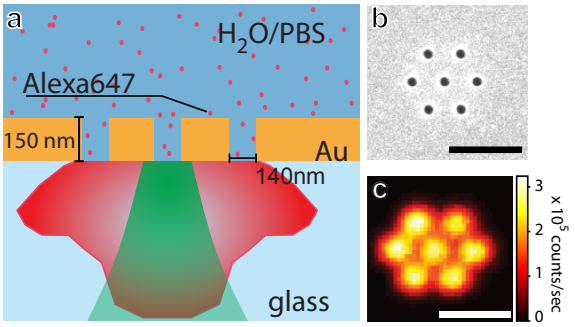

Figure 7.1: (a) Sketch of the sample consisting of a 150 nm thick gold film on glass with apertures of 140 nm diameter at 440 nm pitch. A drop of 1 μM solution of Alexa Fluor 647 in water saline solution is placed on top of the sample. (b) SEM image and (c) confocal fluorescence scan of a hexagonal array consisting of a central hole with one shell of apertures around it. The scale bars correspond to 1μm.

To obtain directed fluorescence emission normal to the sample plane, we design the plasmonic band structure so that the center wavelength for fluorescence emission for our fluorophore (around 660 nm) falls near a plasmonic band edge that closes at the Γ-point ($\mathbf{k}_{||} = 0$). This condition sets the pitch between neighboring apertures to about one SPP wavelength. Specifically, we fabricated lattices of 440 nm pitch using focused ion beam milling. A series of samples were generated with increasing number of rings of holes around a central aperture from 0 (single aperture) to 3, placing the holes in a hexagonal or

square lattice (hexagonal: 1, 7, 19, 37 unit cells across; Fig. 7.4(a-d)) or square (1, 5, 21, 37 unit cells across; fig. 7.5(a-d)).

To record the influence of the plasmonic band structure on single molecule fluorescence emission, we cover each sample with an aqueous solution of Alexa647 dye ($\approx 1\mu$molar Alexa647 in standard phosphate-buffered saline (PBS) solution), which infiltrates the nano apertures (Figure 7.1a). Diffusion ensures a continuous exchange of fluorophores in the aperture with the reservoir in the droplet and thus avoids photobleaching of the aperture fluorescence. The dipole orientation of the fluorophores in the liquid is random and constantly changing. Thus all measured quantities are averages over the dipole orientation.

7.2.2 Optical setup

The experimental setup is based on a confocal inverted microscope with a NA= 1.2 water-immersion objective, as shown in figure 7.2. The sample is mounted on a computer controlled XYZ piezo stage (Polytech PI P-517.3CD) and dye-solution is dropped on the sample and infiltrates the nano-apertures. A He-Ne laser (λ_{HeNe} = 633nm, continuous wave (CW)) is focused with a water immersion objective (Zeiss C-apochromat 40x, NA = 1.2) on the sample through the glass slide. For lifetime measurements, the excitation source is a picosecond laser diode operating at 636 nm (PicoQuant LDH-P-635, repetition rate 80 MHz). A single-mode optical fiber (Thorlabs P3-630A-FC-5) ensures a perfect spatial overlap between the pulsed laser diode and the CW He-Ne laser. The fluorescence signal is collected through the same objective and is separated from the pump laser light at a dichroic mirror. For confocal imaging and FCS we employ a 30 μm pinhole (effectively 375 nm in the sample plane). Single photon detection is performed by avalanche photodiodes (Micro

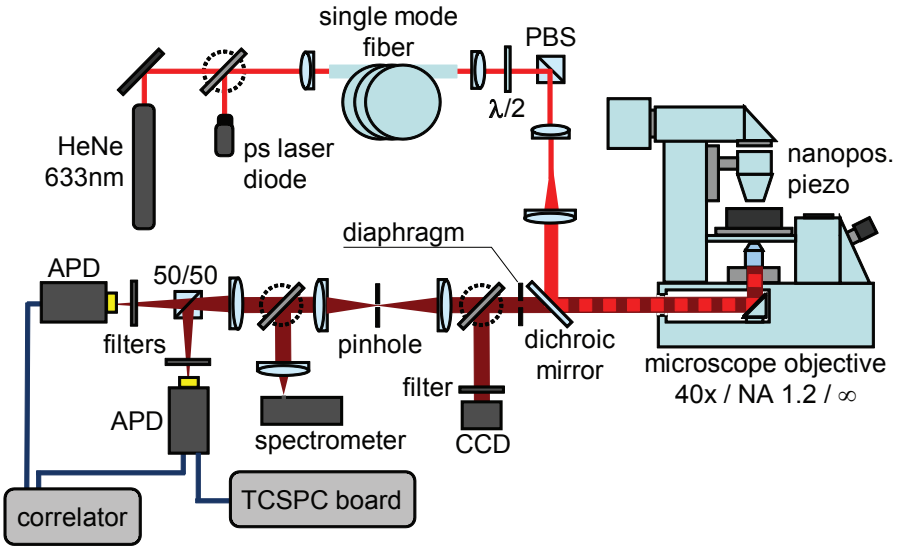

Figure 7.2: Diagram of the setup consisting of an inverted microscope, a CCD for Fourier imaging, and a set of APDs coupled to timing electronics as detectors confocal with the diffraction limited pump spot.

Photon Devices MPD-5CTC) in a Hanbury-Brown Twiss (HBT) configuration featuring a band pass filter (Omega Filters 640AELP) in front of each APD to further remove all scattered laser light. The fluorescence intensity temporal fluctuations are analyzed with a ALV6000 hardware correlator which computes the second order correlation function. We determine the average number of molecules contributing to the signal by fitting the analytical expression[79] for free diffusion FCS.

7.3 Experimental results

7.3.1 Calibration measurements

In our measurement protocol (set up diagram, see figure 7.2), we first perform confocal imaging. For each structure we first scan the sample in the xy-plane to acquire a confocal image (excitation power: 200 μW) of the fluorescence intensity using the APD photodetectors. We clearly resolve the individual holes (see fig. 7.1c) which are separated by 440 nm at count rates above 300 kHz when exciting the center of an aperture. The low count rate of < 1 kHz in the black areas of the scan shows that 150 nm thick gold effectively shields the fluorophores that are not close to a hole from being excited or coupling out. For all subsequent measurements of a structure we positioned the sample such, that only the center hole is excited. Thus, the driving source for the fluorescence emission stands in the molecules located in the central aperture, which serves as feed element for the rest of the antenna array.

As part of our measurement protocol, prior to assessing directionality, we benchmark the number of fluorescing molecules in the center aperture on basis of 'fluorescence correlation spectroscopy'. [148] This is performed by computing the second-order temporal correlation of the fluorescence intensity. An FCS measurement for the two-row hexagonal structure is shown in Figure 7.3 with the corresponding fit to standard diffusion theory [20, 79]. We find that for all structures, independently of the total number of holes in the

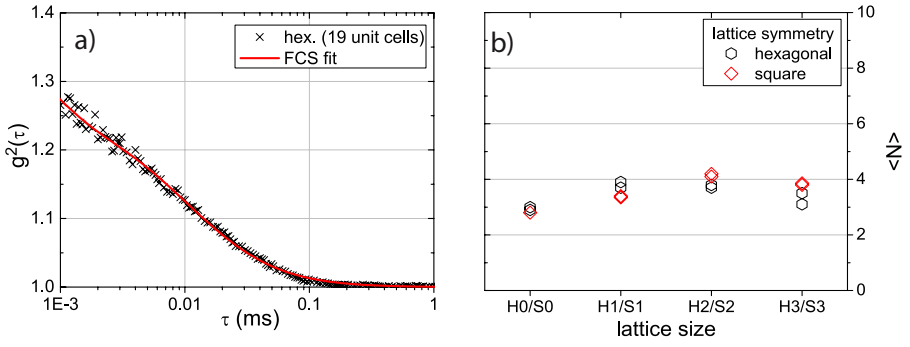

Figure 7.3: (a) Typical fluorescence correlation spectroscopy (FCS) trace. This trace is obtained from the central aperture in a hexagonal lattice of radius that is twice the pitch (two shells around the central hole). The data is excellently fitted according to the procedure in Ref. [20, 79]. We use the very same analysis method to extract the number $\langle N \rangle$ of molecules probed, plotted as a function of structure size in panel (b), for the square and hexagonal lattices (square resp. hexagonal plot symbols).

cluster, we detect almost the same number of contributing molecules ($\langle N \rangle = 3.5 \pm 0.7$). The diffusion time confirms that the fluorescence emission originates from molecules performing normal diffusion without sticking to any interface. In figure 7.3d (bottom) we plot the average number of molecules $\langle N \rangle$ for all measured structures and compare to reference measurements which we have taken in an open solution. Importantly we find that the average number of fluorophores measured for all nano-apertures falls in the range of $\langle N \rangle = 3.5 \pm 0.7$ and hardly depends on the structure surrounding the pumped hole. The small variation of at most 20% in $\langle N \rangle$ measured by FCS indicates equal geometric size of the apertures.

7.3.2 Back aperture images hexagonal samples

Next we turn to mapping of emission directionality, using back aperture imaging. For the back aperture imaging, we position a mirror behind the dichroic beam splitter to direct the fluorescence emission through a band pass filter (690 ± 20 nm) on a camera (Kodak KAF-1603, CCD with microlenses), while still only pumping the center-aperture with the He-Ne laser (now $P = 200$ μW; exposure time $T = 25$ s). The optical path between objective and CCD contains only bandpass filtering (690 ± 20 nm), but no lenses, and is about 1 m in length. In the backfocal plane (BFP) the intensity distribution corresponds to the angular emission pattern or 'fourier image' of the structure in the focal plane [149]. We collect all the emitted radiation and there is no spatial filtering by a pinhole as in the calibration measurements that employ the APD detectors. Figure 7.4 summarizes our main experimental results, namely the emergence of directivity for hexagonal lattices, as captured in the back focal plane images as function of lattice size. The radial coordinate in these images scales as the numerical aperture $\sin\theta$ for the emission, and thus the CCD images represent the intensity $I(\theta, \varphi)$ emitted from the plasmonic crystal structure for different angular directions, where θ is measured from the sample normal and φ is the azimuthal angle. Figure 7.4e) shows that a single aperture does not show any significant

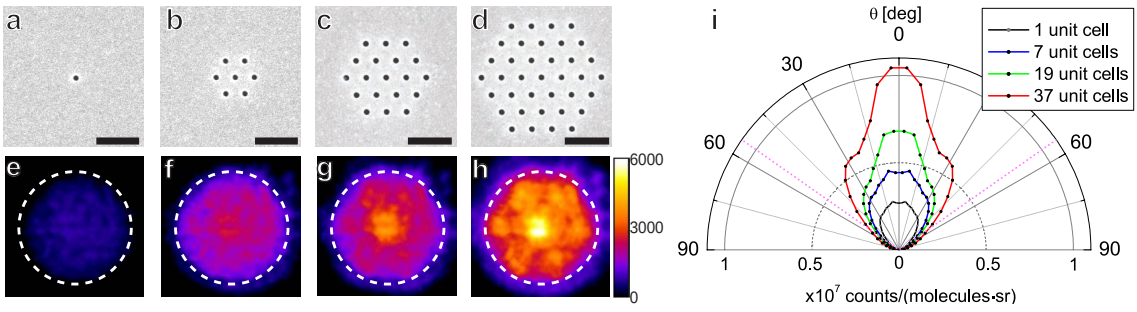

Figure 7.4: (a) Scanning electron micrographs of a single hole structure, and hexagonal clusters with (b) 7, (c) 19 and (d) 37 unit cells (one, two and three shells) around the central aperture (the scale bar is 1μm). (e-h) Back focal plane (Fourier plane) images representing the radiation patterns for the structures in (a-d). Note that only the central aperture was illuminated by the laser beam in these experiments. The colorbar represents a linear scale from 0 to 6000 counts per pixel. (i) Radiated intensity in counts per second per molecule per solid angle for hexagonal lattices of increasing number of apertures.

directional feature, although emission is more directional than a Lambertian emitter would be. In Fourier imaging with a high NA aplanatic objective, a truly lambertian emitter would in fact show as a disk with highest intensity at the edge of the BFP image [39, 150]. In stark contrast to the rather featureless single-hole radiation pattern, when the central aperture is surrounded by three shells of holes, the radiation pattern appears clearly structured (Figure 7.4d,h). In particular, a significant beaming is observed into the forward direction, and the central beam is accompanied by a set of six side lobes reproducing the sixfold symmetry of the lattice. Remarkably, we obtain directional emission despite the averaging over the emitter orientations. On one hand this demonstrates robustness of the observed directionality, while on the other hand further improvements might be possible if strategies to localize and orient sources on the nanoscale would be employed [18]. Although only the center aperture is excited, the entire lattice structure contributes to determine the angular distribution of the fluorescence emission. We relate this strong directionality in the normal direction to constructive interferences between the fluorescence light directly emitted from the central aperture into the far-field and the surface-wave coupled fluorescence emission that is scattered into the far-field by the neighboring apertures. A necessary condition for such constructive interference is that the aperture to aperture pitch corresponds to approximately one SPP wavelength on the gold/glass interface. This condition can be understood equivalently in k-space as requiring operation exactly at the condition of second order Bragg diffraction for the surface plasmon wave, i.e., at the closing of a plasmonic band near the Γ-point of the lattice. Importantly, the observation of strong directionality demonstrates that the neighboring apertures *coherently* re-emit the surface-wave fluorescence light stemming from a single molecule. Incoherent superposition of the fluorescence light emitted by different molecules would only result in the same featureless and broad radiation pattern observed for a single (isolated) aperture.

To quantify the directionality relative to the sample normal, we average back focal plane images over the azimuthal coordinate, taking into account the weighting caused by the objectives aplanatic lens construction [150]. Polar plots of the azimuthally averaged radiation patterns in Figure 7.4i demonstrate increased directionality correlated with growing structure size, in excellent agreement with the behavior expected for a coherent phased array antenna. On basis of the calibration of the average number of detected molecules for each sample, we can directly relate the radiation patterns to detected photon flux *per molecule* and per solid angle [20, 57]. This quantifies the fluorescence enhancement along each emission direction. Furthermore, we can also compute the directivity figure of merit for each antenna. In classical antenna theory, the directivity corresponds to the ratio of the radiated power density along the direction of strongest emission relative to the power density radiated by an ideal isotropic source emitting the same amount of total power [151].

For a single aperture, we measure a fluorescence enhancement of 10x integrated over the whole collection numerical aperture (as compared to the reference in solution without aperture), and a corresponding directivity of 3.4 dB [57]. For a hexagonal lattice with three shells, we record a fluorescence enhancement up to 40× into the forward direction, and a directivity of 4.3 dB. The enhancement and directivity clearly increase with lattice size, as expected from a spatially distributed phased array effect.

7.3.3 Back aperture images square samples

That a hexagonal lattice provides strong directionality is expected since the radial distance from the central aperture to the next row of apertures is uniquely defined, so that contributions from all apertures sum up constructively. In other words, the hexagonal lattice benefits from an almost circular Brillouin zone. This should be contrasted to the case of square lattices, that we also investigated to further confirm the defining role of the band structure for the radiation pattern.

We performed measurement on square lattices of different sizes, all with the same pitch of $a = 440$ nm as the hexagonal structures, and with the same hole size of 140 nm. Figure 7.5 shows scanning electron micrographs of the fabricated square structures (total size 1, 5, 21, 37 unit cells). As in the case of hexagonal arrays, we measured radiation patterns and observed increasing overall collected flux per molecule as the structure size increases. However, the radiation pattern is best characterized as a ring with a minimum into the forward direction. The maximum enhancement of 2.8× for the square lattice is located at an angle of $\theta \approx 20°$, whereas the enhancement into the forward direction is only 1.9×. This stark contrast with the hexagonal lattice data can be interpreted in k-space as firstly due to the Brillouin zone being more circular for the hexagonal case, and secondly through the fact that at the same pitch, the square lattice reciprocal lattice vectors differ by a factor of $\sqrt{3/4}$ in length.

7.4 Full wave simulations

7.4.1 Simulation method

Full wave calculations of radiation patterns were obtained using the COMSOL 4.3 finite element solver. Figure 7.6 shows the layout of the simulation domain, which is a cylinder with axis normal to the sample substrate that is a stack of water and the perforated gold film, on top of which we place a hemispherical dome of glass. As refractive indices we assume $n = 1.33$, $n = 1.52$ for water and glass, and a modified Drude model $\epsilon = \epsilon_b - \omega_p^2/(\omega^2 + i\omega\gamma)$ for gold [152], with $\epsilon_b = 9.54$, $\omega_p = 2\pi \cdot 2.148 \cdot 10^{15}$ Hz and $\gamma = 0.0092 \cdot \omega_p$. The simulation domain is closed on all sides with perfectly matched layers ($\sim \lambda/2$ thickness), except at

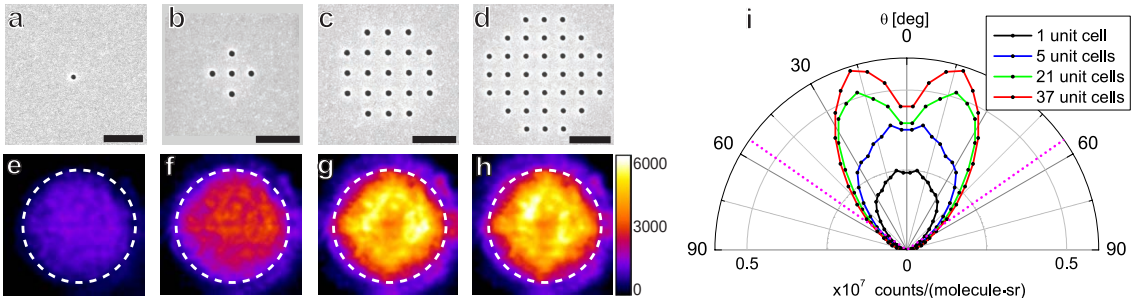

Figure 7.5: (a-d) Scanning electron micrographs of square lattices of different size (scalebar: 1μm), (e-h) corresponding radiation patterns and i) radiated intensity per molecule per steradian.

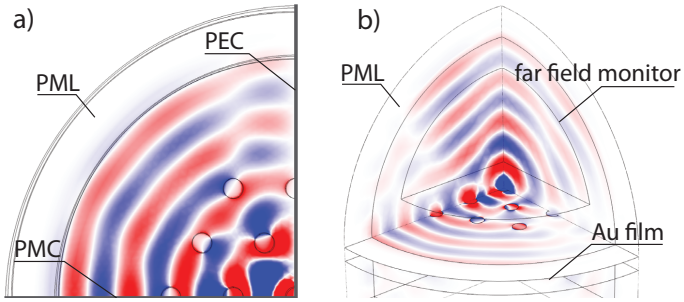

Figure 7.6: Layout of the COMSOL 4.3 finite element simulation. (a) Top view onto the sample plane, highlighting the periodic boundary conditions and absorbing boundary conditions used for an x-oriented dipole (color code shows a snapshot of the z-component of the electric field). We use the symmetry of the problem to reduce the size of the computation box. The symmetry plane normal to the dipole orientation is implemented as a perfect electric conductor (PEC), the symmetry plane parallel to the source is set as a perfect magnetic conductor (PMC). The entire computation domain is closed by perfectly matched layers (PML). The color indicates of z-component of the electric field amplitude at the gold-glass interface. b) Tilted view on the computation domain including the surface used to do the near to far-field transformation. The color coding here represents the amplitude of the x-component of the electric field.

the symmetry planes $x = 0$, $y = 0$ where perfect electric/magnetic conductor boundary conditions allow to reduce the computational load. To ensure accurate results we use a fine discretization < 10 nm of the metal surfaces, further refining the mesh near the interface into the metal, glass and water using boundary layer meshing. As source we place a current-carrying dipole in the center of the central hole mimicking the fluorescent molecule. We obtain ensemble averaging over random dipole orientation rigorously by summing the calculated angle-resolved far field fluxes over three orthogonal dipole orientations for which we do the simulations. In practice we found that the z-oriented dipole hardly contributes to far field radiation in both the hexagonal and square lattice.

We retrieve the far field by performing a Stratton-Chu near- to far-field transformation [153] of the fields that we calculate on the glass side on a spherical cap concentric with the central hole, that has a radius of 1.33 μm (3 wavelengths as measured in glass) and is truncated 300 nm above the sample surface. The near-to-far-field transformation requires choosing a surface on which to record the near-field. Since the Stratton-Chu integral is rigorously valid only for closed surfaces and in absence of stratification, the obtained far field should be viewed as a finite-truncation radius approximation to the angular spectrum representation integral that rigorously describes radiation patterns near surfaces [39]. By choosing as surface for the near to far field transformation a large dome concentric with the spherical wave seen to originate from the structure and by truncating the dome 300 nm above the sample surface, we find reasonably accurate far fields. A key aspect of this choice is that truncation of the dome above the surface removes unphysical contributions of the unscattered guided plasmon that appear if the surface is chosen closer to the gold film. Indeed, the dome ends above the evanescent tail of the guided plasmon so that it collects plasmon fields scattered out by the holes into the radiative continuum, but avoids contributions of the unscattered guided plasmon. On basis of benchmark comparisons of this approach to theory for dipole sources above unpatterned interfaces [154, 155], we

estimate accuracy to within $10-20$ %. We have furthermore established that the radiation patterns barely change if we increase the simulation box size, including the near-to-far field transformation dome by a factor 3 in radius (while keeping the same truncation height).

7.4.2 Simulation results

Figure 7.7 provides full wave simulation results for both the case of the hexagonal lattice, and the case of the square lattice, for select wavelengths in the emission spectrum of the fluorophore. For both lattices a transition occurs from beaming into the forward direction for long wavelengths, to emission into sidelobes for shorter wavelength. While for the hexagonal lattice the forward emission vanishes around 690 nm, for the square lattice the transition happens already around 750 nm owing to the factor $\sqrt{3/4}$ difference in reciprocal lattice size. We notice that the simulated radiation pattern does not change significantly in the spectral region of the experiment ($670-710$ nm). The simulation is consistent with the observed dip into the forward direction and the fact that most of the intensity is radiated into a ring at an angle of approximately 20° relative to the sample normal. We now return to the strongly directional radiation patterns evident for hexagonal lattices. The simulated radiation patterns bear a substantial dependence on the emission wavelength when considering the wavelenght range from 650 to 800 nm. We show in Figure 7.8b a fluorescence spectrum of Alexa Fluor 647 for reference. The radiation patterns show a marked transition from highly directional beaming into the forward direction for wavelengths of 700 nm and above, to a redistribution of the radiated power into six side lobes and no emission into the forward direction at wavelengths of 685 nm and below. The experimental back focal plane images actually result from spectral averaging over the range from 670 to 710 nm (grey shaded region in Fig. 7.8). This spectral averaging underlies our experimental observation of strong beaming normal to the sample *accompanied by* six side lobes for the hexagonal lattice.

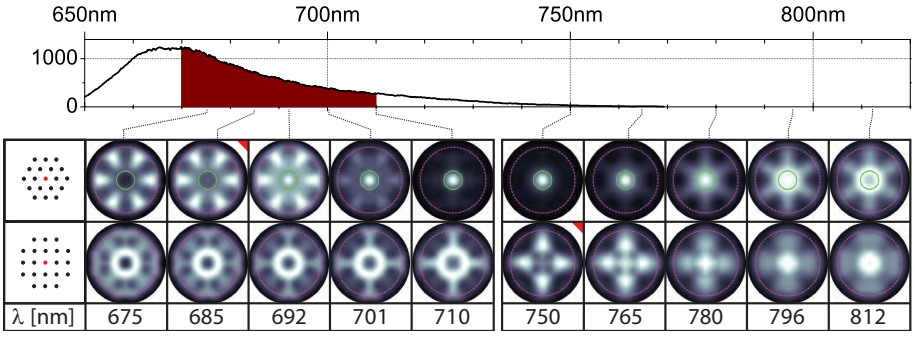

Figure 7.7: top) Fluorescence emission spectrum of a single nano-aperture infiltrated with Alexa647. The part of the spectrum filled in dark red denotes the spectrum transmitted by the bandpass filter in front of the CCD. bottom) simulated radiation patterns for different wavelength for the hexagonal and square S2 lattice. Radiation patterns marked with a red triangle indicate the wavelength where the beaming into forward direction has just stopped. To allow comparison to the experimental data, the magenta dashed line denotes the maximum collection angle of the experiment.

7.4.3 Experimental verification of predicted spectral dependence

To confirm experimentally the predicted spectral dependence of the radiation patterns, we record the fluorescence spectrum after placing a diaphragm of 2.9 mm diamater in the back focal plane (BFP image diameter 9 mm) to transmit only the radiation of the inner lobe (corresponding to the green circle in Fig. 7.7a). We report spectra for the structure analyzed in Fig. 7.4(d,h). The spectra with diaphragm (green solid line), without diaphragm (magenta dashed line) and the reference solution (black solid line) show marked differences in the region 700-740 nm. In particular, when we use the diaphragm to select only the central lobe, the spectrum clearly shows an extra emission shoulder in the red, consistent with the prediction from simulations that beaming is strong only for wavelengths to the red of a sharp cut-off at 700 nm (Figure 7.8b). The differences are better clarified by computing the fluorescence enhancement as compared to the confocal reference case (Fig. 7.8c). When only the central lobe is selected, we observe a significant spectral enhancement for wavelengths above 700 nm, indicating that the central lobe indeed contains significantly red-shifted fluorescence emission. This experimental finding stands in excellent agreement with the predictions from the simulated radiation patterns.

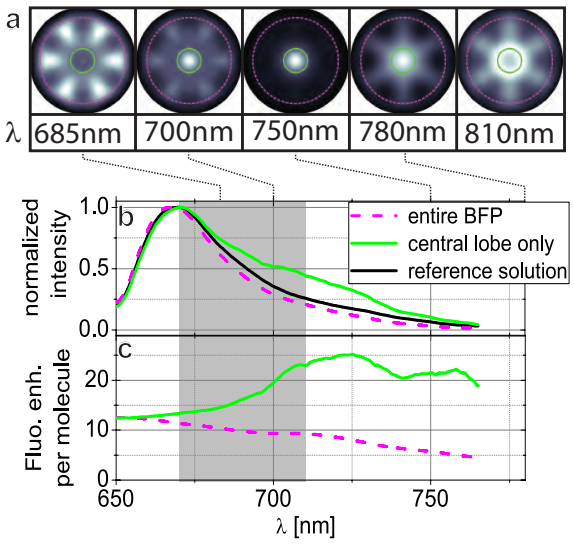

Figure 7.8: (a) Computed radiation patterns into the glass substrate for selected wavelengths assuming an isotropic ensemble of emitting dipoles in the central aperture surrounded by two shells of apertures in hexagonal lattice. (b) Normalized fluorescence spectra after placing a diaphragm (corresponding to the green circle in panel a) in the back focal plane to transmit only the radiation of the inner lobe. The reference solution spectrum appears in black, the hexagonal cluster with two shells and open diaphragm (full angular integration) is shown in magenta dashed line, and the closed diaphragm case is displayed in solid green line. (c) Enhancement of the fluorescence intensity per molecule with an open (magenta dashed line) or closed diaphragm (solid green line).

7.5 Analytical model

On basis of measurements and simulations, we conclude that the hexagonal clusters of apertures realize a nanoscale phased array antenna, where the required coupling between scatterers must be mediated via surface plasmon polaritons. To underpin this claim with a simple analytical model, we use a classical result from radiowave antenna theory [150, 151].

In the far-field of a phased array antenna of identical elements, the electric field along an observation direction $\hat{k}$ (vector of unit length) can be written as

$$\boldsymbol{E} = \frac{e^{ikR}}{R} S(\hat{k}) \sum_{n=1}^{N} A_n e^{-i\boldsymbol{k}\cdot\boldsymbol{r_n}} \tag{7.1}$$

where R is the radius of the observation sphere, and $\mathbf{k} = \omega/c\hat{k}$. Here, the first term is an overall spherical wave, and the second term $S(\hat{k})$ is the form factor of each single element, which is in the case of a single nano-aperture almost but not perfectly isotropic [144], and corresponds to the measured radiation pattern in Fig. 7.4e. The final term is the structure factor that is determined by the positions $\boldsymbol{r_n}$ and complex amplitudes A_n of the scatterers. If we set the apertures to be driven through the surface plasmon (SPP) waves launched at the central aperture, we can assume a complex amplitude $A_n = \frac{Ae^{ik_{SPP}r_n}}{\sqrt{r_n}}$.

The finite summation in Eq. (7.1) essentially represents a Fourier transform of the 2D source distribution represented by the cluster of scatterers. Conceptually, its evaluation can be simplified by recognizing that we are dealing with the product of (1) an infinite lattice, (2) a windowing function truncating the lattice to a finite set, (3) the surface plasmon phase term $e^{ik_{SPP}r}$, (4) the plasmon amplitude $1/\sqrt{r}$ that also acts as a windowing function. This construction of the source distribution is depicted in fig. 7.9. If we lump the finite lattice truncation and the $1/\sqrt{r}$ decay together in a windowing function W_N we can rewrite Eq. (7.1) as

$$\boldsymbol{E} = \left[\frac{e^{ikR}}{R} S(\hat{k})\right] \left[\mathcal{W}_{\mathcal{N}} * \sum_{\text{lattice}} e^{i(k_{SPP}r_n - i\boldsymbol{k}\cdot\boldsymbol{r_n})}\right] \tag{7.2}$$

As recognized by Rigneault [156] the infinite sum over the entire lattice k is formally equivalent to Harrison's construction [157] for the repeated zone scheme dispersion of the surface plasmon dispersion relation. The infinite sum results in a discrete set of circles of radius k_{SPP} centered at the reciprocal lattice vectors. This is easy to see, since the Fourier transform of an infinite lattice is its reciprocal lattice, while the Fourier transform of the phase factor $e^{ik_{SPP}r}$ is a circle of radius k_{SPP}. Since the Fourier transform of a product is a convolution of the Fourier transforms, this means that one obtains an infinite set of circles of radius k_{SPP} centered at the reciprocal lattice vectors. Thus our simple model shows an intimate relation between the finite structure array response, and the infinite lattice dispersion relation. In our approximation we neglect the actual perturbation that the holes impose on the surface plasmon dispersion by multiple scattering. For this reason we find the folded free surface plasmon dispersion. The rigorous band structure beyond the folded free surface plasmon dispersion approximation was defined and calculated by Lalanne et al.[143]. For the finite, lossy lattices studied here, the truncation windowing

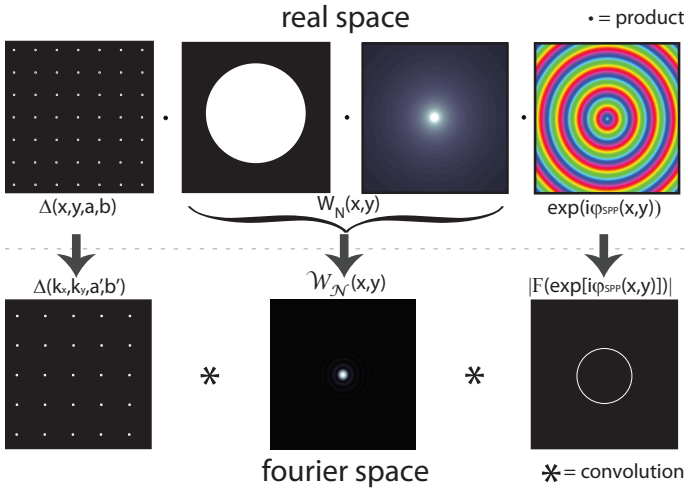

Figure 7.9: Source distribution (top row) decomposed into four factors (left to right): infinite lattice, a window function, the amplitude of the driving field and its complex phase (top row, left to right). The lower row shows the respective fourier transformations (FT). The FT of the infinite lattice gives the reciprocal lattice. The amplitude function W_N, given by the window function and the surface plasmon amplitude act as effective blurring $\mathcal{W}_{\mathcal{N}}$ of the amplitude distribution in reciprocal space. The phase factor yield a circle with the radius of the surface-plasmon wavelength. || denotes the absolute value, arg the phase of a complex number and F the fourier transform.

translates into a blurring of the infinite lattice band structure, formalized as a convolution with the Fourier transform $\mathcal{W}_N$ of the truncation W_N.

Figure 7.10 shows the folded dispersion relation of the hexagonal lattice as a ω, k-diagram, where we calculate k_{SPP} from the surface plasmon dispersion on the Au/glass

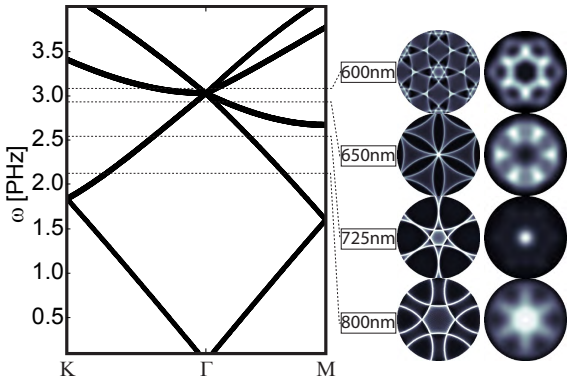

Figure 7.10: Band diagram of the folded dispersion relation of a hexagonal 2D lattice with zero interaction. Note that the vertical axis is in normalized frequency units d/λ_{SPP}, where in fact λ_{SPP} depends dispersively on optical frequency. Middle column: characteristic isofrequency cuts through folded wavevector space at selected frequencies indicated by dashed lines, that are well below, just below, and just above the 2nd order SPP Bragg diffraction condition. Right column: characteristic radiation patterns from COMSOL corresponding to the characteristic cuts of the dispersion relation.

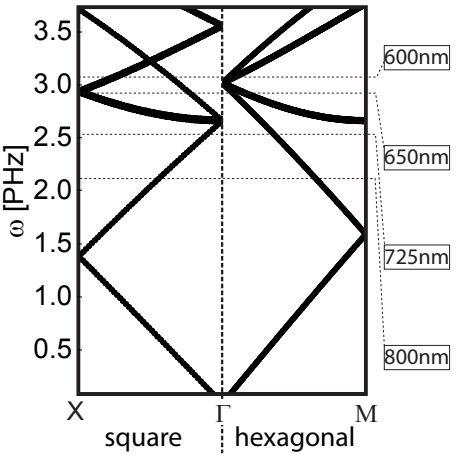

Figure 7.11: Crosscut along a reciprocal lattice vectors through the folded dispersion relation of a SPP on a Gold-glass interface for the square lattice (left) and the hexagonal lattice (right), both with 440 nm pitch.

interface. As per the design choice of lattice pitch, we expect the dispersion relation to cross the Γ-point in the dye emission spectrum, at 650 nm within the free SPP approximation. In a system with finite interaction strength one expects a red shift of the entire dispersion relation [143], and the opening of a small stop gap at the edge of the brillouin-zone, that pushes the lower band edge further to the red [122, 137, 141, 158]. For frequencies below the band edge, the allowed modes lie on a ring of wave vector close to $\boldsymbol{k}_{||} = 0$. As the wavelength sweeps from 750 nm to ~ 700 nm, we hence expect increasing directionality as the ring closes. As the band edge is crossed, emission is funneled into the next higher order band that doesn't close at the Γ-point. Consequently, a steep transition in the radiation pattern is expected to occur from a single lobe, to a six-lobed radiation pattern, as is indeed predicted by the full-wave simulations. We also fold the SPP dispersion relation with the reciprocal latices vectors of an square lattice. We compare both bandstructures in Fig. 7.11. For the square lattices the $\Gamma-$point crossing of the square lattice is redshifted out of the dye emission spectrum. Instead the fluorescence is coincident with the next higher band, hence exiting the sample off normal.

7.6 Lifetime measurements

Finally, for completeness, we also have measured the local density of states enhancement that the nano-aperture arrays provide. From the field of photonic crystals it is well known that redirection effects are not necessarily related to strong LDOS modifications. For instance, already at moderate index contrast marked redirection of emission, diffraction, and band-edge slow down of light [159–162] can occur although variations in spontaneous emission rates in such systems are small [163, 164].

For both the hexagonal and square samples, and for all patch sizes, we have measured fluorescence decay traces using time correlated single photon counting, pumping with a 636 nm pulsed diode laser. For fluorescence lifetime measurements, the APD output is coupled to a fast time-correlated single photon counting module (PicoQuant PicoHarp 300)

and correlated against the electronic trigger output of the pulsed laser diode. The temporal resolution of our setup for fluorescence lifetime measurements is 120 ps FWHM.

Independent of array type or size, we record fluorescence lifetimes in the range $\tau = 0.49 \pm 0.01$ ns (Fig. 7.12). Comparison with the lifetime of the open solution of $\tau_{\text{open}} = 1.03$ ns yields a significant shortening of the lifetime in the nano-aperture by a factor of 2.1. Through the known internal quantum efficiency, the measured *total* decay rate can be separated as the sum of an intrinsic non-radiative decay rate that is not modified by photonic environment, and the intrinsic radiative rate on which the photonic environment acts [68], where by definition the change exactly equals the LDOS normalized to the vacuum LDOS. Here the LDOS is rigorously defined as the imaginary part of the Greens function $\text{Im}\{G(\mathbf{r_0}, \mathbf{r_0})\}$ and contains the sum of all decay channels provided by the photonic environment [39]. This includes those decay channels related to decay into any plasmonic modes with strong near field enhancement, decay directly into the radiative continuum, and any quenching that is induced by the vicinity of the metal. Since the quantum efficiency of Alexa Fluor 647 is $\eta = 33\%$, we conclude that in all experiments, the molecules experience a significant LDOS enhancement by a factor $\frac{1}{\eta}(\frac{\tau_{open}}{\tau} - 1 + \eta) = 4.4$. Importantly, we find that the measured LDOS inside the central aperture is virtually independent of the lattice structure and not altered by the formation of a SPP band structure. Since Wenger et al. [79] already reported a complete study of the radiative and non-radiative decay channels in single nano-apertures, we don't pursue a decomposition into the distinct contributions that add up to the measured LDOS change here. The important conclusion for this work is that the nanophotonic control factorizes into two effects. On one hand directionality control and an increase in absolute count rate per molecule is provided via coherent reradiation by the entire phased array. As in the case of moderate index photonic crystals, this redirection effect is strong, although the periodicity has no strong effect on LDOS. Indeed, the LDOS is governed entirely by the geometry of the hole to which the fluorophore is directly coupled. A similar factorization to facilitate nano-photonic design was noted for plasmonic

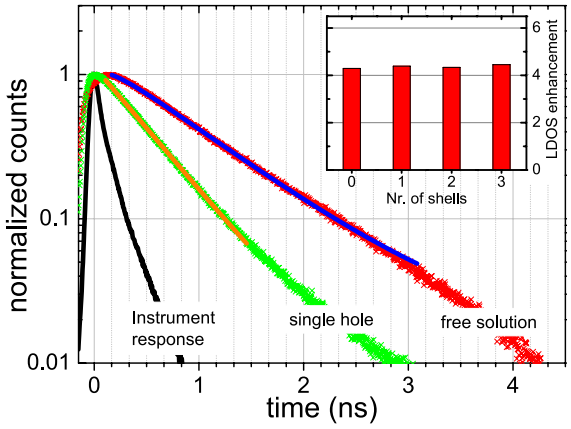

Figure 7.12: Normalized fluorescence decay traces for the reference solution (red markers) and the single aperture (green markers). The normalized decay traces for the hexagonal lattices with increasing number of apertures are found identical to the single aperture case. Solid lines are fitted decay curves, the black line represents the instrument response function. The insert shows the LDOS enhancement versus structure size.

Yagi-Uda antennas, where the entire array determines the overall directivity, while Purcell enhancement can be independently engineered by modifying only the feed element [120].

7.7 Conclusions

Hexagonal clusters of nano-apertures in a plasmonic film realize a nanoscale phased array antenna to control single molecule emission. The formation of a plasmonic band structure is a simple and powerful tool to tailor the radiation patterns of localized single emitters, enabling up to 40 times brightness enhancement per molecule in the forward direction in our experiment. We demonstrate that already small lattices with less than 25 elements show such highly directional emission that is set by the plasmonic crystal band structure, in excellent correspondence with numerical simulations. Interestingly, the single emitter radiation pattern can be tuned independently from the LDOS, as the 4.4-fold Purcell enhancement factor depends only on the geometry of the central hole that acts as feed element for the entire antenna.

Strong directionality of emission was reported earlier in two distinct plasmonic scenarios: on one hand for Yagi-Uda antennas that are interpreted as a travelling wave phased array antenna, and on the other hand for emission of ensembles of fluorophores tuned to diffraction resonances in infinite periodic arrays [121, 122, 134–136]. Here, we show that the very same mechanisms that are explored for infinite arrays of scatterers are already at play in small phased array antennas, as the band structure is evident in the emission pattern of single emitters in very small clusters of scatterers that are just a few unit cells across. This demonstration that infinite-system dispersion relations of diffractive modes can be used to taylor the behavior of phased array antennas that are very limited in size is complementary to the finding for Yagi-Uda antennas that directionality results from the infinite 1D chain dispersion relation [18, 120]. While Yagi-Uda antennas are limited to on-axis beaming, diffractive arrays allow much larger flexibility for beam steering, beam shaping and polarization control. Thereby our work opens a rich toolbox to engineer single photon emitters to emit selectively in particular angles, polarization states, or in more exotic beam profiles such as doughnut modes or orbital angular momentum beams. As compared to surface groove milling [20, 57, 144], the fabrication of array of apertures appears as a much simpler and robust technical solution. Indeed, while the structures presented in this manuscript were prototyped with focused ion beam milling, they can be manufactured on large scale using replication techniques such as imprint lithography [145–147].

8

Shaping fluorescence by a plasmonic metasurface

8.1 Introduction

In nano-optics, metal nano-particles are used as antennas for electromagnetic waves in the visible or infrared part of the spectrum [71, 165]. They allow localizing fields in much smaller volumes than the diffraction limit. As it is established for antennas in the radio frequency and microwave regime the spectral shape and polarization response of the scattered field of the nano-antenna can be tailored by shape and orientation of the particle. Two dimensional arrays of nano-particles, so called *Metasurfaces*, recently received strong interest for their ability to control the shape of a wavefront with a single layer of scatteres. To first order, a metasurface can be considered as a 2D plane (or sheet) in which an incident wave, e.g. a plane wave $Ee^{i\mathbf{k}\cdot\mathbf{r}}$, can induce locally a polarization of which the amplitude and phase is controlled on a per building block basis by design of each scatterer. Upon excitation, the induced polarization will act as a secondary source distribution. For instance, one could imagine a sheet of nano-particles at sub-wavelength spacing at coordinates $\mathbf{R}_m$ that have a complex tensorial polarizability α_m where the phase and magnitude of each polarizability tensor is individually optimized. If the particles only weakly couple so that they are mainly driven by the incident field, the amplitude and phase distribution of the polarizability is directly imprinted as an amplitude and phase distribution of the 2D source distribution, yielding a controlled output beam after Fourier transforming. For example, wavefront curvature can be changed, and metasurfaces thereby can form plasmonic lens [166, 167] despite being only 20 nm thick. The polarization state of transmitted beams can be modified to create singularities [168] or to generate beams with orbital angular momentum [62]. All these concepts act on far-field photons which interact with the metasurface and propagate again into the far-field. A unique feature that is advantageous for applications is that these meta-surfaces are effectively infinitely thin, or at least thinner than $\lambda/20$, whereas they perform functions that are usually solved through bulky secondary optics. Since they can be fabricated in a layer of a single height, the use of 3D sculpturing of material is not required. Thereby, metasurfaces promise

superior compactness in use and superior ease of fabrication. In particular, soft conformal imprint lithography could enable large scale replication of nanoscale metasurfaces with high fidelity.[145]

Our aim is to investigate in how far the concept of metasurfaces can be applied to spatially incoherent light sources embedded in the array, rather than the reflection, transmission and diffraction of a coherent plane wave as e.g. considered by Yu et al. [62]. Plasmonic structures have been successfully used to improve the conversion of blue light into longer wavelengths in particular through improvements in pump-field absorption on the one hand, and directional out coupling of light on the other hand [122]. In particular photo-luminescence enhancements above 50-fold have been achieved over narrow angular ranges (few degrees) using simple periodic plasmon lattices. Here we ask if the concept of plasmonic metasurfaces can be fruitfully applied to ensembles of incoherent local sources, such as fluorophores in light conversion layers.

This chapter is structured in the following way: in the following section 8.2 we choose the metasurface, compatible with fluorescence experiments and justify our choice of material and geometry of the nano-antennas. Section 8.4 explains the experiment and show polarization-resolved fluorescence radiation patterns for the designed metasurface and a reference structure. Section 8.5 describes the experiment with a simple single-scattering model neglecting particle-particle interactions and polarization. We verify the results by a full coupled dipole calculation, taking multiple scattering and polarization into account.

8.2 Structure and design strategy

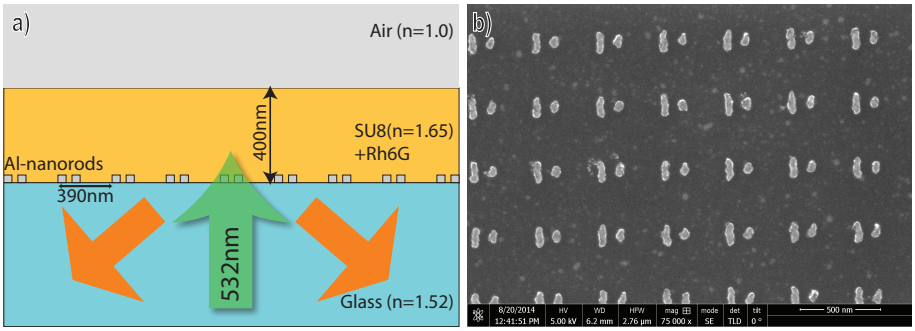

Figure 8.1: a) Schematic cross-section of the sample: an Al-nano-antenna array is located on a glass substrate and embedded in a 400 nm thick high-index polymer layer which is doped with Rh6G molecules. Excitation of the fluorophores is performed by a pulsed 532 nm laser though an oil-immersion objective at the glass side. Fluorescence emission is collected through the same objective. b) SEM-micrograph of the antenna array taken after lift-off before spin-coating the polymer layer. Dimension [l × w × h]: long antenna [130 × 40 × 30]nm; short antenna [70 × 40 × 30]nm; antenna distance (center to center) d = 120 nm; pitch: 390 nm.

In order to test the metasurface principle with local fluorescent sources, an antenna array compatible with the geometry and wavelength used in typical fluorescence experiments is required. We choose the geometry recently studied by Rodriguez et al. [135, 169] and by Schokker et al. [170], which consists of nano-antennas residing on a glass substrate (Menzel

Gläser, $n_{glass} = 1.52$), covered in a 400 nm thick layer of the high-index polymer *SU8*. Due to its high refractive index ($n_{SU8} = 1.65$), the photo-resist acts as single mode slab waveguide. Fluorescent Rhodamine 6G (Rh6G) molecules mixed in the polymer acts as ensemble of randomly oriented and randomly distributed dipole sources in our experiment, with a fluorescence emission band at 550 – 600 nm. In previous experiments directional photo-luminescence enhancement in the normal direction was achieved for square lattices of single plasmonic scatterers of pitch 380 – 400 nm. This distance corresponds closely to the wavelength in the waveguide. Hence in-plane second order Bragg diffraction of the waveguide mode and thus scattering out of plane, normal to the sample surface is favorable.

We now want to tailor a unit cell which provides a phase gradient to scattered light and thus acts as directional antenna. The resonance in a nano-particle imposes a phase shift on scattering varying from 0 to 180° when the resonance frequency is swept from the blue side to the red of the emission wavelength. The resonance frequency of plasmons can be tuned by size [166, 167], shape [62] or material [171]. As building blocks for our metasurface we choose metal nano-rods of different lengths. To gain phase contrast we require metal particles which exhibit a resonance around the fluorescence emission wavelength, when they are embedded in the high-index dielectric. The resonance wavelength of standard plasmonic particles (Au and Ag) of ≈ 50 nm size or above are already at longer wavelength than the desired 580 nm, and would further shift to longer wavelength when being embedded in the polymer. Aluminum provides a higher plasma frequency than Ag or Au, thus particles of the same geometry have a higher resonance frequency.

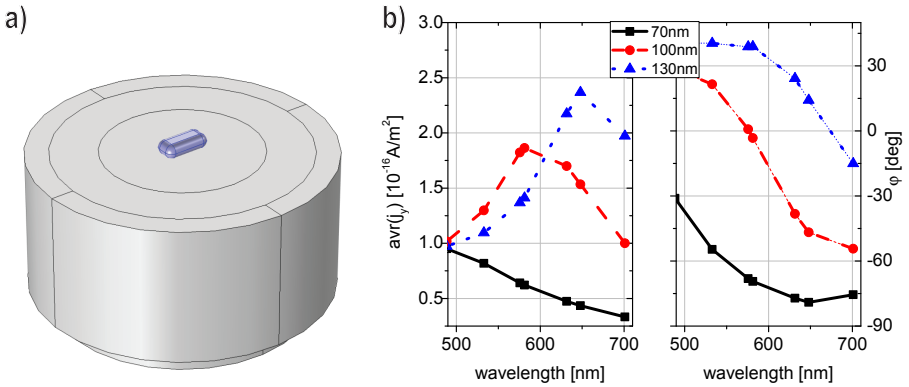

Figure 8.2: a) Screen shot of half the computation volume used in the Finite Element Maxwell solver [92]. In the center the aluminum nano-rod on a cylinder with the refractive index of glass ($n_{SiO_2} = 1.52$). The volume surrounding the antenna represents the high index resist SU8 ($n_{SU8} = 1.65$). The cylindrical computation box has a diameter of ø≈ 650 nm and a total height of ≈ 600 nm. The outer surface is terminated with a perfectly matched layer. b) Currents (left) and phase-lag to the driving field (right) of the volume-averaged current density along the long axis in three nano-rods of 70 nm (solid black line, squares), 100 nm (dashed red line, circles) and 130 nm (dotted blue line, triangles) length.

The scattered field amplitude and phase of aluminum nano-rods of different lengths is simulated with a commercial finite element Maxwell solver, COMSOL 4.3 [92]. For all simulations and calculation we use the dielectric function of aluminum given by Rakić

et al. in [172]. Simulations are performed in frequency domain and contain a single Al nano-rod ($l \times w \times h = [50-150] \times 40 \times 30$ nm^3) on the surface of a semi-infinite glass substrate, with its long axis aligned along the y-axis. The remaining volume is filled with the high index polymer. The computation volume has a cylindrical shape (ø≈ 600 nm, height ≈ 1.2μm) and the outer surfaces are terminated with perfectly matched layers (see figure 8.2,a). A y-polarized (along the long axis of the nano-rod) plane wave is used as excitation field, incident from the glass side (amplitude: $1\,V/m$), taking the Fresnel reflection at the glass-SU8 interface into account. We run the calculation for nano-rod lengths from $50-150$ nm in 10 nm steps. For each combination of geometry and frequency the current density averaged over the wire volume is extracted. This quantity peaks at the resonance, when most energy is stored in the resonator. Further the relative phase between the current in the wire and the driving field, both in y-direction, is calculated.

Figure 8.2,b shows the averaged current and the relative phase for three wire lengths $70, 100$ and 130 nm. While the resonance of the 130 nm wire (blue) is at approximately 650 nm wavelength and the shortest wire has its peak at a wavelength smaller than 500 nm, the 100 nm wire has its resonance at our design wavelength of 580 nm. Additionally, because of the strong phase difference of ≈ 100° between the scattered field of the 130 nm and the 70 nm wire, we choose these two elements as the building block to form a simple two element phased gradient antenna. We set the particle distance to 120 nm (see fig. 8.3a). This value is constrained by on one hand the expected unit cell size fo 380–400 nm across, and on the other hand minimum separations that can be reproducibly generated with electron beam lithography techniques.

To determine the directional properties of this dimer antenna, we performed full wave simulations. We enclosed the nano-rods by a virtual sphere which serves as a far-field monitor. The electromagnetic fields on the sphere surface are used to calculate the corresponding far-field radiation pattern by a near- to far-field transformation [93], as

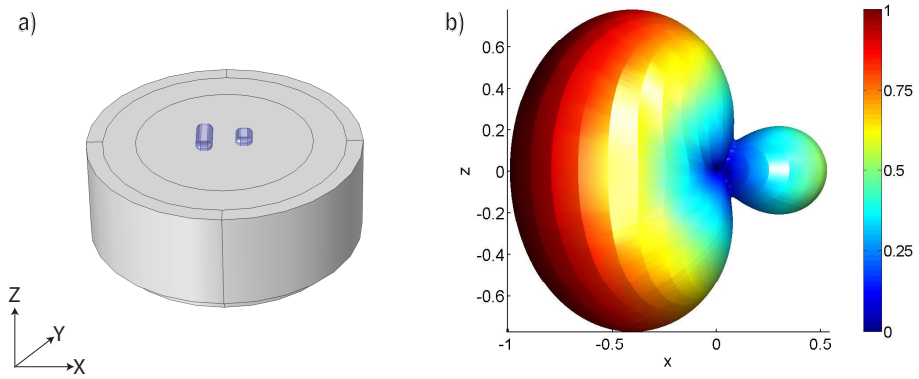

Figure 8.3: a) Simulated nano-rod pair: the centers of both nano-rods are aligned on the x-axis. The long nano-rod (130 nm) is centered at $x = -60$ nm and the short rod at $x = 60$ nm. b) Radiation pattern of the scattered field of the nano-rod pair in a homogeneous medium of 1.65. The nano-rods are excited with equal phases by a plane wave with a wavevector aligned along the z-axis. the radiation patterns is normalized to its maximum value, which occurs on the x-axis in negative directions, in the direction where the long nano-rod is located. In the positive direction, a factor 2 less power is radiated along x axis than in the negative direction.

we already used in chapters 4 and 7. To calculate the far-field accurately, the far-field monitor needs to enclose the entire scatterer and must be placed in a homogeneous medium, therefore the antenna is entirely immersed in the high-index resist ($n = 1.65$) and the glass interface is ignored. The scattered power (shown in fig. 8.3b) in the -x direction is more than twice the power scattered in to +x direction, for a driving field with a wavevector aligned along the z-axis and polarization along the long axis of the nano-rods. This two element phase-gradient antenna hence acts a directional scatterer, which scatters preferentially into the direction of the long nano-rod.

8.3 Sample fabrication and set up

To study the collective emission from dye distributed in the plane, we arranged the antennas in a 2d square array with a pitch of 390 nm. Figure 8.1,b shows a SEM micrograph of a fabricated phase-gradient antenna array. It was fabricated with electron beam lithography in a positive resist (ZEP520) on a glass cover slide with the conditions given in ref. [170]. Exposure was done using dot exposure with doses of $(1 - 1.5) \cdot 10^{-4}$ pC using an electron gun voltage of 20 kV and a current of 0.11 nA. After exposure we performed development of the resist in pentyl acetate, a 1:3 methyl isobutyl ketone / isopropyl alcohol mixture and isopropyl alcohol. Aluminum was deposited via electron beam evaporation at a pressure of $\approx 1 \cdot 10^{-6}$ mbar with an evaporation rate of 2 $Å/s$. Lift-off was later performed in anisole at $50°C$. On the same samples we also fabricated reference structures, that have only one rod per unit cell, instead of a dimer. To fabricate the waveguide with fluorophores on top of the antenna array, we use the negative photoresist SU8 and dope it with Rh6G by dissolving 5.25 mg of Rh6G perchlorate in 1 mL of cyclopentanone. The cyclopentanone with Rh6G is added to 1 ml of SU8-2005, after which we ultrasonicate the solution for 10 min. The solution has a Rh6G perchlorate concentration of 0.25 wt.%. Spincoating the SU8 solution at 2000 rpm on the antenna array samples, results in a $\approx$ 400 nm thick SU8 layer. Finally, the samples were baked for 2 min at $90°C$ to evaporate remaining cyclopentanone.

Our measurements are performed in a home-built fluorescence fourier microscope with pulsed laser excitation (Teem Photonics, type STG-03E-1S0) at 532 nm wavelength. A detailed description of the used setup is given by Schokker et al. in ref. [170]. The center of the nano-antenna array (dimensions 100 μm × 100 μm) is illuminated through an oil-immersion objective (Nikon Plan Apo λ 100 × /1.45 NA) with laser pulses of $\approx$ 500 ps duration with a maximum pulse energy of 4.5 μJ to excite the fluorescent molecules in the waveguide. The pump pulse passes a computer controlled acousto-optical modulator (AOM), which allows us to set the pulse energy which reaches the sample. The excitation hits the sample plane as a collimated beam, with an approximate diameter of 50 μm. This corresponds to a pulse energy density at the maximum AOM setting of $\approx$ 57 mJ/cm^2. The fluorescence is collected through the same objective and passes a dichroic beamsplitter (Semrock, Di01-R532-25x36) and a long pass filter (Chroma, HHQ545lp) to block the excitation light. After the spectral filtering, a polarization is selected with a linear polarizer (Thorlabs LPVIS100), and the back-focal plane (BFP) of the objective is imaged via a fourier lens [173] on a thermoelectrically cooled Si CCD (Andor CLARA). By this we measure the angular distribution of the fluorescence emission for vertical and horizontally

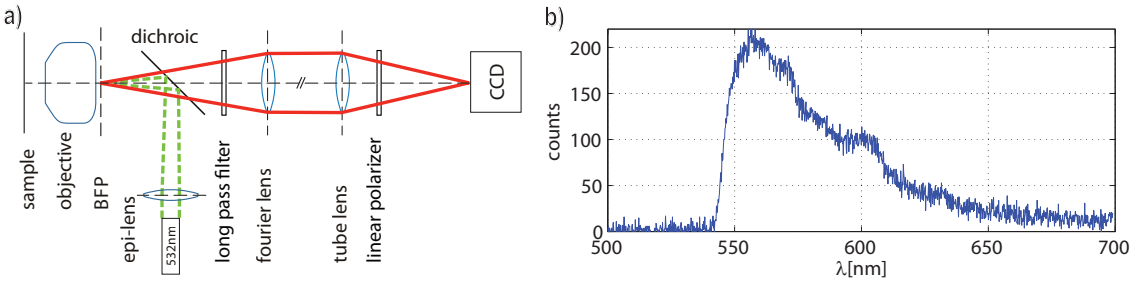

Figure 8.4: a) Schematic of the used fourier fluorescence microscope. The pulsed excitation laser (green dashed line) is focussed on the back focal plane (BFP) to give a collimated beam in the sample plane. The fluorescence emission (red solid line) is picked up by the same objective and the BFP is imaged by a fourier lens and a tube lens on a CCD. The green excitation light is suppressed by a long-pass filter. b) (right) fluorescence emission spectrum of Rhodamine6G in the SU8 resist layer, as measured after the long-pass filter.

polarization.

8.4 Measurement

Figure 8.5 shows angle-resolved fluorescence images of two different structures each at polarization parallel and perpendicular to the long axis of the nano-rods. Each plot corresponds to the sum of 10 measurements, each integrating over 10 excitation pulses with an intensity of 3% of the maximum AOM setting for the single nano-rod array, and 5% for the double nano-rod antenna array. Each fluorescence image is a back focal plane image, meaning that images appear as a bright disk of fluorescence with radius set by the maximum collection angle of the microscope objective. Since the NA is 1.45, this corresponds to emission at parallel wavevectors $k_\parallel / k_0 = 1.45$ where $k0 = \omega / c$, or equivalently emission angles into the glass of $\arcsin(1.45/1.52) = 72°$. The center of each image corresponds to fluorescence propagating along the optical axis, normal to the sample surface. The spatial coordinate in the images directly corresponds to parallel momentum. Besides the outer ring at the objective NA, a step like increase of fluorescence intensity is evident at $k_\parallel = k_0$ is caused by the fact that fluorescence at an air-dielectric interface is preferentially emitted at angles just above $NA = 1$, as shown in Ref. [39, 100].

Multiple intersecting circles of high intensity appear both in measurements of the phase gradient antenna array as well as for the reference structure of single rod emitters. For both structures the circles have the highest visibility in vertical polarization (fig. 8.5, right column), which corresponds to an electric field aligned along the long axis of the nano-rods in the sample plane and matches our expectation that the nano-rods scatter the strongest when polarized along their long axis. Measurements of the horizontal polarization are shown for the sake of completeness but we will focus the discussion on the vertical polarization.

We explain the generic features in the measurements by discussing as the example the reference structure (single rods) in vertical polarization, shown in fig. 8.5, top right. There are eight intersecting circles forming a cross-shape in the measurement of the

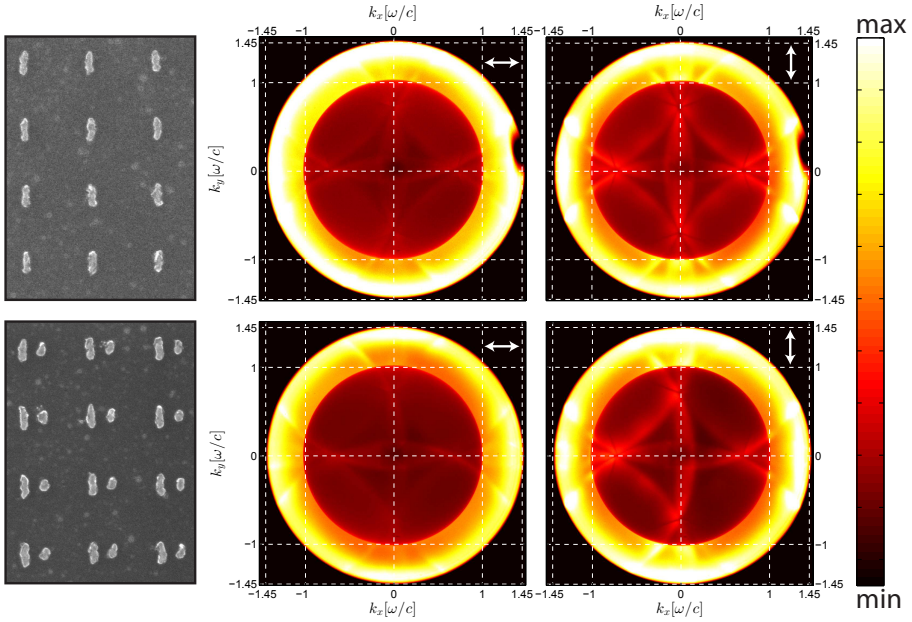

Figure 8.5: Left column: SEM micrographs of two samples: top) a single nano-rod per unit cell (excitation power $\approx 0.13\,\mu$J per pulse); bottom) or with two nano-rods of different size in a unit cell (excitation power $\approx 0.23\,\mu$J per pulse). The middle and right columns show the corresponding angular intensity distribution of the fluorescence in x-polarization (middle column) and y-polarization (right column). We list the minima and maxima of the color-scaling in each image: for the single rod array, x-pol. [1700−4300], y-pol. [3000−12000] and for the double-rod array: x-pol. [3500−14000], y-pol. [4000 − 13000], where numbers refer to CCD pixel counts. The obstruction at $[k_x, k_y] = [1.2, 0]\,k_0$ in the radiation patterns in the reference sample is due to an air bubble in the immersion oil during the measurement.

reference structure. A mode index of $k_{WG} = 1.57k_0$ at the 580 nm is obtained when calculating the dispersion relation for our wave-guide geometry (fig. 8.6c), by using the formula given in ref. [174, eq. 4.4 and 4.17]. The radius of curvature of the circular features in our measurement indeed corresponds well to $1.57k_0$. Therefore we conclude that the Fourier images represent a isofrequency cut through the repeated zone scheme waveguide dispersion relation, similar to our discussion in Chapter 7. Indeed we find in the experiment circles of this size, corresponding to a single frequency cut through the waveguide dispersion relation. Periodic scatters provide reciprocal lattice vectors, at which the photons in the waveguide can scatter. The reciprocal lattice vectors relevant in our measurement are located at $G = \frac{2\pi}{a} \cdot [n; m]$ with $n; m = -1, 0, 1$. Copies of the waveguide mode circle appear centered around each reciprocal lattice vector. The circle centered around the Γ-point ($[k_x; k_y] = [0; 0]$), corresponds to the bare waveguide mode and has parallel wavevector greater than the light line in glass. Hence it is not visible in our measurement. Only eight circles intersecting from reciprocal lattice vectors of nonzero momentum are seen. The circles are blurred due to spectral averaging over the fluorescence bandwidth of ≈ 50 nm.

For the single element unit cell, circles originating at $\frac{2\pi}{a}[0; \pm 1]$ and $\frac{2\pi}{a}[\pm 1; 0]$ intersect close to the Γ point, which means that in our experiment the waveguide mode has a slightly

higher momentum than the reciprocal lattice vector. In other words, the experiment was slightly detuned from the 2nd order Bragg diffraction condition [156]. Furthermore there are four circles originating from the diagonals $\frac{2\pi}{a}[\pm1;\pm1]$ intersecting on the x or y axis at approximately $\frac{3}{4}k_0$. The radiation pattern possesses the symmetries of the reference structure, i.e. two mirror planes along the x and y axis.

Now we turn to a discussion of the radiation pattern of the phase-gradient antenna array. Again intersecting circles are observed: most of the characteristics are the same, with the difference that the three circles originating at $k_x = 2\pi/a$ and $k_y = [-1;0;1]\cdot 2\pi/a$ show hugely reduced intensity. The radiation pattern as well as the structure do not posses a mirror symmetry around the y-axis anymore. Introducing a phase gradient in the unit-cell has translated into a selective asymmetric scattering at a subset of reciprocal lattice vectors. This shows that even for an incoherent ensemble of local sources, the concept of phase-gradient metasurfaces can be employed to shape the angular distribution of photons.

8.5 Modelling

To show how the directional scattering properties of each unit cell translate to an asymmetry in the band intensities measured in the far-field, we use a classical model from radio wave antenna theory [151]. The model assumes that radiation into the far-field originates from the induced polarization in the nano-antennas, which is given by the product of the local driving field A_n and a scalar polarizability α of each particle. In this scalar model the vector nature of the electric field is neglected and A is assumed to be a scalar complex-valued driving field, as we have previously done in chapter 7. As scalar polarizability the polarizability along the long axis of the nano-particle is used. The radiated field in viewing direction $\hat{k}$ reads

$$E = \frac{e^{ikR}}{R} S(\hat{k}) \sum_{n\in\text{lattice}} \alpha_n A_n e^{-i\mathbf{k}\cdot\mathbf{r}_n}$$

with r_n the position of the scatterer, A_n the complex amplitude of the driving field, α_n the scalar polarizability of the particle, and S the radiation pattern of the single element. The scattered field factorizes in the single element radiation pattern $S(\hat{k})$ and a factor determined by the array geometry [151]. This is analogous to solid-state physics where an x-ray diffraction pattern can be factorized in a structure- and form-factor [175].

For each antenna element we calculate the polarizability tensor in the waveguide environment, using a method explained in the following section 8.5.1. Our scalar model only uses the polarizability along the long axis of the nano-rods, a constraint that is relaxed in section 8.5.1. Figure 8.6 shows the absolute value (a) and phase (b) of the polarizabilities of the long (black dotted lines) and short (gray solid lines) nano-rod. The spectral behavior of this polarizability matches well with that of induced current in the FEM simulations (compare to fig. 8.2).

We decompose our antenna array into a two dimensional-δ-comb (comb denoted as Δ) representing the periodic lattice and two delta peaks, separated by a distance d, with different complex amplitudes mimicking the response of nano-antennas in the unitcell: $UC(\mathbf{r}) = \alpha_l\delta(-\frac{d}{2}) + \alpha_s\delta(\frac{d}{2})$. A convolution of both yields our phase gradient antenna array, as illustrated in the two left pictograms in the top of figure 8.7. Having defined the

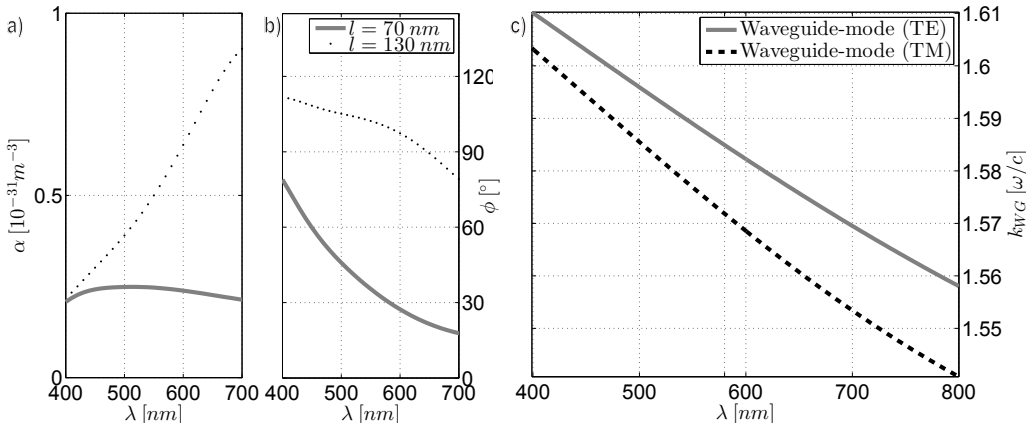

Figure 8.6: a) Absolute value $|\alpha_{y,y}|$ and b) phase $\arg(\alpha_{y,y})$ of the polarizability tensor along the long axis of nano-rods of 70 nm (gray solid lines) and 130 nm (black dotted lines). The phase shows an difference of 90° compared to fig. 8.6 due to the fact that, in a time-harmonic driving field, the polarization of a dipole is 90° out of phase with point-current. c) Relevant dispersion relations in dielectric slab: TE (gray solid line) and TM (black dashed line) waveguide mode.

geometry, we turn to describing the driving field. In the experiment our system is driven by an incoherent ensemble of point sources emitting in a fluorescence band around 580 nm (516 THz). To capture the essential physics, we take as driving source frequency 516 THz and describe the analysis for a single point source located at the the origin. Different source positions can be treated similarly using the Fourier shift theorem and give essentially the same results (not shown). The point source radiates a cylindrical wave of wavenumber $k_{WG} = 1.57k_0$ into the waveguide, that acts as driving for the phase-gradient antennas. Mathematically, the driving field for the antenna array reads $\tilde{A}_{wg}(\mathbf{r}) = e^{i|\mathbf{r}|\cdot k_{WG}} \cdot A_0 \cdot |\mathbf{r}|^{-1/2}$.

Returning to the evaluation of the infinite sum

$$\sum_{n \in \text{lattice}} \alpha_n A_n e^{-i\mathbf{k}\cdot\mathbf{r}_n}$$

we now realize that the source distribution that generates the field that is radiated into the far field is the product of the antenna array with the local complex valued driving field

$$J(\mathbf{r}) = [UC(\mathbf{r}) * \Delta(\mathbf{r}, \mathrm{a})] \cdot \tilde{A}_{wg}(\mathbf{r}) \tag{8.1}$$

as illustrated in the top row of fig. 8.7. The field radiated into the far-field is given by the fourier transform (FT) of the source distribution [151]

$$\iint J(\mathbf{r}) \cdot e^{-i\mathbf{k}\cdot\mathbf{r}} d\mathbf{r}\ .$$

that is easily obtained by calculating the fourier transform of each term in the factorization and using the convolution theorem. The real space configuration and their respective FTs are illustrated in fig. 8.7. $J(\mathbf{r})$ is a product of two factors, the lattice geometry and the driving field, with each of the factors constructed either by a convolution or a product. First we look at the FT of the geometry, constructed as the convolution of the lattice with the unit-cell. Fourier transforming the unit-cell gives a slowly varying but asymmetric

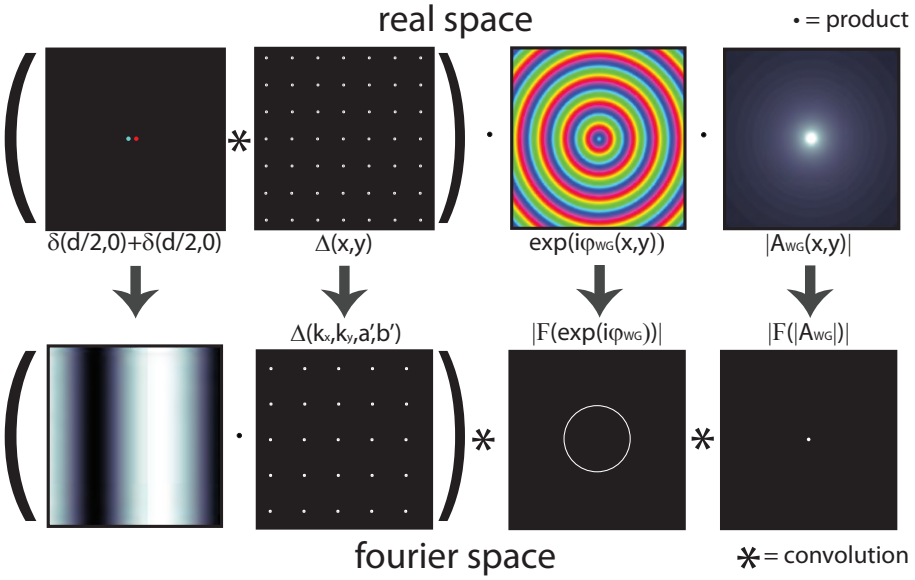

Figure 8.7: Illustration of the real space factorization and the respective fourier transform. The brightness of a pixel indicates amplitude, the color value indicates the phase. Top row shows depicts the real space representation of the direction antenna array, constructed via the convolution of the nano-rod-pair (left) of the single antenna with a periodic lattice of Dirac-δs. The constructed antenna array is multiplied with the driving field of a point source in the center with a radial phase profile (2nd from right) and a decaying amplitude (right). The bottom row shows the fourier transform of the corresponding functions.

sinusoidal amplitude modulation. Transforming the periodic square lattice with pitch a gives again a periodic square lattice with the pitch $2\pi/a$. Invoking the convolution theorem, the FT of the geometry, a convolution of two functions, is given by the product of the two FTs. This yields a square lattice multiplied with the FT of the unit-cell. The positions of the peaks are given by the square lattice, and their complex amplitude is given by the unit-cell [176].

We proceed with transforming the driving field, which is given by the FT of the phase factor convoluted with the FT of the amplitude factor. The phasemap yields an iso-frequency cut through the waveguide dispersion relation, which is a circle with radius $k_{WG} = 1.57k_0$. The FT of the amplitude function is a peak of finite size, but with a full width half maximum much smaller than $|k_{wg}|$.

The full radiation pattern can now be constructed as a convolution of the reciprocal lattice with the blurred circle of the waveguide mode. This results in copies of the WG circles centered around each reciprocal lattice vector, multiplied with the respective complex amplitude, as we show in fig. 8.8. The Γ-point in the center of the graph is enclosed by four intersecting circles. The circle centered around $[k_x, k_y] = [-k_{WG}, 0]$ shows an intensity $\approx 3\times$ higher than the circle centered around $[+k_{WG}, 0]$. Already this strongly simplified model captures the key features of the experiment, and explains well the asymmetry of the radiation pattern. Our simple geometry of two scatterers with a phase gradient, shows control over the relative scattering strength of left and right pointing reciprocal lattice vectors. Taking multiple scatterers with phase and amplitude in one

unitcell and using this simple design rule allows to enhance or suppress scattering at selected reciprocal lattice vectors.

8.5.1 Coupled dipole model

To check how the simplified scalar single scattering model compares to a full coupled dipole calculation, we implement a coupled dipole model (CDM) of an antenna array in the waveguide geometry [39, 174]. In the CDM each antenna is characterized by a polarizability tensor α. We now take the full tensorial character of the polarizability of the scatterers into account and calculate the polarizability tensor. Therefore we evaluate the static polarizability with the depolarization matrix of a rectangular volume [177] and the permitivity of aluminum, embedded in a background medium with the refractive index of SU8. We then add radiation damping to the polarizability, which we calculate by evaluating the imaginary part of the Greens function at the location of the scatterer in the layered medium [174].

In an array of N particles, the dipole moment induced in particle m is due to the total field at the particle position, which is the superposition of the driving field E_{inc} and the field scattered from all the other particles. This leads to a set of equations

$$\mathbf{p}_n = \boldsymbol{\alpha}\left[\mathbf{E}_{inc} + \sum_{n=1;n\neq m}^{N} \mathbf{G}(\mathbf{r}_m,\mathbf{r}_n)\mathbf{p}_n\right],$$

which can be solved self-consistently to obtain the dipole moments $\mathbf{p}_m$ of each antenna. The interaction between dipoles of different position is given by the Greens function $\mathbf{G}(\mathbf{r}_m,\mathbf{r}_n)$ of our waveguide geometry [39, Ch.10]. Including in total 1922 scatterers in the calculation, the modelled array covers a square area of approximately 12 μm × 12 μm.

As driving field we place a dipole source within the waveguide in the unit cell in the center of the array, and solve for the induced dipole moments in each antenna. We then

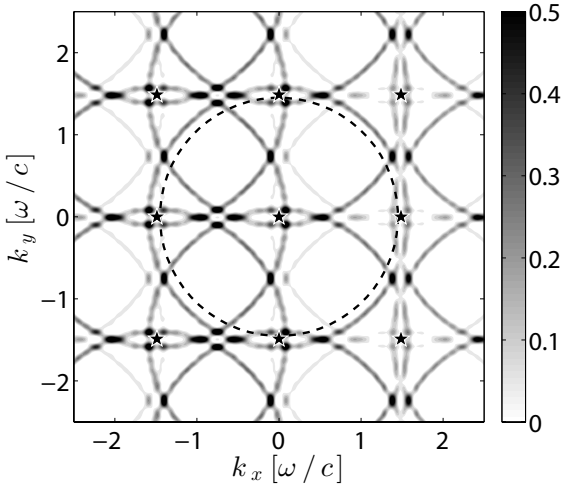

Figure 8.8: Numerical calculation of the radiation pattern by convolution of the waveguide dispersion relation (circles) with the reciprocal lattice (black pentagrams). Intensities are normalized to the maximum, the colorscale is linear. The black dashed circle indicates the maximum collection angle of $1.45k_0$ in the experiment.

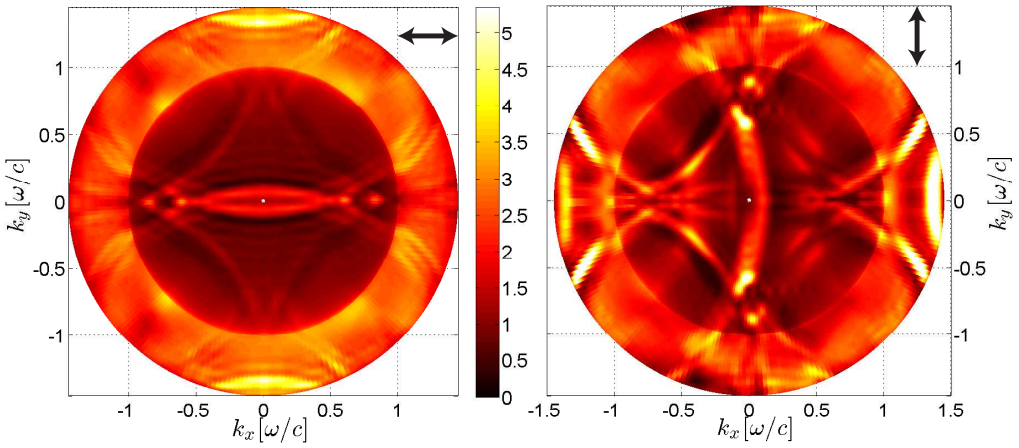

Figure 8.9: Radiation patterns of the PGAA for horizontal (left) and vertical (right) polarization, calculated with a coupled dipole model in the waveguide.

calculate the scattering into the far-field, using an approximated far-field Greens function and transform the angular emission into the back focal plane image according to the Abbe sine condition [39, Ch.3]. By that we obtain the full electric field, including polarization, in the BFP as they are then mapped in our experiment on our CCD. We calculate the far-field image for three orthogonal source dipole orientations at eight different positions inside the unit-cell volume in the waveguide. Finally we sum up the far-field *intensities* for each polarization channel of all the 24 calculations of different source orientations and positions. The result of the calculation are shown in fig. 8.9. Comparing to the measurements shown in fig. 8.5 we find good agreement and find all the key characteristics well reproduced by the CDM. In horizontal polarization, perpendicular to the nano-rod orientation, only

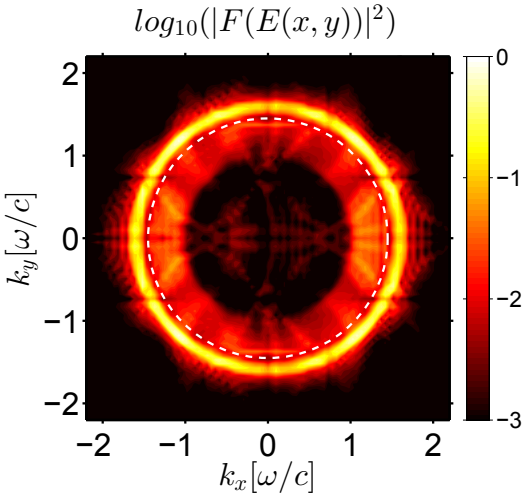

Figure 8.10: Angular power spectrum of the fourier transform of the electric field in the waveguide. In large part the amplitude is located in the unscattered waveguide mode. The white dashed line indicates the maximum collection angle of the objective at $1.45k_0$. The intensity is normalized to the maximum, the colorscale is logarithmic spanning three orders of magnitude.

minor left-right asymmetry is observed. In contrast, in y polarization, there is strong intensity from the waveguide modes scattered at $k_x = -2\pi/a$ and almost no intensity in those waveguide modes scattered at $k_x = 2\pi/a$.

The coupled dipole model also allows to evaluate the near-field in the waveguide. An interesting question is, if the directional scattering properties of the unit-cell also translate into an asymmetric population of the waveguide mode. To answer this question we calculate the near-field in the middle of the waveguide, 200 nm away from both the glass and air interface. We perform a 2d fourier transform for every field component for every source orientation at each of the 8 source positions. We then sum the power-spectrum for all polarizations for all source orientations and positions. The result is displayed in fig. 8.10, showing the parallel wavevector content of the fields inside the waveguide, plotted in a logarithmic colorscale spanning three orders of magnitude in wave vector intensity. We see that the highest amplitudes are in the waveguide mode centered around the Γ-point, confirming our intuition that the system is weakly scattering and justifying the assumption of the simplified model in the previous section. Around the circle perimeter we find only a minor modulation of the amplitude. For wavevectors $k_\parallel < \omega/c$, the maximum intensity is more than a factor 100 smaller than in the waveguide mode. Only a minor left-right asymmetry in population of the mode *inside* the waveguide is visible, in contrast to the asymmetry of the scattering *out* into the far-field.

8.6 Conclusion and outlook

We have shown that the concept of meta-surfaces allows to shape and transform the far-field emission pattern of ensembles of randomly positioned, incoherent emitters. The layer of fluorophores is a spatially incoherent source. Coupling the incoherent sources to a guided mode provides a high degree of spatial coherence within the guided mode and thus allows to control the angular distribution of the light scattering into the far-field by tailoring the spectrum of spatial frequencies [178].

Bibliography

[1] J. C. Maxwell, *A Dynamical Theory of the Electromagnetic Field*, Philos. Trans. R. Soc. London **155**, 459 (1865).

[2] E. Abbe, *Beiträge zur Theorie des Mikroskops und der mikroskopischen Wahrnehmung*, Arch. Mikrosk. Anat. **9**, 413 (1873).

[3] Rayleigh, *Investigations in optics, with special reference to the spectroscope*, Philos. Mag. Ser. 5 **8**, 261 (1879).

[4] K. Kao and G. Hockham, *Dielectric-fibre surface waveguides for optical frequencies*, in *Proc. Inst. Electr. Eng.*, volume 113, page 1151, 1966.

[5] E. Kuramochi, K. Nozaki, A. Shinya, K. Takeda, T. Sato, S. Matsuo, H. Taniyama, H. Sumikura, and M. Notomi, *Large-scale integration of wavelength-addressable all-optical memories on a photonic crystal chip*, Nat. Photonics **8**, 474 (2014).

[6] U. Kreibig and M. Vollmer, *Optical Properties of Metal Clusters*, Springer, New York, 1995.

[7] M. Agio and A. Alú, *Optical Antennas*, Cambridge University Press, 2013.

[8] J. Heber, *Plasmonics: Surfing the wave*, Nature **461**, 720 (2009).

[9] A. Polman and H. A. Atwater, *Photonic design principles for ultrahigh-efficiency photovoltaics*, Nature Mater. **11**, 174 (2012).

[10] J. R. Lakowicz, *Principles of Fluorescence Spectroscopy*, Springer, 3rd edition, 2006.

[11] M. Fleischmann, P. J. Hendra, and A. J. McQuillan, *Raman spectra of pyridine adsorbed at a silver electrode*, Chem. Phys. Lett. **26**, 163 (1974).

[12] R. Zhang, Y. Zhang, Z. C. Dong, S. Jiang, C. Zhang, L. G. Chen, L. Zhang, Y. Liao, J. Aizpurua, Y. Luo, J. L. Yang, and J. G. Hou, *Chemical mapping of a single molecule by plasmon-enhanced Raman scattering*, Nature **498**, 82 (2013).

[13] J. Aizpurua, T. Taubner, F. J. García de Abajo, M. Brehm, and R. Hillenbrand, *Substrate-enhanced infrared near-field spectroscopy*, Opt. Express **16**, 1529 (2008).

[14] P. Anger, P. Bharadwaj, and L. Novotny, *Enhancement and quenching of single-molecule fluorescence*, Phys. Rev. Lett. **96**, 113002 (2006).

[15] A. Kinkhabwala, Z. Yu, S. Fan, Y. Avlasevich, K. Müllen, and W. E. Moerner, *Large single-molecule fluorescence enhancements produced by a bowtie nanoantenna*, Nat. Photonics **3**, 654 (2009).

[16] H. Yuan, S. Khatua, P. Zijlstra, M. Yorulmaz, and M. Orrit, *Thousand-fold enhancement of single-molecule fluorescence near a single gold nanorod*, Angew. Chemie - Int. Ed. **52**, 1217 (2013).

[17] D. Punj, P. Ghenuche, S. B. Moparthi, J. de Torres, V. Grigoriev, H. Rigneault, and J. Wenger, *Plasmonic antennas and zero-mode waveguides to enhance single molecule fluorescence detection and fluorescence correlation spectroscopy toward physiological concentrations*, Wiley Interdiscip. Rev. Nanomed. Nanobiotechnol. **6**, 268 (2014).

[18] A. G. Curto, G. Volpe, T. H. Taminiau, M. P. Kreuzer, R. Quidant, and N. F. van Hulst, *Unidirectional emission of a quantum dot coupled to a nanoantenna*, Science **329**, 930 (2010).

[19] T. H. Taminiau, F. D. Stefani, F. B. Segerink, and N. F. van Hulst, *Optical antennas direct single-molecule emission*, Nat. Photonics **2**, 234 (2008).

[20] H. Aouani, O. Mahboub, N. Bonod, E. Devaux, E. Popov, H. Rigneault, T. W. Ebbesen, and J. Wenger, *Bright unidirectional fluorescence emission of molecules in a nanoaperture with plasmonic corrugations*, Nano Lett. **11**, 637 (2011).

[21] C. Belacel, B. Habert, F. Bigourdan, F. Marquier, J. P. Hugonin, S. Michaelis De Vasconcellos, X. Lafosse, L. Coolen, C. Schwob, C. Javaux, B. Dubertret, J. J. Greffet, P. Senellart, and A. Maitre, *Controlling spontaneous emission with plasmonic optical patch antennas*, Nano Lett. **13**, 1516 (2013).

[22] G. G. Stokes, *On the composition and resolution of streams of polarized light from different sources*, Trans. Cambridge Philos. Soc. **IX**, 233 (1852).

[23] M. Bawendi, *The Quantum Mechanics Of Larger Semiconductor Clusters* , 1990.

[24] C. G. Cremer, *Far-field Light Microscopy*, eLS. John Wiley & Sons Ltd., Chichester, 2001.

[25] D. Evanko, A. Heinrichs, and C. K. Rosenthal, *Milestones in light microscopy*, Nat. Cell Biol. **11**, 1165 (2009).

[26] J. D. Jackson, *Classical Electrodynamics*, Wiley, 3 edition, 1998.

[27] R. Loudon, *Non-classical effects in the statistical properties of light*, Rep. Prog. Phys. **43**, 913 (2000).

[28] R. Hanbury Brown and R. Q. Twiss, *A Test of a New Type of Stellar Interferometer on Sirius*, Nature **178**, 1046 (1956).

[29] B. Lounis and M. Orrit, *Single-photon sources*, Reports Prog. Phys. **68**, 1129 (2005).

[30] B. J. Berne and R. Pecora, *Dynamic light scattering: with applications to chemistry, biology, and physics*, Dover Publications, 2000.

[31] D. Magde, E. Elson, and W. Webb, *Thermodynamic Fluctuations in a Reacting System - Measurement by Fluorescence Correlation Spectroscopy*, Phys. Rev. Lett. **29**, 705 (1972).

[32] M. J. Levene, J. Korlach, S. W. Turner, M. Foquet, H. G. Craighead, and W. W. Webb, *Zero-mode waveguides for single-molecule analysis at high concentrations*, Science **299**, 682 (2003).

[33] J. Wenger, P.-F. Lenne, E. Popov, H. Rigneault, J. Dintinger, and T. Ebbesen, *Single molecule fluorescence in rectangular nano-apertures*, Opt. Express **13**, 7035 (2005).

[34] P. Schwille and E. Haustein, *Fluorescence correlation spectroscopy. An introduction to its concepts and applications*, Biophysics Textbook Online 1(3), Göttingen, 2001.

[35] P. Schwille, *Fluorescence correlation spectroscopy and its potential for intracellular applications*, Cell Biochem. Biophys. **34**, 383 (2001).

[36] J. Wenger, *Fluorescence enhancement factors on optical antennas: Enlarging the experimental values without changing the antenna design*, Int. J. Opt. **2012** (2012), Article ID 828121.

[37] G. Colas des Francs, a. Bouhelier, E. Finot, J. C. Weeber, a. Dereux, C. Girard, and E. Dujardin, *Fluorescence relaxation in the near-field of a mesoscopic metallic particle: distance dependence and role of plasmon modes*, Opt. Express **16**, 17654 (2008).

[38] A. Einstein, *Über die von der molekularkinetischen Theorie der Wärme geforderte Bewegung von in ruhenden Flüssigkeiten suspendierten Teilchen*, Ann. Phys. **322**, 549 (1905).

[39] L. Novotny and B. Hecht, *Principles of Nano Optics*, Cambridge University Press, 2006.

[40] H. Blom and G. Björk, *Lorentzian spatial intensity distribution in one-photon fluorescence correlation spectroscopy*, Appl. Opt. **48**, 6050 (2009).

[41] J. Enderlein, I. Gregor, D. Patra, and J. Fitter, *Art and Artefacts of Fluorescence Correlation Spectroscopy*, Curr. Pharm. Biotechnol. **5**, 155 (2004).

[42] I. Gregor, D. Patra, and J. Enderlein, *Optical saturation in fluorescence correlation spectroscopy under continuous-wave and pulsed excitation*, ChemPhysChem **6**, 164 (2005).

[43] H. Blom, L. Kastrup, and C. Eggeling, *Fluorescence fluctuation spectroscopy in reduced detection volumes*, Curr. Pharm. Biotechnol. **7**, 51 (2006).

[44] K. Hassler, M. Leutenegger, P. Rigler, R. Rao, R. Rigler, M. Gösch, and T. Lasser, *Total internal reflection fluorescence correlation spectroscopy (TIR-FCS) with low background and high count-rate per molecule*, Opt. Express **13**, 7415 (2005).

[45] A. Arkhipov, J. Hüve, M. Kahms, R. Peters, and K. Schulten, *Continuous fluorescence microphotolysis and correlation spectroscopy using 4Pi microscopy*, Biophys. J. **93**, 4006 (2007).

[46] L. Kastrup, H. Blom, C. Eggeling, and S. Hell, *Fluorescence fluctuation spectroscopy in subdiffraction focal volumes*, Phys. Rev. Lett. **94**, 178104 (2005).

[47] T. Dertinger, V. Pacheco, I. von der Hocht, R. Hartmann, I. Gregor, and J. Enderlein, *Two-focus fluorescence correlation spectroscopy: a new tool for accurate and absolute diffusion measurements*, ChemPhysChem **8**, 433 (2007).

[48] T. Dertinger, A. Loman, B. Ewers, C. B. Müller, B. Krämer, and J. Enderlein, *The optics and performance of dual-focus fluorescence correlation spectroscopy*, Opt. Express **16**, 14353 (2008).

[49] U. Meseth, T. Wohland, R. Rigler, and H. Vogel, *Resolution of fluorescence correlation measurements*, Biophys. J. **76**, 1619 (1999).

[50] P. Schwille, F. J. Meyer-Almes, and R. Rigler, *Dual-color fluorescence cross-correlation spectroscopy for multicomponent diffusional analysis in solution*, Biophys. J. **72**, 1878 (1997).

[51] I. Gregor and J. Enderlein, *Time-resolved methods in biophysics. 3. Fluorescence lifetime correlation spectroscopy*, Photochem. Photobiol. Sci. **6**, 13 (2007).

[52] P. Kapusta, M. Wahl, A. Benda, M. Hof, and J. Enderlein, *Fluorescence lifetime correlation spectroscopy*, J. Fluoresc. **17**, 43 (2007).

[53] A. Benda, V. Fagulová, A. Deyneka, J. Enderlein, and M. Hof, *Fluorescence*

lifetime correlation spectroscopy combined with lifetime tuning: new perspectives in supported phospholipid bilayer research, Langmuir **22**, 9580 (2006).

[54] M. Leutenegger, M. Gösch, A. Perentes, P. Hoffmann, O. J. F. Martin, and T. Lasser, *Confining the sampling volume for Fluorescence Correlation Spectroscopy using a sub-wavelength sized aperture*, Opt. Express **14**, 956 (2006).

[55] H. Rigneault, J. Capoulade, J. Dintinger, J. Wenger, N. Bonod, E. Popov, T. W. Ebbesen, and P.-F. F. Lenne, *Enhancement of single-molecule fluorescence detection in subwavelength apertures*, Phys. Rev. Lett. **95**, 117401 (2005).

[56] J. Wenger, B. Cluzel, J. Dintinger, N. Bonod, A.-L. Fehrembach, E. Popov, P.-F. Lenne, T. Ebbesen, and H. Rigneault, *Radiative and Nonradiative Photokinetics Alteration Inside a Single Metallic Nanometric Aperture*, J. Phys. Chem. C **111**, 11469 (2007).

[57] H. Aouani, O. Mahboub, E. Devaux, H. Rigneault, T. W. Ebbesen, and J. Wenger, *Plasmonic antennas for directional sorting of fluorescence emission*, Nano Lett. **11**, 2400 (2011).

[58] Q. Wang, G. Lu, L. Hou, T. Zhang, C. Luo, H. Yang, G. Barbillon, F. H. Lei, C. a. Marquette, P. Perriat, O. Tillement, S. Roux, Q. Ouyang, and Q. Gong, *Fluorescence correlation spectroscopy near individual gold nanoparticle*, Chem. Phys. Lett. **503**, 256 (2011).

[59] D. Punj, J. de Torres, H. Rigneault, and J. Wenger, *Gold nanoparticles for enhanced single molecule fluorescence analysis at micromolar concentration*, Opt. Express **21**, 27338 (2013).

[60] L. C. Estrada, P. F. Aramendía, and O. E. Martínez, *10000 times volume reduction for fluorescence correlation spectroscopy using nano-antennas*, Opt. Express **16**, 20597 (2008).

[61] S. Dutta Choudhury, K. Ray, and J. R. Lakowicz, *Silver nanostructures for fluorescence correlation spectroscopy: Reduced volumes and increased signal intensities*, J. Phys. Chem. Lett. **3**, 2915 (2012).

[62] N. Yu, P. Genevet, M. a. Kats, F. Aieta, J.-P. Tetienne, F. Capasso, and Z. Gaburro, *Light propagation with phase discontinuities: generalized laws of reflection and refraction.*, Science **334**, 333 (2011).

[63] A. A. Kinkhabwala, Z. Yu, S. Fan, and W. E. Moerner, *Fluorescence correlation spectroscopy at high concentrations using gold bowtie nanoantennas*, in *Chem. Phys.*, volume 406, pages 3–8, Elsevier B.V., 2012.

[64] D. Punj, M. Mivelle, S. B. Moparthi, T. S. van Zanten, H. Rigneault, N. F. van Hulst, M. F. García-Parajó, and J. Wenger, *A plasmonic 'antenna-in-box' platform for enhanced single-molecule analysis at micromolar concentrations*, Nat. Nanotechnol. **8**, 512 (2013).

[65] G. Mie, *Beiträge zur Optik trüber Medien, speziell kolloidaler Metallösungen*, Ann. Phys. **330**, 377 (1908).

[66] C. T. Tai, *Dyadic Green Functions in Electromagnetic Theory, 2nd Ed*, IEEE Press, 1994.

[67] P. B. Johnson and R. W. Christy, *Optical Constants of the Noble Metals*, Phys. Rev. B **6**, 4370 (1972).

[68] H. Mertens, A. F. Koenderink, and A. Polman, *Plasmon-enhanced luminescence*

near noble-metal nanospheres: Comparison of exact theory and an improved Gersten and Nitzan model, Phys. Rev. B **76**, 115123 (2007).

[69] J. R. Lakowicz, K. Ray, M. Chowdhury, H. Szmacinski, Y. Fu, J. Zhang, and K. Nowaczyk, *Plasmon-controlled fluorescence: a new paradigm in fluorescence spectroscopy*, Analyst **133**, 1308 (2008).

[70] R. Sprik, B. A. van Tiggelen, and A. Lagendijk, *Optical emission in periodic dielectrics*, Europhys. Lett. **35**, 265 (1996).

[71] P. Bharadwaj, B. Deutsch, and L. Novotny, *Optical Antennas*, Adv. Opt. Photonics **1**, 438 (2009).

[72] R. G. S. El-Dardiry, S. Faez, and A. Lagendijk, *Classification of light sources and their interaction with active and passive environments*, Phys. Rev. A **83**, 031801 (2011).

[73] J. N. Anker, W. P. Hall, O. Lyandres, N. C. Shah, J. Zhao, and R. P. Van Duyne, *Biosensing with plasmonic nanosensors*, Nat. Mater. **7**, 442 (2008).

[74] P. L. Stiles, J. a. Dieringer, N. C. Shah, and R. P. Van Duyne, *Surface-enhanced Raman spectroscopy*, Annu. Rev. Anal. Chem. **1**, 601 (2008).

[75] V. Giannini, A. I. Fernández-Domínguez, S. C. Heck, and S. A. Maier, *Plasmonic nanoantennas: Fundamentals and their use in controlling the radiative properties of nanoemitters*, Chem. Rev. **111**, 3888 (2011).

[76] D. Gérard, J. Wenger, N. Bonod, E. Popov, H. Rigneault, F. Mahdavi, S. Blair, J. Dintinger, and T. Ebbesen, *Nanoaperture-enhanced fluorescence: Towards higher detection rates with plasmonic metals*, Phys. Rev. B **77**, 045413 (2008).

[77] J. Wenger, D. Gerard, P. F. Lenne, H. Rigneault, N. Bonod, E. Popov, D. Marguet, C. Nelep, and T. W. Ebbesen, *Biophotonics applications of nanometric apertures*, Int. J. Mater. Prod. Technol. **34**, 488 (2009).

[78] J. Wenger, H. Rigneault, J. Dintinger, D. Marguet, and P.-F. Lenne, *Single-fluorophore diffusion in a lipid membrane over a subwavelength aperture*, J. Biol. Phys. **32**, SN1 (2006).

[79] J. Wenger, D. Gérard, J. Dintinger, O. Mahboub, N. Bonod, E. Popov, T. W. Ebbesen, and H. Rigneault, *Emission and excitation contributions to enhanced single molecule fluorescence by gold nanometric apertures*, Opt. Express **16**, 3008 (2008).

[80] S. Khatua, P. M. R. Paulo, H. Yuan, A. Gupta, P. Zijlstra, and M. Orrit, *Resonant plasmonic enhancement of single-molecule fluorescence by individual gold nanorods*, ACS Nano **8**, 4440 (2014).

[81] G. Lu, J. Liu, T. Zhang, W. Li, L. Hou, C. Luo, F. Lei, M. Manfait, and Q. Gong, *Plasmonic near-field in the vicinity of a single gold nanoparticle investigated with fluorescence correlation spectroscopy*, Nanoscale **4**, 3359 (2012).

[82] M. Brinkmeier, K. Dörre, J. Stephan, and M. Eigen, *Two-beam cross-correlation: a method to characterize transport phenomena in micrometer-sized structures*, Anal. Chem. **71**, 609 (1999).

[83] J. Wenger, F. Conchonaud, J. Dintinger, L. Wawrezinieck, T. W. Ebbesen, H. Rigneault, D. Marguet, and P.-F. Lenne, *Diffusion analysis within single nanometric apertures reveals the ultrafine cell membrane organization*, Biophys. J. **92**, 913 (2007).

[84] S. T. Hess, S. Huang, A. A. Heikal, and W. W. Webb, *Biological and chemical*

applications of fluorescence correlation spectroscopy: A review, Biochemistry-US **41**, 697 (2002).

[85] J. Aizpurua, G. W. Bryant, L. J. Richter, and F. J. García de Abajo, *Optical properties of coupled metallic nanorods for field-enhanced spectroscopy*, Phys. Rev. B **71**, 235420 (2005).

[86] K. R. Chi, *Super-resolution microscopy: breaking the limits*, Nat. Methods **6**, 15 (2009).

[87] R. M. Dickson, a. B. Cubitt, R. Y. Tsien, and W. E. Moerner, *On/off blinking and switching behaviour of single molecules of green fluorescent protein*, Nature **388**, 355 (1997).

[88] E. Betzig, G. H. Patterson, R. Sougrat, O. W. Lindwasser, S. Olenych, J. S. Bonifacino, M. W. Davidson, J. Lippincott-Schwartz, and H. F. Hess, *Imaging intracellular fluorescent proteins at nanometer resolution*, Science **313**, 1642 (2006).

[89] T. A. Klar, S. Jakobs, M. Dyba, A. Egner, and S. W. Hell, *Fluorescence microscopy with diffraction resolution barrier broken by stimulated emission*, Proc. Natl. Acad. Sci. U. S. A. **97**, 8206 (2000).

[90] T. Ha, T. Enderle, D. F. Ogletree, D. S. Chemla, P. R. Selvin, and S. Weiss, *Probing the interaction between two single molecules: fluorescence resonance energy transfer between a single donor and a single acceptor*, Proc. Natl. Acad. Sci. U. S. A. **93**, 6264 (1996).

[91] A. I. Chizhik, I. Gregor, F. Schleifenbaum, C. B. Müller, C. Röling, A. J. Meixner, and J. Enderlein, *Electrodynamic coupling of electric dipole emitters to a fluctuating mode density within a nanocavity*, Phys. Rev. Lett. **108**, 163002 (2012).

[92] I. COMSOL, *Comsol Multiphysics 4.4b*, 2014.

[93] J. Stratton and L. Chu, *Diffraction Theory of Electromagnetic Waves*, Phys. Rev. **56**, 99 (1939).

[94] P. Török, P. Higdon, and T. Wilson, *On the general properties of polarised light conventional and confocal microscopes*, Opt. Commun. **148**, 300 (1998).

[95] R. Beams, D. Smith, T. W. Johnson, S. H. Oh, L. Novotny, and a. N. Vamivakas, *Nanoscale fluorescence lifetime imaging of an optical antenna with a single diamond NV center*, Nano Lett. **13**, 3807 (2013).

[96] M. Frimmer, Y. Chen, and a. F. Koenderink, *Scanning emitter lifetime imaging microscopy for spontaneous emission control*, Phys. Rev. Lett. **107**, 123602 (2011).

[97] Y. Xu, R. Lee, and A. Yariv, *Quantum analysis and the classical analysis of spontaneous emission in a microcavity*, Phys. Rev. A **61**, 033807 (2000).

[98] P. Lunnemann, I. Sersic, and A. F. Koenderink, *Optical properties of two-dimensional magnetoelectric point scattering lattices*, Phys. Rev. B **88**, 245109 (2013).

[99] H. Gersen, M. F. García-Parajó, L. Novotny, J. a. Veerman, L. Kuipers, and N. F. Van Hulst, *Near-field effects in single molecule emission*, J. Microsc. **202**, 374 (2001).

[100] M. A. Lieb, J. M. Zavislan, and L. Novotny, *Single-molecule orientations determined by direct emission pattern imaging*, J. Opt. Soc. Am. B **21**, 1210 (2004).

[101] L. Novotny, *Single molecule fluorescence in inhomogeneous environments*, Appl.

Phys. Lett. **69**, 3806 (1996).

[102] H.-J. Gersen, M. Garcia-Parajo, J.-A. Veerman, L. Kuipers, and N. V. Hulst, *Controlling the angular emission of a single molecule*, in *Quantum Electron. Laser Sci. Conf. (QELS 2000). Tech. Dig.*, 2000.

[103] J. Schartner, K. Gavriljuk, A. Nabers, P. Weide, M. Muhler, K. Gerwert, and C. Kötting, *Immobilization of Proteins in their Physiological Active State at Functionalized Thiol Monolayers on ATR-Germanium Crystals*, Chembiochem **15**, 2529 (2014).

[104] L. Laan, S. Roth, and M. Dogterom, *End-on microtubule-dynein interactions and pulling-based positioning of microtubule organizing centers*, Cell Cycle **11**, 3750 (2012).

[105] B. Schuler, E. A. Lipman, and W. A. Eaton, *Probing the free-energy surface for protein folding with single-molecule fluorescence spectroscopy*, Nature **419**, 743 (2002).

[106] R. Zhao and D. Rueda, *RNA folding dynamics by single-molecule fluorescence resonance energy transfer*, Methods **49**, 112 (2009).

[107] P. Kapusta, *Absolute Diffusion Coefficients : Compilation of Reference Data for FCS Calibration. Picoquant Application Note*, 2010.

[108] M. Stelzle, R. Miehlich, and E. Sackmann, *Two-dimensional microelectrophoresis in supported lipid bilayers*, Biophys. J. **63**, 1346 (1992).

[109] M. Wahl, *Time-Correlated Single Photon Counting The Principle of Time-Correlated*, Technical report, PicoQuant GmbH, 2009.

[110] J. Wenger, H. Aouani, D. Gérard, S. Blair, T. W. Ebbesen, and H. Rigneault, *Enhanced fluorescence from metal nanoapertures : physical characterizations and biophotonic applications*, in *Proc. SPIE 7577, Plasmon. Biol. Med. VII, 75770J*, number Section 2, 2010.

[111] P. S. Dittrich and P. Schwille, *Spatial two-photon fluorescence cross-correlation spectroscopy for controlling molecular transport in microfluidic structures*, Anal. Chem. **74**, 4472 (2002).

[112] R. Jaffiol, Y. Blancquaert, A. Delon, and J. Derouard, *Spatial fluorescence cross-correlation spectroscopy*, Appl. Opt. **45**, 1225 (2006).

[113] H. Craighead, *Future lab-on-a-chip technologies for interrogating individual molecules*, Nature **442**, 387 (2006).

[114] F. Falcone, T. Lopetegi, M. A. G. Laso, J. D. Baena, J. Bonache, M. Beruete, R. Marques, F. Martín, and M. Sorolla, *Babinet principle applied to the design of metasurfaces and metamaterials*, Phys. Rev. Lett. **93**, 197401 (2004).

[115] T. Zentgraf, T. Meyrath, A. Seidel, S. Kaiser, H. Giessen, C. Rockstuhl, and F. Lederer, *Babinet s principle for optical frequency metamaterials and nanoantennas*, Phys. Rev. B **76**, 33407 (2007).

[116] B. Ögüt, R. Vogelgesang, W. Sigle, N. Talebi, C. T. Koch, and P. A. van Aken, *Hybridized metal slit eigenmodes as an illustration of Babinet's principle*, ACS Nano **5**, 6701 (2011).

[117] T. W. Ebbesen, H. J. Lezec, H. F. Ghaemi, T. Thio, and P. A. Wolff, *Extraordinary optical transmission through sub-wavelength hole arrays*, Nature **391**, 667 (1998).

[118] A. F. Koenderink, J. V. Hernández, F. Robicheaux, L. D. Noordam, and A. Polman,

Programmable nanolithography with plasmon nanoparticle arrays, Nano Lett. **7**, 745 (2007).

[119] T. Kosako, H. F. Hofmann, and Y. Kadoya, *Directional emission of light from a nano-optical Yagi-Uda antenna*, Nat. Photonics **4**, 4 (2009).

[120] A. F. Koenderink, *Plasmon nanoparticle array waveguides for single photon and single plasmon sources*, Nano Lett. **9**, 4228 (2009).

[121] G. Vecchi, V. Giannini, and J. Gómez Rivas, *Shaping the fluorescent emission by lattice resonances in plasmonic crystals of nanoantennas*, Phys. Rev. Lett. **102**, 146807 (2009).

[122] G. Lozano, D. J. Louwers, S. R. Rodríguez, S. Murai, O. T. Jansen, M. a. Verschuuren, and J. Gómez Rivas, *Plasmonics for solid-state lighting: enhanced excitation and directional emission of highly efficient light sources*, Light Sci. Appl. **2**, e66 (2013).

[123] K. Busch and S. John, *Photonic band gap formation in certain self-organizing systems*, Phys. Rev. E **58**, 3896 (1998).

[124] A. F. Koenderink, L. Bechger, H. P. Schriemer, A. Lagendijk, and W. L. Vos, *Broadband fivefold reduction of vacuum fluctuations probed by dyes in photonic crystals*, Phys. Rev. Lett. **88**, 143903 (2002).

[125] M. Fujita, S. Takahashi, Y. Tanaka, T. Asano, and S. Noda, *Simultaneous inhibition and redistribution of spontaneous light emission in photonic crystals*, Science **308**, 1296 (2005).

[126] P. Lodahl, A. Floris Van Driel, I. S. Nikolaev, A. Irman, K. Overgaag, D. Vanmaekelbergh, and W. L. Vos, *Controlling the dynamics of spontaneous emission from quantum dots by photonic crystals*, Nature **430**, 654 (2004).

[127] M. R. Jorgensen, J. W. Galusha, and M. H. Bartl, *Strongly modified spontaneous emission rates in diamond-structured photonic Crystals*, Phys. Rev. Lett. **107**, 143902 (2011).

[128] S. Noda, M. Fujita, and T. Asano, *Spontaneous-emission control by photonic crystals and nanocavities*, Nat. Photonics **1**, 449 (2007).

[129] M. Barth, N. Nüsse, B. Löchel, and O. Benson, *Controlled coupling of a single-diamond nanocrystal to a photonic crystal cavity*, Opt. Lett. **34**, 1108 (2009).

[130] K. Aoki, D. Guimard, M. Nishioka, M. Nomura, S. Iwamoto, and Y. Arakawa, *Coupling of quantum-dot light emission with a three-dimensional photonic-crystal nanocavity*, Nat. Photonics **2**, 688 (2008).

[131] S. Noda, *Photonic crystal lasers - ultimate nanolasers and broad-area coherent lasers [Invited]*, J. Opt. Soc. Am. B **27**, B1 (2010).

[132] T. Ming, L. Zhao, H. Chen, K. C. Woo, J. Wang, and H. Q. Lin, *Experimental evidence of plasmophores: Plasmon-directed polarized emission from gold nanorod - Fluorophore hybrid nanostructures*, Nano Lett. **11**, 2296 (2011).

[133] T. Ming, H. Chen, R. Jiang, Q. Li, and J. Wang, *Plasmon-Controlled Fluorescence: Beyond the Intensity Enhancement*, J. Phys. Chem. Lett. **3**, 191 (2012).

[134] S. Wedge, I. Hooper, I. Sage, and W. Barnes, *Light emission through a corrugated metal film: The role of cross-coupled surfaceplasmon polaritons*, Phys. Rev. B **69**, 245418 (2004).

[135] S. R. K. Rodriguez, S. Murai, M. A. Verschuuren, and J. G. Rivas, *Light-Emitting*

Waveguide-Plasmon Polaritons, Phys. Rev. Lett. **109**, 166803 (2012).

[136] A. V. Zayats, I. I. Smolyaninov, and A. A. Maradudin, *Nano-optics of surface plasmon polaritons*, Phys. Rep. **408**, 131 (2005).

[137] F. J. G. De Abajo and F. J. García de Abajo, *Colloquium: Light scattering by particle and hole arrays*, Rev. Mod. Phys. **79**, 1267 (2007).

[138] F. J. Garcia-Vidal, L. Martin-Moreno, T. W. Ebbesen, and L. Kuipers, *Light passing through subwavelength apertures*, Rev. Mod. Phys. **82**, 729 (2010).

[139] F. Przybilla, A. Degiron, C. Genet, T. Ebbesen, F. de Léon-Pérez, J. Bravo-Abad, F. J. García-Vidal, and L. Martín-Moreno, *Efficiency and finite size effects in enhanced transmission through subwavelength apertures*, Opt. Express **16**, 9571 (2008).

[140] J. Henzie, M. H. Lee, and T. W. Odom, *Multiscale patterning of plasmonic metamaterials*, Nat. Nanotechnol. **2**, 549 (2007).

[141] S. Kitson, W. Barnes, and J. Sambles, *Full Photonic Band Gap for Surface Modes in the Visible*, Phys. Rev. Lett. **77**, 2670 (1996).

[142] W. L. Barnes, S. C. Kitson, T. W. Preist, and J. R. Sambles, *Photonic surfaces for surface-plasmon polaritons*, J. Opt. Soc. Am. A **14**, 1654 (1997).

[143] P. Lalanne, J. C. Rodier, and J. P. Hugonin, *Surface plasmons of metallic surfaces perforated by nanoholes*, J. Opt. A Pure Appl. Opt. **7**, 16 (2005).

[144] Y. C. Jun, K. C. Y. Huang, and M. L. Brongersma, *Plasmonic beaming and active control over fluorescent emission*, Nat. Commun. **2**, 283 (2011).

[145] M. A. Verschuuren, P. Gerlach, H. A. van Sprang, and A. Polman, *Improved performance of polarization-stable VCSELs by monolithic sub-wavelength gratings produced by soft nano-imprint lithography*, Nanotechnology **22**, 505201 (2011).

[146] P. Nagpal, N. C. Lindquist, S.-H. Oh, and D. J. Norris, *Ultrasmooth patterned metals for plasmonics and metamaterials*, Science **325**, 594 (2009).

[147] J. Henzie, J. Lee, M. H. Lee, W. Hasan, and T. W. Odom, *Nanofabrication of plasmonic structures*, Annu. Rev. Phys. Chem. **60**, 147 (2009).

[148] P. Schwille, J. Bieschke, and F. Oehlenschläger, *Kinetic investigations by fluorescence correlation spectroscopy: the analytical and diagnostic potential of diffusion studies*, Biophys. Chem. **66**, 211 (1997).

[149] B. E. A. Saleh and M. C. Teich, *Fundamentals of Photonics - Second Edition*, Wiley, 2nd edition, 2007.

[150] I. Sersic, C. Tuambilangana, T. Kampfrath, and A. F. Koenderink, *Magnetoelectric point scattering theory for metamaterial scatterers*, Phys. Rev. B **83**, 12 (2011).

[151] C. A. Balanis, *Antenna Theory: Analysis and Design*, Wiley, 3 edition, 2012.

[152] J. J. Penninkhof, A. Moroz, A. Van Blaaderen, and A. Polman, *Optical properties of spherical and oblate spheroidal gold shell colloids*, J. Phys. Chem. C **112**, 4146 (2008).

[153] A. Taflove and S. C. Hagness, *Computational Electrodynamics: The Finite-Difference Time-Domain Method*, Artech House Publishers, 3rd edition, 2005.

[154] W. Lukosz and R. E. Kunz, *Light emission by magnetic and electric dipoles close to a plane interface I Total radiated power*, J. Opt. Soc. Am. **67**, 1607 (1977).

[155] W. Lukosz and R. E. Kunz, *Light emission by magnetic and electric dipoles close to a plane dielectric interface II Radiation patterns of perpendicular oriented dipoles*, J. Opt. Soc. Am. **67**, 1615 (1977).

[156] H. Rigneault and F. Lemarchand, *Extraction of light from sources located inside waveguide grating structures*, Opt. Lett. **24**, 148 (1999).
[157] W. A. Harrison, *Solid state theory*, Dover Publications, 2011.
[158] M. Kretschmann and a. Maradudin, *Band structures of two-dimensional surface-plasmon polaritonic crystals*, Phys. Rev. B **66**, 245408 (2002).
[159] I. S. Nikolaev, P. Lodahl, and W. L. Vos, *Quantitative analysis of directional spontaneous emission spectra from light sources in photonic crystals*, Phys. Rev. A **71**, 053813 (2004).
[160] M. Barth, A. Gruber, and F. Cichos, *Spectral and angular redistribution of photoluminescence near a photonic stop band*, Phys. Rev. B **72**, 085129 (2005).
[161] F. García-Santamaría, J. F. Galisteo-López, P. V. Braun, and C. López, *Optical diffraction and high-energy features in three-dimensional photonic crystals*, Phys. Rev. B **71**, 195112 (2005).
[162] J. F. Galisteo-López, M. Galli, M. Patrini, A. Balestreri, L. C. Andreani, and C. López, *Effective refractive index and group velocity determination of three-dimensional photonic crystals by means of white light interferometry*, Phys. Rev. B **73**, 125103 (2006).
[163] Z.-Y. Li and Z.-Q. Zhang, *Weak photonic band gap effect on the fluorescence lifetime in three-dimensional colloidal photonic crystals*, Phys. Rev. B **63**, 125106 (2001).
[164] I. S. Nikolaev, P. Lodahl, and W. L. Vos, *Fluorescence lifetime of emitters with broad homogeneous linewidths modified in opal photonic crystals*, J. Phys. Chem. C **112**, 7250 (2008).
[165] L. Novotny and N. van Hulst, *Antennas for light*, Nat. Photonics **5**, 83 (2011).
[166] H. Gao, J. K. Hyun, M. H. Lee, J.-C. Yang, L. J. Lauhon, and T. W. Odom, *Broadband Plasmonic Microlenses Based on Patches of Nanoholes*, Nano Lett. (2010).
[167] L. Lin, X. M. Goh, L. P. McGuinness, and A. Roberts, *Plasmonic lenses formed by two-dimensional nanometric cross-shaped aperture arrays for fresnel-region focusing*, Nano Lett. **10**, 1936 (2010).
[168] G. M. Lerman and U. Levy, *Generation of a radially polarized light beam using space-variant subwavelength gratings at 1064 nm*, Opt. Lett. **33**, 2782 (2008).
[169] S. Rodriguez and J. G. Rivas, *Surface lattice resonances strongly coupled to Rhodamine 6G excitons: tuning the plasmon-exciton-polariton mass and composition*, Opt. Express **21**, 27411 (2013).
[170] A. H. Schokker and A. F. Koenderink, *Lasing at the band edges of plasmonic lattices*, Phys. Rev. B **90**, 155452 (2014).
[171] T. Shegai, S. Chen, V. D. Miljković, G. Zengin, P. Johansson, and M. Käll, *A bimetallic nanoantenna for directional colour routing*, Nat. Commun. **2**, 481 (2011).
[172] A. D. Rakic, A. B. Djurisic, J. M. Elazar, and M. L. Majewski, *Optical properties of metallic films for vertical-cavity optoelectronic devices*, Appl. Opt. **37**, 5271 (1998).
[173] C. M. Dodson, J. A. Kurvits, D. Li, and R. Zia, *Wide-angle energy-momentum spectroscopy*, Opt. Lett. **39**, 3927 (2014).
[174] H. Urbach and G. Rikken, *Spontaneous emission from a dielectric slab*, Phys. Rev. A **57**, 3913 (1998).

[175] C. Kittel, *Introduction to solid state physics*, Wiley, 8th edition, 2005.
[176] S. Larouche and D. R. Smith, *Reconciliation of generalized refraction with diffraction theory*, Opt. Lett. **37**, 2391 (2012).
[177] L. Langguth, *Coupling in Metamaterials*, Diplomarbeit, Universität Stuttgart, 2010.
[178] C. Arnold, F. Marquier, M. Garin, F. Pardo, S. Collin, N. Bardou, J.-L. Pelouard, and J.-J. Greffet, *Coherent thermal infrared emission by two-dimensional silicon carbide gratings*, Phys. Rev. B **86**, 035316 (2012).

Summary

Fluorescence describes the property of matter to absorb light and shortly after emit light of another color. Fluorescent materials are found in nature, e.g. in the jelly-fish *Aequorea victoria*, in some plants and mushrooms, and in minerals such as *Fluorite* in which this property was first scientifically described. For electric lighting in our homes and streets fluorescent materials are a key ingredient in every compact fluorescent lamp and white light LED. In the life sciences, fluorescent molecules have become indispensable to selectively mark functional parts of living cells or tissues, and fluorescence microscopy is of paramount importance for today's biological imaging. Which color is absorbed by the fluorophore, and how much time it takes until the fluorescence photon of lower frequency is emitted, are properties of the fluorescent molecule. Additionally, these parameters depend on the optical environment of the molecule. Metallic nano-structures can act as effective antennas for fluorophores, as they can increase the emission rate, determine the polarization, spectral shape and radiation pattern of the fluorescence emission. Therefore, metal nano-structures are pursued by many groups to improve fluorescence microscopy.

This thesis is divided into three parts and targets the question of how different fluorescence applications can benefit from metal nano-antennas.

The first part addresses the scenario of a plasmon-antenna enhanced fluorescence correlation spectroscopy (FCS) experiment. FCS allows to locally determine the mobility of fluorescent molecules in solution, via the analysis of fluctuations of the fluorescence intensity generated from a high numerical aperture focus. The fluorescence fluctuations originate from random motions of the fluorophores in and out of the detection volume. In 2003, Levene et al. performed FCS in round nano-apertures (ø≈ 50 nm) in an optically thick aluminum film, to reduce the detection volumes by three orders of magnitude compared to a diffraction limited focus. In Chapter 2 we revisit conventional FCS where the detection volume is given by a diffraction limited focus in a bulk liquid. How the detection volume changes in the presence of a spherical nano-antenna is illustrated by exact calculations of antenna-enhanced FCS at a Mie sphere, which evidences two intense near-field lobes i.e. 'hotspots'. In Chapter 3 a general model is developed which allows the efficient calculation of FCS measurements in the presence of arbitrarily complex detection volumes. The model is applied to a simple system of a diffraction limited focus with a superimposed hot-spot, which elucidates the requirements and limitations of a plasmon-enhanced FCS experiment. It is shown, how the fluorescence background originating from the diffraction limited focus, adversely affects the high correlation contrast provided by the hotspot.

The second part of the thesis describes how the position of a single molecule relative to a nano-antenna translates into far-field properties of the fluorescence emission, such as polarization, fluorescence lifetime or radiation pattern. In Chapter 4 we present a new method to localize single molecules close to a nano-antenna based on these different far-field observables. The proposed method uses simultaneous measurements of different far-field observables, which allow to reconstruct the coordinates with an accuracy of a few nanometers relative to the nano-antenna. Moreover, it allows localization rates in the kHz regime. Chapter 5 shows how diffusing emitters introduce fluctuations in non-intensity observables. Furthermore, we discuss how lifetime fluctuations can alleviate the problems of background signals which we encountered in Chapter 3. Additionally, Chapter 5 shows that lifetime and polarization fluctuations can be used to measure the near-field volume of plasmonic antennas. As the calibration of a plasmon enhanced FCS experiments is intrinsically challenging, Chapter 6 presents a plasmonic design of a dual focus FCS experiment which allows the measurement of a diffusion coefficient without additional calibration.

Part three discusses two experiments which address the question of how to shape the angular distribution of the fluorescence emission of an incoherent ensemble of dye molecules. Chapter 7 presents an improvement to the nano-aperture enhanced FCS measurements. Typically, a large fraction of fluorescence photons is lost because the emitter does not radiate into the collection optics, but rather into surface plasmons, i.e., surface waves bound to the metal film. We show how the surface plasmons can be recuperated to contribute to the photon signal by using small periodic arrays of nano-apertures. These couple the surface plasmon polaritons into highly directional free space radiation right into collection optics. Chapter 8 combines the concept of metasurfaces with an ensemble of incoherent sources in a waveguide. Metasurfaces consist of nano-structured elements which are arranged on a periodic lattice in a plane. If the spacing between these elements is much smaller than the wavelength of an impinging electromagnetic wave, the wave perceives effective interface properties, which can modify the polarization and phasefront almost arbitrarily by design of the metasurface. We show how the design of the periodic meta-surface allows to control the scattering amplitude of the reciprocal lattice, and how it translates into directional emission of the ensemble fluorescence into the far-field.

Samenvatting

Fluorescentie is de eigenschap van materie om energie in de vorm van licht te absorberen en vervolgens, met enige vertraging, weer licht uit te stralen, meestal van een iets andere kleur. Fluorescente materialen zijn te vinden in de natuur, bijvoorbeeld in de kwal *Aequorea victoria*, in sommige planten, paddestoelen, en in minerale gesteenten zoals *Fluoriet*, waarvoor het fenomeen 'fluorescentie' het eerst wetenschappelijk beschreven is. Fluorescente materialen zijn een heel belangrijk bestanddeel van de elektrische verlichting waarmee we onze huizen en straten verlichten, met name in TL-buizen, spaarlampen, en witte LED-verlichting. In de levenswetenschappen zijn fluorescente moleculen niet weg te denken, omdat ze het mogelijk maken om functioneel belangrijke onderdelen van levende cellen en organische weefsels selectief te markeren en zichtbaar te maken in afbeeldingen door middel van 'fluorescentie-microscopie'. Welke kleur een fluorofoor absorbeert, en uitzendt, en hoe lang dit uitzenden duurt zijn eigenschappen van het molecuul. Bovendien hangen deze eigenschappen af van de omgeving van het molecuul. Met behulp van nanoschaal metaalstructuren die als antenne dienen die gekoppeld kunnen worden aan een fluorofoor, is het mogelijk om fluorescentie te beïnvloeden. Zo is het mogelijk fluoroforen sneller, en daarmee helderder te laten stralen, de polarisatie en de bundelrichting van de fluorescentie naar believen vorm te geven, en het spectrum te wijzigen.

Dit proefschrift is onderverdeeld in drie delen, en heeft als centraal thema, hoe verschillende toepassingen van fluorescentie door het gebruik van antennes verbeterd kunnen worden.

Het eerste deel van het proefschrift is toegespitst op het verbeteren van 'fluorescentie correlatie spectroscopie' (FCS) door middel van metalen 'plasmonische' antennes. FCS is een techniek om heel lokaal de mobiliteit te meten van fluorescente moleculen die diffunderen in een oplossing, door middel van het meten van fluctuaties in de fluorescentie intensiteit die optreden wanneer je fluorescentie aanslaat en verzamelt, vanuit een heel nauw focus gemaakt door een hoge numerieke apertuur microscoopobjectief. Deze fluctuaties ontstaan omdat moleculen willekeurig het detectievolume in en uit bewegen door Brownse beweging. In 2003 lieten Levene et al. zien dat ze het detectievolume wel duizendmaal konden verkleinen ten opzichte van dat in de beste microscoop, door FCS te meten in nanoschaal openingen van 50 nm doorsnede in een optisch dikke metaalfilm. In hoofdstuk 2 vatten we eerst samen hoe standaard FCS werkt in het focus van een microscoop. Vervolgens bespreken we de mogelijkheden om detectievolumes te verkleinen met het complement van een nanoschaal gat in een metaalfilm, namelijk een metalen

nanodeeltje. Deze metalen 'Mie' bol geeft een complex gevormd detectievolume, met twee 'hot spots' die subgolflengte afmetingen hebben. In hoofdstuk 3 presenteren we een eenvoudig model waarmee FCS in willekeurig gevormde detectievolumes beschreven kan worden. We passen het model toe op het scenario waarin een diffractiegelimiteerd focus met daarin een plasmonische antenne met lokale veldversterking gebruikt wordt. De berekening laat zien wat de eisen aan plasmonische antennes zijn om FCS te verbeteren, en ook wat de beperkingen zijn. Zelfs bij aanzienlijke veldversterking vormt de fluorescentie die als achtergrond aanwezig is door het focus waarmee de antenne beschenen wordt een groot probleem, omdat het de sterke toename van het correlatiecontrast dat door de antenne gerealiseerd wordt grotendeels weer teniet doet.

Het tweede deel van het proefschrift beschrijft hoe de precieze positie van een fluorofoor ten opzichte van een nanoschaal antenne zich vertaalt in eigenschappen in het verre veld anders dan de totale in een microscoop te meten intensiteit, zoals de hoekverdeling van licht, de fluorescente levensduur en polarisatie. In Hoofdstuk 4 laten we zien dat op basis hiervan het mogelijk moet zijn om de positie van een molecuul met nanometrische precisie te meten. Hiertoe moeten tegelijk de drie genoemde eigenschappen gemeten worden. Nanometer lokalisatie precisie is binnen bereik, binnen een meting van circa 1 ms integratietijd. Hoofdstuk 5 bediscussieert hoe in dit scenario diffusie van een fluorofoor aanleiding geeft tot fluctuaties in meetbare grootheden anders dan intensiteit, waar standaard FCS op gebaseerd is. Fluctuatie correlatie spectroscopie van deze grootheden, dat wil zeggen, van bijvoorbeeld fluorescente levensduur en polarisatie, vermindert de problematiek aangestipt in hoofdstuk 3 sterk. Dat wil zeggen dat deze nieuwe vormen van fluctuatie correlatie spectroscopie veel minder gevoelig zouden moeten zijn voor achtergrond vanuit het focus waarmee de plasmon antenne aangeslagen wordt. Hoofdstuk 5 legt uit hoe het met deze techniek mogelijk moet zijn om volumes van plasmonische hot spots direct te meten. Voorwaarde voor deze meting, zoals bij alle vormen van fluorescentie correlatie spectroscopie, is wel nauwkeurige calibratie van de opstelling met behulp van een standaardoplossing. De reden is dat FCS intrinsiek een tijdschaal meet, en deze pas omgezet kan worden naar een plasmonische lengteschaal als er een bekende diffusieconstante in het spel is, of omgekeerd er pas een diffusieconstante afgeleid kan worden als de lengteschaal vast ligt. Deze lengteschaal is echter moeilijk *onafhankelijk* te bepalen voor een enkele nanoantenne. Hoofdstuk 6 bespreekt een ontwerp voor een plasmonisch antenne substraat waarbij calibratie niet meer nodig is, omdat het substraat bestaat uit een reeks nano-antennes op vaste afstanden van elkaar. Door slimme oriëntatie van de antennes levert dit een kruiscorrelatie op tussen metingen op verschillend gepolariseerde detectoren, die een calibratievrije bepaling van diffusieconstanten toestaat.

Deel drie van dit proefschrift bespreekt twee experimenten die zich toespitsen op de vraag hoe je de hoekverdeling van fluorescent licht van een incoherent ensemble van fluoroforen naar believen vorm geeft. Hoofdstuk 7 presenteert een aanzienlijke verbetering op de klassieke nano-apertuur metingen zoals die voor het eerst door Levene gerapporteerd zijn. In zulke experimenten wordt een groot deel van de fluorescentie niet door de detector verzameld, omdat een groot deel van de fotonen niet het objectief ingestraald wordt, maar aan het metaal gebonden blijven als zogenoemde 'oppervlakteplasmonen'. We laten zien hoe deze fotonen terug gewonnen kunnen worden door kleine periodieke gaatjesroosters te gebruiken die de oppervlaktegolf uitstralen als een nauwe bundel die precies de

collectie-optiek in is gericht. Hoofdstuk 8 combineert fluorescentie met het concept ‘meta-oppervlak’. ‘Meta-oppervlakken’ zijn roosters van metalen nano-antennes in een vlak, met een periodiciteit veel kleiner dan de golflengte van licht. In zo’n geval ziet een inkomende golf een effectief homogeen grensvlak, maar met reflectie en transmissie eigenschappen die bijna willekeurig ontworpen kunnen worden. We laten zien hoe een ‘meta-oppervlak’ met een complexe eenheidscel de verstrooiingsamplitude van verschillende diffractieordes beïnvloedt, en hoe dit zich vertaalt in een asymmetrisch gerichte afstraling van fluorescentie door ensembles van incoherente bronnen.

Acknowledgements

I started my PhD in the Resonant Nanophotonics Group to learn how to do experimental nano-optics. After five years of work with single nano particles and single molecules, not only my hair, patience and frustration threshold have grown, but I can resume, I have learned many invaluable lessons about how to and how not to do experiments.

First, I thank Femius for giving me the chance to 'play' in his labs, for his patience and support during my experimental struggles and many interesting discussions we had in our weekly meetings and all the things I learned in the last five years.

I want to thank all the students, I had the pleasure to share office 2.14 with: Martin, Ruben, Freddy, Hugo, Oleg and Jia. Special thanks to Martin, who was very valuable to me as a scientific discussion partner. After registering for overwork and sharing a beer in the office our discussions helped me to see things from another perspective. Also I want to thank Oleg, for educating me on pump-probe spectroscopy, the countless times when we were lost in fourier space, all the updates on newest gadgets and technology and for filling the cookie jar regularly with double-chocolate cookies.

Thanks to all the members of the Resonant Nanophotonics Group for good atmosphere. Special thanks to Hinke and Abbas for their help with sample fabrication, and to Martin, Andrej, Per, Felipe, Cocoa and Clara for insightful discussions about fluorescence, coupled-dipole models, polarization and everything else. What I will miss most are the scientific discussions, e.g. in the Nanophotonics poster sessions. I want to thank all the members of the Center for Nanophotonics for the interesting physics discussions we had over the years, especially Jochen, Boris, Gabriel and Sander.

Further I want to thank Jérôme and Deep for sharing their expertise on plasmonic FCS in Marseille and the experience, how easy FCS measurements can be.

None of my experimental work in AMOLF would have been possible without the excellent support. I want to acknowledge all the technical support staff, that was directly involved in help with my microscope: Iliya, Henk-Jan, all the members of the mechanical workshop, Duncan, Idsart and Jan for all the electronic components, and Sjoerd and Luc for the software that collects and stores all the photons and computes the correlation function so efficiently. Further thanks to Hinco, Idsart, Niels, Dion, Ricardo and Mark for their technical help on various 'friday-afternoon' projects.

Also the rest of the support staff, that took a lot of work off the shoulders my shoulders, by helping me to have a roof over my head, keeping the computers and coffee machine running, order and receive packages for me, and made me enter every morning into a tidy building.

My time in Amsterdam did luckily not only consist of work. I want to thank Stefanie for your support from distance and the good times we had together in Stuttgart and Amsterdam.

Further, I have been very lucky with my housemates. I want to thank Sophie and Núria and Jeanette and Cristina, for the great time together in our apartment in the Herschelstraat, and Stephan for my short but enjoyable stay in the Middenweg. All of you gave me the feeling to come home after the long days in *the Institution* - thank you.

Special thanks to Maga who welcomed me in her cozy home, showing me so many nice places in Amsterdam, all the fun times we had together, the support to get through with my theses, and for putting one million commas (and other corrections) into this book.

Finally and most importantly, I want to thank my parents for their continuous support, not only during the PhD but since ever. It was always comforting to know, no matter what happens, I would always be more than welcome to come home to Karlsruhe, where a freezer full of homemade pizza is waiting for me.

List of publications

This thesis is based on the following publications:

- *Simple model for plasmon enhanced fluorescence correlation spectroscopy*
  L. Langguth and A. F. Koenderink
  Optics Express **22**, 15397-15409 (2014). **(Chapter 3)**

- *Plasmonic band structure controls single molecule fluorescence*
  L. Langguth, D. Punj, J. Wenger, and A. F. Koenderink
  ACS Nano **7**, 8840-8848 (2013). **(Chapter 7)**

- *Rigorous analysis of FCS at a plasmonic Mie sphere*
  L. Langguth and A. F. Koenderink
  in preparation for Journal of Optical Society of America B. **(Chapter 2)**

- *Plasmonic gradient-phase metasurfaces for spontaneous emission control*
  L. Langguth, A. H. Schokker, K. Guo and A. F. Koenderink
  in preparation for Scientific Reports. **(Chapter 8)**

- *Quantitative proposals for plasmon-enhanced FCS experiments using lifetime and polarization contrast*
  L. Langguth and A. F. Koenderink
  in preparation for New Journal of Physics. **(Chapter 5 & 6)**

Other publications by the author:

- *Coupling strength of complex plasmonic structures in the multiple dipole approximation*
  L. Langguth and H. Giessen
  Optics Express **19**, 22156-22166 (2009).

- *Planar metamaterial analogue of electromagnetically induced transparency for plasmonic sensing*
  N. Liu, T. Weiss, M. Mesch, L. Langguth, U. Eigenthaler, M. Hirscher, C. Sönnichsen, and H. Giessen
  Nano Letters **10**, 1103-1107 (2010).

- *Cavity-enhanced localized plasmon resonance sensing*
  R. Ameling, L. Langguth, M. Hentschel, M. Mesch, P. v. Braun, and H. Giessen
  Applied Physics Letters **97**, 253116:1-3 (2010).

- *Plasmonic analogue of electromagnetically induced transparency at the Drude damping limit*
  N. Liu, L. Langguth, T. Weiss, J. Kästel, M. Fleischhauer, T. Pfau and H. Giessen
  Nature Materials **8**, 758-762 (2009).